

# University of Alberta

Materials Characterization and Growth Mechanisms of ZnO, ZrO<sub>2</sub>, and HfO<sub>2</sub> Deposited by  
Atomic Layer Deposition

by

Amir Afshar

A thesis submitted to the Faculty of Graduate Studies and Research  
in partial fulfillment of the requirements for the degree of

Doctor of Philosophy

in

Materials Engineering

Department of Chemical and Materials Engineering

© Amir Afshar  
Spring 2014  
Edmonton, Alberta

Permission is hereby granted to the University of Alberta Libraries to reproduce single copies of this thesis and to lend or sell such copies for private, scholarly or scientific research purposes only. Where the thesis is converted to, or otherwise made available in digital form, the University of Alberta will advise potential users of the thesis of these terms.

The author reserves all other publication and other rights in association with the copyright in the thesis and, except as herein before provided, neither the thesis nor any substantial portion thereof may be printed or otherwise reproduced in any material form whatsoever without the author's prior written permission.

*To my wonderful wife, Arezou, who has always been there inspiring me to do better.*

*And to my parents, Mahrokh and Esmaeil, and to my sisters, Azin and Ada.*

## **Abstract**

Gallium Nitride (GaN) is recognized as one of the best candidates for high-power high-frequency metal-oxide-semiconductor field-effect-transistors (MOSFETs). The critical component to enable this technology is the development of a robust oxide with low density of defects and preferential mobility properties that can produce an enhancement mode transistor rather than a depletion mode transistor. Zirconium oxide ( $\text{ZrO}_2$ ) and hafnium oxide ( $\text{HfO}_2$ ) are considered as two promising oxides for the gate oxide of the GaN MOSFETs. On the other hand, zinc oxide (ZnO) is an alternative wide bandgap semiconductor for GaN. ZnO has some advantages over GaN in optoelectronics due to its large exciton binding energy ( $\sim 60$  meV), and is widely used as the active channel in thin film transistors (TFTs). To control the electrical properties of the deposited thin films, a fundamental understanding of the nucleation and growth mechanisms is essential. In this dissertation, the material characterization and growth mechanisms of atomic layer deposition (ALD) of the three important oxides in semiconductor industry, ZnO,  $\text{ZrO}_2$ , and  $\text{HfO}_2$ , were investigated. The oxides were deposited using thermal and plasma-enhanced ALD on Si(100) substrate at various deposition temperatures. Different analytical techniques, including spectroscopic ellipsometry (SE), X-ray photoelectron spectroscopy (XPS), X-ray diffraction (XRD), atomic force microscopy (AFM), and transmission electron microscopy (TEM) were utilized to analyze the optical, chemical, and morphological characteristics of the oxide thin films. Based on the results, nucleation and growth mechanisms were proposed for thermal and plasma enhanced ALD of ZnO,  $\text{ZrO}_2$ ,

and HfO<sub>2</sub>. The role of ALD parameters, as well as –OH reaction sites on the nucleation and growth mechanisms were described. Atomistic growth mechanisms of thermal ALD ZnO, ZrO<sub>2</sub>, and HfO<sub>2</sub> were studied using a density functional theory (DFT) approach. The important role of formation of intermediate structures between surface reaction sites and the precursor molecules were emphasized. The results were found to be consistent with the variation of growth rate of the ALD oxides with the deposition temperature. Finally, it was found that PEALD ZrO<sub>2</sub> offered the best properties for the gate oxide of the GaN MOSFETs with the lowest value of density of interface traps.

## **Acknowledgments**

This thesis would never come to existence without support and assistance from many individuals. I would like to gratefully thank my supervisor Dr. Ken Cadien for his support, enthusiastic guidance, inspiration, and patience throughout my PhD program. I would also like to thank Dr. Douglas Barlage for his advice, and encouragements along my study. I am also grateful to the examining committee members, Dr. John Nychka, Dr. Vinay Prasad, and Dr. David Emslie for their insightful comments on my thesis.

Much of the work I did was the results of collaborations with my fellow colleagues. I would like to especially thank Dr. Ali Foroughi, Triratna Muneshwar, Kyle Bothe, Peter von Hauff, Alex Ma, Gem Shoute, Mei Shen, Dr. Manisha Gupta, Mourad Benlarmi, Alireza Kohan Dehghan, and Dr. Farshid Vejahati, for many insightful debates and ideas.

I am grateful to Dr. Bruce Rayner, Noel O'Toole, and Don Fillipelli from Kurt J. Lesker for their time on training me on the atomic layer deposition system and also helping me in troubleshooting the system.

I would like to thank the faculty and staff of the Department of Chemical and Materials Engineering, especially Lily Laser, Mia Law, Marion Pritchard, and Kevin Heidebrecht for all the provided fundamental administrative and technical assistance to me.

I would like to thank my beloved wife, Arezou Elliyoon, for her patience, support, and encouragements throughout my PhD studies and also helping me

with drawing the schematic figures in this thesis. Lastly, I would like to thank my parents and my sisters for their constant support throughout the course of my studies.

# Table of Contents

|   |           |
|---|-----------|
| <b>1. Introduction.....</b>   | <b>1</b>  |
| 1.1 Background.....   | 1         |
| 1.2 Literature Review .....   | 2         |
| 1.2.1 Zinc Oxide (ZnO).....   | 2         |
| 1.2.2 Gallium Nitride (GaN) .....                                       | 2         |
| 1.2.3 GaN-Based Transistors .....                                       | 4         |
| 1.2.4 MOSFET Operation and Interface Oxides.....                        | 6         |
| 1.2.5 Gate Oxide Materials for GaN MOSFETs.....                         | 7         |
| 1.2.6 Heterojunction Band Alignment .....                               | 9         |
| 1.2.7 Previous Studies on Dielectric Materials for GaN MOSFETs ..       | 10        |
| 1.2.8 Atomic Layer Deposition (ALD) of Oxides .....                     | 15        |
| 1.3 Objectives of This Work.....  | 18        |
| 1.4 Outline of Thesis .....   | 19        |
| <b>2. Theoretical Background of Quantum Chemistry Calculations.....</b> | <b>20</b> |
| 2.1 Schrödinger Equation for a Many-Body System.....                    | 20        |
| 2.2 Born-Oppenheimer Approximation and Variational Theorem .....        | 22        |
| 2.3 Basis Functions.....  | 23        |
| 2.4 Molecular Orbital Methods – Hartree-Fock .....                      | 25        |
| 2.5 Density Functional Theory .....                                     | 27        |

|   |           |
|---|-----------|
| 2.6 Geometry Optimization and Frequency Calculations .....            | 29        |
| 2.7 Computational Chemistry Approach to Atomic Layer Deposition ..... | 30        |
| 2.8 Computational Method in This Thesis .....                         | 31        |
| <b>3. Experimental Procedures .....</b>                               | <b>32</b> |
| 3.1 ALD Reactor .....   | 32        |
| 3.2 Sample Preparation .....  | 35        |
| 3.3 In-Situ Spectroscopic Ellipsometry .....                          | 36        |
| 3.4 Atomic Force Microscopy (AFM) .....                               | 38        |
| 3.5 X-Ray Photoelectron (XPS) Analyses .....                          | 40        |
| 3.6 X-Ray Diffraction (XRD) Analyses .....                            | 41        |
| <b>4. Atomic Layer Deposition of Zinc Oxide .....</b>                 | <b>43</b> |
| 4.1 Introduction .....  | 43        |
| 4.2 Experimental Procedure and Theoretical Model .....                | 45        |
| 4.3 Results and Discussion .....                                      | 46        |
| 4.3.1 Optical Constants .....   | 46        |
| 4.3.2 Saturation curves and GPC .....                                 | 50        |
| 4.3.3 Chemical Composition .....                                      | 52        |
| 4.3.4 Roughness .....   | 56        |
| 4.3.5 Crystallinity .....   | 59        |
| 4.3.6 Electrical Resistivity .....                                    | 62        |
| 4.4 Growth Mechanism of TALD ZnO: DFT Approach .....                  | 64        |

|   |            |
|---|------------|
| 4.5 Conclusions .....   | 76         |
| <b>5. Atomic Layer Deposition of Zirconium Oxide .....</b>        | <b>77</b>  |
| 5.1 Introduction .....  | 77         |
| 5.2 Experimental Procedure .....                                  | 78         |
| 5.3 Results .....   | 79         |
| 5.3.1 Optical Constants .....                                     | 79         |
| 5.3.2 Growth Rate and Saturation Curves.....                      | 81         |
| 5.3.3 Chemical Composition.....                                   | 83         |
| 5.3.4 Roughness .....   | 86         |
| 5.3.5 Crystallinity.....  | 88         |
| 5.4 Characterization of Cr/ZrO <sub>2</sub> /GaN MOS .....        | 90         |
| 5.5 Growth Mechanism of TALD ZrO <sub>2</sub> : DFT Approach..... | 92         |
| 5.6 Conclusions .....   | 103        |
| <b>6. Atomic Layer Deposition of Hafnium Oxide .....</b>          | <b>105</b> |
| 6.1 Introduction .....  | 105        |
| 6.2 Experimental Procedure and Computational Calculations .....   | 107        |
| 6.3 Results .....   | 107        |
| 6.3.1 Optical Constants .....                                     | 107        |
| 6.3.2 Growth Per Cycle (GPC) .....                                | 110        |
| 6.3.3 Chemical Composition.....                                   | 111        |
| 6.3.4 Roughness and Crystallinity .....                           | 115        |

|  |            |
|--|------------|
| 6.4 Characterization of Cr/HfO <sub>2</sub> /GaN MOS .....         | 117        |
| 6.5 Growth Mechanism of TALD HfO <sub>2</sub> : DFT Approach ..... | 118        |
| 6.6 Conclusions .....  | 128        |
| <b>7. Conclusions and Future Work.....</b>                         | <b>130</b> |
| 7.1 Summary of Contributions to Knowledge.....                     | 133        |
| 7.2 Future Work.....   | 134        |
| <b>Bibliography .....</b>  | <b>136</b> |

## List of Tables

|           |  |    |
|-----------|--|----|
| Table 1.1 | Some GaN characteristics .....   | 4  |
| Table 1.2 | FOM for various semiconductors normalized with respect Si .....  | 5  |
| Table 1.3 | Calculated band offsets of dielectrics on GaN (eV) .....   | 10 |
| Table 1.4 | A summary of some of the properties of dielectric materials used as the gate oxide of the GaN MOSFETs .....            | 15 |
| Table 3.1 | Flow rates of ALD line for deposition of the ALD oxides (sccm) .....   | 34 |
| Table 3.2 | Calibration table for the setpoint of the substrate temperature .....  | 36 |
| Table 3.3 | The temperature of the various parts of the ALD system during the deposition.....                                      | 36 |
| Table 4.1 | Optical bandgap of ALD ZnO at various deposition temperatures .....  | 48 |
| Table 4.2 | Chemical compositions of ZnO films (at.%) deposited at various temperatures using thermal and plasma-enhanced ALD..... | 55 |
| Table 4.3 | RMS Roughness parameters of the TALD and PEALD ZnO deposited at various temperatures.....                              | 56 |
| Table 4.4 | Average grain size of ALD ZnO films (nm).....  | 58 |
| Table 4.5 | Variation of GPC with the substrate temperature for the ALD of ZnO .....   | 64 |

|   |     |
|---|-----|
| Table 4.6 Effect of cluster size on the half-reactions energies and the geometry of structures 6 and 11 .....       | 73  |
| Table 5.1 Chemical composition of zirconium oxide samples deposited by TALD and PEALD at various temperatures ..... | 86  |
| Table 5.2 RMS Roughness of the TALD and PEALD ZrO <sub>2</sub> deposited at various temperatures (nm).....          | 86  |
| Table 6.1 Chemical compositions of hafnium oxide samples deposited by TALD and PEALD at various temperatures .....  | 114 |
| Table 6.2 RMS Roughness of the TALD and PEALD HfO <sub>2</sub> deposited at various temperatures (nm).....          | 115 |

## List of Figures

|  |    |
|--|----|
| Figure 1.1 Schematic diagrams of wurtzite (a) and zincblende (b) crystal structures.....   | 4  |
| Figure 1.2 Schematic view of an n-channel MOSFET. ....   | 6  |
| Figure 1.3 Possible band alignments of two semiconductors in contact: (a) type I, (b) type II, staggered, and (c) type III, broken gap alignments.....   | 10 |
| Figure 1.4 Schematic representation of an ALD cycle. ....  | 16 |
| Figure 1.5 Schematic of ALD window and possible behavior of ALD growth. ..   | 17 |
| Figure 2.1 A system of two nuclei and two electrons. $\alpha$ and $\beta$ are nuclei and i and j represent the electrons in the system.....  | 22 |
| Figure 3.1 Views of (a) the ALD-150LX system and (b) the inside of the ALD cabinet. 1:Load-lock; 2: ALD cabinet; 3: ALD chamber; 4: Plasma Source; 5: Ampoule heater box; 6: Water ampoule. .... | 33 |
| Figure 3.2 Schematic view of the ALD system. ....  | 33 |
| Figure 3.3 A Schematic view of SE.....   | 37 |
| Figure 3.4 A Schematic view of the SE mounted on the ALD chamber. The plasma source on top of the chamber was not shown in this figure.....  | 37 |
| Figure 4.1 Refractive index (a,b) and extinction coefficient (c,d) of TALD (a,c) and PEALD (b,d) ZnO at the deposition temperature. For more clarity   |    |

|   |    |
|---|----|
| the refractive index and extinction coefficient of the samples deposited at 200 °C are shown in (e, f). .....   | 47 |
| Figure 4.2 Illustration of the procedure of finding the optical bandgap of PEALD ZnO at 100 °C. ....  | 48 |
| Figure 4.3 Effect of temperature on the optical bandgap of TALD ZnO deposited at 200 °C.....  | 49 |
| Figure 4.4 Variation of GPC vs. DEZ (a), H <sub>2</sub> O (b), and oxygen plasma (c) exposure times for ALD of ZnO at 100 °C. ....  | 51 |
| Figure 4.5 Variation of GPC with deposition temperature for TALD and PEALD of ZnO. ....   | 52 |
| Figure 4.6 High Resolution XPS graphs of Zn2p (a), O1s (b), and C1s (c), for ALD ZnO with different deposition conditions. ....   | 54 |
| Figure 4.7 Average RMS roughness of the ALD ZnO thin films vs. the deposition temperature.....  | 56 |
| Figure 4.8 AFM surface plots of the ALD ZnO deposited at different temperatures using thermal and plasma-enhanced approaches.....   | 58 |
| Figure 4.9 Average grain size of ALD ZnO films vs. the deposition temperature.  | 59 |
| Figure 4.10 XRD profiles of the TALD and PEALD ZnO samples deposited at various temperatures. ....  | 60 |
| Figure 4.11 Schematic views of crystallites nucleation and growth of ALD ZnO at different deposition conditions. The gray indicates the substrate and the blue represents the ZnO crystallites. At low deposition temperature, the lateral growth is limited by the slow surface diffusion of atoms due to presence of –OH groups. .... | 62 |
| Figure 4.12 Variation of electrical resistivity of TALD ZnO with the deposition temperature. ....   | 63 |

|             |  |    |
|-------------|--|----|
| Figure 4.13 | Reaction pathway of DEZ half-reaction. The white spheres represent H, red: O, black: C, and blue: Zn atoms. The bond lengths and angles are reported in Å and degrees. ....  | 66 |
| Figure 4.14 | Potential energy surface for the DEZ half-reaction. The calculations were carried out at the B3LYP/6-311G(d) level. The enthalpy values are reported at 0 K. For clarity, the ZnO structure in the reactions is shown with a smaller cluster.....  | 67 |
| Figure 4.15 | Reaction pathway of H <sub>2</sub> O half-reaction. The white spheres represent H, red: O, black: C, and blue: Zn atoms. The bond lengths and angles are reported in Å and degrees. ....   | 69 |
| Figure 4.16 | PES of H <sub>2</sub> O half-reaction. All the calculations were carried out at the B3LYP/6-311G(d) level. The enthalpy values are reported at 0 K.  | 70 |
| Figure 4.17 | PES of H <sub>2</sub> O half-reaction and the structure of AS-8, calculated at the B3LYP/6-31G(d) level. The enthalpy values are reported at zero Kelvin. ....   | 70 |
| Figure 4.18 | The structure of the ZnO cluster models, which were used to study the effect of near neighbor atoms on the ZnO ALD half-reactions. .   | 72 |
| Figure 4.19 | Temperature-dependent variation of GPC, and Gibbs free energies of adsorption of DEZ and H <sub>2</sub> O during ALD of ZnO. The rate of variation of GPC with temperature changes approximately at the same temperature that the Gibbs free energies of adsorption of precursors become positive..... | 75 |
| Figure 5.1  | Refractive index (a,b) and extinction coefficient (c,d) of TALD (a,c) and PEALD (b,d) ZrO <sub>2</sub> vs. the incident photon energy and ALD temperatures. For more clarity the refractive index and extinction coefficient of the samples deposited at 200 °C are shown in (e, f).....               | 80 |

|   |    |
|---|----|
| Figure 5.2 Saturation curves for the TDMAZr (a), H <sub>2</sub> O (b), and (c) O <sub>2</sub> -Plasma at 200 °C. ....   | 82 |
| Figure 5.3 GPC of ALD ZrO <sub>2</sub> with deposition temperature for both thermal and plasma-enhanced processes.....  | 83 |
| Figure 5.4 High Resolution XPS graphs of Zr3d (a), O1s (b), and C1s (c) for ALD ZrO <sub>2</sub> at different deposition conditions.....  | 84 |
| Figure 5.5 AFM surface plots of the ALD ZrO <sub>2</sub> deposited at different temperatures using thermal and plasma-enhanced approaches.....  | 87 |
| Figure 5.6 XRD profiles of the ALD ZrO <sub>2</sub> samples deposited by thermal and plasma-enhanced ALD processes at different deposition temperatures.  | 89 |
| Figure 5.7 A schematic model for crystallites nucleation and growth in ZrO <sub>2</sub> and HfO <sub>2</sub> thin films fabricated by ALD. The grey, orange, and black areas show the substrate, amorphous phase, and crystalline phase of the ALD oxides. .... | 90 |
| Figure 5.8 TEM image of Cr/ZrO <sub>2</sub> /GaN MOS structure revealing the polycrystalline microstructure of ZrO <sub>2</sub> and the quality of the ZrO <sub>2</sub> /GaN interface. ....  | 91 |
| Figure 5.9 C-V characteristics of the Cr/P-Zr-100/GaN MOSCAPs.....  | 92 |
| Figure 5.10 Reaction path for first partial reaction of ZrO <sub>2</sub> ALD, involving TDMAZr and Zr-OH* surface reaction sites. The bond lengths are reported in Å and the angles are reported in °. ....   | 94 |
| Figure 5.11 PES of the first partial reaction of the ALD ZrO <sub>2</sub> , between TDMAZr and –OH surface reaction sites. ....   | 95 |

|             |   |     |
|-------------|---|-----|
| Figure 5.12 | Reaction path for second partial reaction of $ZrO_2$ ALD, involving $H_2O$ and $-Zr-(N(CH_3)_2)_3^*$ surface reaction sites. The bond lengths are reported in Å and the angles are reported in °. ....  | 96  |
| Figure 5.13 | PES of the second partial reaction of the ALD $ZrO_2$ , between $H_2O$ and $-Zr-(N(CH_3)_2)_3^*$ surface reaction sites.....  | 97  |
| Figure 5.14 | Reaction pathway for the third partial reaction of $ZrO_2$ ALD, involving $H_2O$ and $-Zr(OH)-(N(CH_3)_2)_2^*$ surface reaction sites. The bond lengths are reported in Å and the angles are reported in °. ....  | 98  |
| Figure 5.15 | PES of the third partial reaction of the ALD $ZrO_2$ , between $H_2O$ and $-Zr-(N(CH_3)_2)_2^*$ surface reaction sites.....   | 100 |
| Figure 5.16 | Reaction path for fourth partial reaction of $ZrO_2$ ALD, involving $H_2O$ and $-Zr(OH)_2-N(CH_3)_2^*$ surface reaction sites. The bond lengths are reported in Å and the angles are reported in °. ....  | 101 |
| Figure 5.17 | PES of the fourth partial reaction of the ALD $ZrO_2$ , between $H_2O$ and $-Zr(OH)_2-N(CH_3)_2^*$ surface reaction sites. ....   | 102 |
| Figure 5.18 | Temperature-dependent variation of GPC, and Gibbs free energies of adsorption of TDMAZr and $H_2O$ during ALD of $ZrO_2$ .....  | 103 |
| Figure 6.1  | Refractive index (a,b) and extinction coefficient (c,d) of TALD (a,c) and PEALD (b,d) $HfO_2$ vs. the incident photon energy at various deposition temperatures. For more clarity the refractive index and extinction coefficient of the samples deposited at 200 °C are shown in (e, f)..... | 109 |
| Figure 6.2  | Variation of GPC with deposition temperature for TALD and PEALD of $HfO_2$ .....  | 111 |

|             |   |     |
|-------------|---|-----|
| Figure 6.3  | High-Resolution XPS profiles of Hf4f (a), O1s (b), C1s (c), and N1s for ALD HfO <sub>2</sub> at different deposition conditions. ....   | 113 |
| Figure 6.4  | AFM surface plots of the ALD HfO <sub>2</sub> deposited at different temperatures using thermal and plasma-enhanced approaches.....   | 116 |
| Figure 6.5  | XRD profiles of the ALD HfO <sub>2</sub> samples deposited by thermal and plasma-enhanced ALD processes at different deposition temperatures.   | 117 |
| Figure 6.6  | C-V characteristics of the Cr/P-Hf-100/GaN MOSCAPs. ....  | 118 |
| Figure 6.7  | Reaction path for first partial reaction of HfO <sub>2</sub> ALD, involving TDMAHf and Hf-OH* surface reaction sites. The bond lengths are reported in Å and the angles are reported in °.....  | 120 |
| Figure 6.8  | PES of the first partial reaction of the ALD HfO <sub>2</sub> , between TDMAHf and -OH surface reaction sites.....  | 121 |
| Figure 6.9  | Reaction path for second partial reaction of HfO <sub>2</sub> ALD, involving H <sub>2</sub> O and -Hf-(N(CH <sub>3</sub> ) <sub>2</sub> ) <sub>3</sub> * surface reaction sites. The bond lengths are reported in Å and the angles are reported in °.....     | 122 |
| Figure 6.10 | PES of the second partial reaction of the ALD HfO <sub>2</sub> , between H <sub>2</sub> O and -Hf-(N(CH <sub>3</sub> ) <sub>2</sub> ) <sub>3</sub> * surface reaction sites. ....   | 123 |
| Figure 6.11 | Reaction path for third partial reaction of HfO <sub>2</sub> ALD, involving H <sub>2</sub> O and -Hf(OH)-(N(CH <sub>3</sub> ) <sub>2</sub> ) <sub>2</sub> * surface reaction sites. The bond lengths are reported in Å and the angles are reported in °. .... | 124 |
| Figure 6.12 | PES of the third partial reaction of the ALD HfO <sub>2</sub> , between H <sub>2</sub> O and -Hf-(N(CH <sub>3</sub> ) <sub>2</sub> ) <sub>2</sub> * surface reaction sites. ....  | 125 |
| Figure 6.13 | Reaction path for fourth partial reaction of HfO <sub>2</sub> ALD, involving H <sub>2</sub> O and -Hf(OH) <sub>2</sub> -N(CH <sub>3</sub> ) <sub>2</sub> * surface reaction sites. The bond lengths are reported in Å and the angles are reported in °.....   | 126 |

|   |     |
|---|-----|
| Figure 6.14 PES of the fourth partial reaction of the ALD HfO <sub>2</sub> , between H <sub>2</sub> O and -Hf(OH) <sub>2</sub> -N(CH <sub>3</sub> ) <sub>2</sub> * surface reaction sites. .... | 127 |
| Figure 6.15 Temperature-dependent variation of GPC, and Gibbs free energies of adsorption of TDMAHf and H <sub>2</sub> O during ALD of HfO <sub>2</sub> .....                                   | 128 |

## **List of Abbreviations**

AFM: Atomic Force Microscopy

ALD: Atomic Layer Deposition

AS: Absorbed State

CL: Cody-Lorentz

CMOS: Complementary Metal–Oxide–Semiconductor

CV: Capacitance-Voltage

CVD: Chemical Vapor Deposition

DEZ: Diethylzinc

DFT: Density Functional Theory

ECP: Effective Core Potential

FOM: Figure of Merit

HF: Hartree-Fock

HFET: Heterojunction Field-Effect-Transistors

LED: Light Emitting Diode

MBE: Molecular Beam Epitaxy

MISFETs: Metal-Insulator-Semiconductor Field-Effect-Transistors

MOSCAP: Metal-Oxide-Semiconductor capacitor

MOSFETs: Metal-Oxide-Semiconductor Field-Effect-Transistors

MSE: Mean Square Error

PEALD: Plasma-Enhanced Atomic Layer Deposition

PECVD: Plasma-Enhanced Chemical Vapor Deposition

RMS: Root Mean Square

SCF: Self-Consistent Field

SE: Spectroscopy Ellipsometry

SEM: Scanning Electron Microscopy

STO: Slater-Type Orbital

TALD: Thermal Atomic Layer Deposition

TDMAHf: tetrakis(dimethylamido)hafnium

TDMAZr: tetrakis(dimethylamido)zirconium

TEM: Transmission Electron Microscopy

TFTs: Thin Film Transistors

TL: Tauc-Lorentz

TS: Transition State

XPS: X-ray Photoelectron Spectroscopy

XRD: X-Ray Diffraction

XRR: X-Ray Reflectivity

XTEM: Cross-Sectional Transmission Electron Microscopy

# Chapter 1

---

## **Introduction**

### **1.1 Background**

Gallium Nitride (GaN) is recognized as one of the best candidates for high-temperature, high-power, and high-frequency metal-oxide-semiconductor field-effect transistors (MOSFETs). Power devices made with GaN have the potential to offer a switching speed with a figure of merit more than 500 times greater than that achievable in silicon. The critical component to enable this technology is the development of a robust oxide with low density of defects and preferential mobility properties that can produce an enhancement mode transistor rather than a depletion mode transistor. However, gate leakage current through the gate oxide and Fermi-level pinning due to large number of interface states at the dielectric/GaN interface limit their usage in such applications. Moreover, the oxides must fulfill various requirements such as a large bandgap to increase the breakdown voltage.

Different methods, such as molecular beam epitaxy (MBE) and plasma-enhanced chemical vapor deposition (PECVD) have been used to deposit high dielectric constant materials on GaN. Atomic layer deposition (ALD) is another thin film deposition technique with the ability of controlling thickness at atomic scale and producing highly conformal films. It is thus an ideal method for deposition of gate oxides of MOSFETs.

Zinc oxide (ZnO) is an alternative wide bandgap semiconductor for GaN. ZnO is recognized for its prospective applications in optoelectronics. ZnO has some advantages over GaN in optoelectronics applications due to its large exciton binding energy (~60 meV), and is widely used as the active channel in thin film transistors (TFTs). ALD of ZnO has been attracted a lot of attention recently.

In this thesis an in-depth investigation of thermal and plasma-enhanced ALD of ZnO is presented. ALD of HfO<sub>2</sub> and ZrO<sub>2</sub> were investigated as promising gate oxides for GaN MOSFETs.

## **1.2 Literature Review**

### **1.2.1 Zinc Oxide (ZnO)**

ZnO has been the center of attention of several studies for decades. The first reports on its characterization go back to 1935 and its crystal structure and optical properties were subject of many studies. A comprehensive review on ZnO materials and devices has recently published by Ozgur et al. [1]. The ZnO properties and structure will be discussed later in Chapter 4, along with a literature review on the ALD of ZnO.

### **1.2.2 Gallium Nitride (GaN)**

The earliest attempt at GaN synthesis dated back to 1932 [2]. Juza and Hahn [3] determined the lattice constant of GaN for the first time. The luminescence properties of GaN were studied by Grimmeiss and Koelmans [4]. However, all of these works studied small crystals in the shape of pellets and needles. Maruska and Tietjen [5] produced epitaxial GaN layers on sapphire and determined that the

direct bandgap of the material to be 3.39 eV at room temperature. Discovery of effective blue electroluminescence property and Light-Emitting Diode (LED) potential motivated many laboratories to synthesize GaN and to investigate its properties [6].

Photonic research led to growth of high-quality GaN with improved electrical properties. It stimulated researchers to study GaN-based materials as a candidate for microwave and high-power high-temperature transistors [7]. High electron mobility and saturation velocity, high sheet carrier concentration at interface, and high breakdown electric field make GaN-based semiconductors ideal for high-power high-temperature applications [8].

The common crystal structures of III-Nitrides are: the wurtzite (WZ), zincblende (ZB) and rocksalt (RS) structures. The degree of ionicity determines which structure will be dominant [9]. For GaN, at room temperature and pressure, the WZ structure is the stable structure, however, the ZB structure is quasistable [10]. Both structures have fourfold coordination (see Figure 1.1). The difference between these two structures is the bond angle of the second-nearest neighbor [11]. The stacking order in WZ is ABABAB along [0001] direction, but in ZB is ABCABC along [111] direction. At high pressure, the RC crystal structure is the stable one [10]. Table 1.1 compares some properties of WZ and ZB GaN.

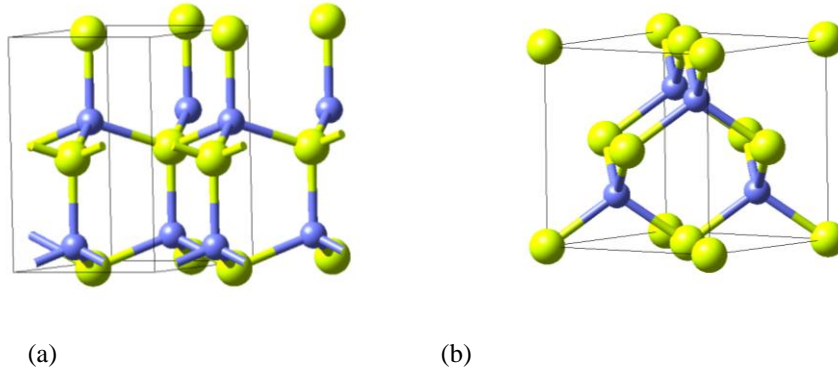


**Figure 1.1** Schematic diagrams of wurtzite (a) and zincblende (b) crystal structures. The dark, and bright spheres represent nitrogen, and gallium atoms, respectively.

**Table 1.1** Some GaN characteristics [12]

| Crystal structure                 | Wurtzite         | Zincblende           |
|-----------------------------------|------------------|----------------------|
| Group of Symmetry                 | $C_{6v}P6_3mc$   | $T_d^2 - F\bar{4}3m$ |
| Density ( $g/cm^3$ )              | 6.15             | 6.15                 |
| <u>Dielectric constant</u>        |                  |                      |
| Static                            | 8.9-9.5          | 9.7                  |
| High frequency                    | 5.35             | 5.3                  |
| Lattice constant ( $\text{\AA}$ ) | a=3.189, c=5.185 | 4.52                 |

### 1.2.3 GaN-Based Transistors

A combination of high current density, high breakdown electric field, and good thermal conductivity can be found in GaN-based transistors [13]. This allows high microwave performance for the solid-state transistors. GaN power devices have the potential to offer a high switching speed and power density with a figure of merit (FOM) greater than 500 times than that achievable in silicon [10].

Several figures of merit (FOM) have been developed for microwave transistors: Johnson's  $(v_{sat}E_c/\pi)^2$ , Baliga's  $(\mu E_c^2)$ , and Keyes' FOM  $(\lambda(v_{sat}/\epsilon_r)^{0.5})$  [13]. Here,  $E_c$  is the breakdown electric field,  $v_{sat}$  is the electron saturation

velocity,  $\mu$  is the electron mobility,  $\epsilon_r$  is the static dielectric constant, and  $\lambda$  is thermal conductivity. Johnson's FOM and Keyes' FOM take into account the high-frequency, high-power capability, and the switching power of the devices, respectively. Baliga's FOM is used to quantitatively evaluate the performance of power MOSFETs by considering on-resistance. Comparing the FOMs for Si, GaAs and GaN in Table 1.2, the superior performance of GaN is obvious (Table 1.2).

**Table 1.2 FOM for various semiconductors normalized with respect Si [14]**

| Material | Johnson's FOM | Keyes' FOM | Baliga's FOM |
|----------|---------------|------------|--------------|
| Si       | 1             | 1          | 1            |
| GaAs     | 7.1           | 0.45       | 11           |
| GaN      | 756           | 1.6        | 77.8         |

A lot of progress has been made in AlGaIn/GaN heterojunction FETs (HFETs) [15-20]. HFETs have the advantage of quantum electron confinement for high electron mobility. However, the gate leakage through the Schottky-barrier gate limits the gate swing. Moreover, depletion mode devices have limited capability in power electronics and are *Normally-On* devices. On the other side, GaN MOSFETs\* provide the capability of fabricating *Normally-Off* devices, with much lower gate-leakage current. The critical component to enable this technology is the development of a robust oxide with low defects and preferential mobility properties that can produce an enhancement mode transistor rather than a depletion mode transistor. In other words, the key parameter in enhancement

\* Also referred to as MISFETs (Metal-Insulator-Semiconductor Field-Effect-Transistors)

mode transistors is the quality of the gate oxide and its compatibility with underlying GaN material.

#### 1.2.4 MOSFET Operation and Interface Oxides

A brief description of MOSFETs operation and their characteristics is discussed in this section. A schematic view of an n-channel MOSFET is shown in Figure 1.2. In the off state, the MOSFET can be considered as two diodes inversely connected in series. No current can pass through the channel in this state. However, by applying a sufficiently large positive voltage to the gate electrode, free electrons, which are minor carriers in p-region, are attracted toward the gate, and an n-channel forms underneath the gate oxide. The minimum required gate voltage to induce the channel is defined as the threshold voltage. At lower voltages, leakage current occurs due to point defects or tunneling of electrons through the gate oxide. By increasing the source-drain voltage at constant gate voltage, the current through channel rises until saturation occurs. Increasing the gate voltage increases the saturation current.

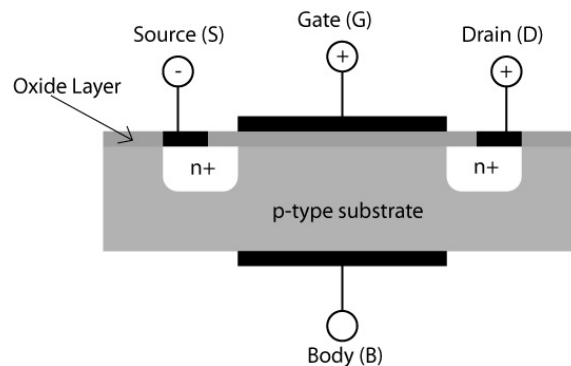


Figure 1.2 Schematic view of an n-channel MOSFET.

The quality of the gate oxide has a lot of influence on the performance of the MOSFET. Trapped charges in gate oxide may degrade the electrical performance. Four types of charges can be found in the gate oxide [21]: (1) Fixed oxide charge, which is the result of structural defects in oxide layer, but it has no interaction with the buried semiconductor. Annealing in N<sub>2</sub> or Ar atmosphere can eliminate these defects. (2) Mobile oxide charge, which comes from ionic impurities like Na<sup>+</sup> and Li<sup>+</sup> ions. (3) Oxide trapped charge, which comes from holes and electrons trapped in bulk oxide due to the ionizing radiation or avalanche injection of carriers from channel. (4) Interface trapped charge, which is due to structural defects at the interface of oxide/semiconductor. The latter is in electrical communication with underlying semiconductor layer and may degrade electrical performance of the device.

Capacitance-Voltage (C-V) curves measured at different frequencies and biases are used to determine the density of interface states. Different methods have been developed for this purpose as discussed in ref. [21]. Interface states also can affect the threshold voltage or cause increase of leakage current. Carriers can jump into interface states and then easily tunnel through the gate oxide. This current is temperature dependent and can be detected through temperature dependent I-V curves [22].

### **1.2.5 Gate Oxide Materials for GaN MOSFETs**

As mentioned earlier, GaN-based MOSFETs have some major advantages over Schottky gate devices. Enhancement-mode MOSFETs have a larger voltage sweep range, lower gate leakage currents, improved thermal stability and higher

temperature operation. Moreover, the circuit design process is simpler since they can be used to form single supply voltage control circuits for power transistors [23, 24]. Moreover, integration of dielectrics can decrease the current collapse by surface passivation, which is the main obstacle of AlGaIn/GaN HFETs [25].

There are two problems with the native oxides of III-V compounds [26]: (1) since they are binary in nature finding a synthesis method for their formation is very difficult, and (2) surface atom bonds have formal fractional occupancy. For example, on the (0001) face in GaN, the formal orbital occupancy for gallium dangling bond is  $3/4$  of an electron, and for nitrogen is  $5/4$  of an electron. As a result, insulators such as  $\text{SiO}_2$  and  $\text{Si}_3\text{N}_4$  cannot form covalent two electron pair bonds between the GaN surface atoms without the creation of charged bonding arrangements. These charged bonds generally degrade interface electronic properties.

Processes like remote plasma ALD, with separate control over interface formation and film deposition can promote the charge distribution on GaN surface and could allow two electrons interfacial bonding between dielectric and GaN [26]. By replacing the  $\text{SiO}_2$  with high- $\kappa$  dielectrics in silicon MOSFETs, silicon has lost some of its advantages over wide bandgap semiconductors, because the high- $\kappa$  dielectrics are not native oxides and can be deposited on any semiconductor [27].

The key guidelines for selecting a high- $\kappa$  gate dielectric are [27, 28]:

- (1) high permittivity, large bandgap, and sufficient band offset ( $>1\text{eV}$ )
- (2) thermal stability

- (3) thermodynamic stability in contact with the semiconductor
- (4) good passivation and interface quality
- (5) compatibility with the current or expected materials to be used in processing for CMOS devices
- (6) process compatibility
- (7) reliability.

Many dielectrics meet some of these requirements but very few materials are favorable with respect to all of the criteria. A summary of these dielectric materials will be presented after describing heterojunction band alignment.

### **1.2.6 Heterojunction Band Alignment**

The band alignment at the interface of GaN/dielectric has an important influence on device performance. As mentioned earlier, large valence and conduction band offsets are required to prevent injection of free electrons and holes [27].

Based on bandgap and electron affinities, three types of band alignments can be formed when two materials with bandgaps are in contact [29]: (1) type I, (2) type II, staggered, and (3) type III, broken gap alignments (Figure 1.3). Direct interaction between semiconductor materials results in space charge redistribution and leads to band bending near the junction. A nominated dielectric should form type I band alignment to reduce the leakage currents in MOSFET device. Table 1.3 shows the band alignment of various oxides on GaN.

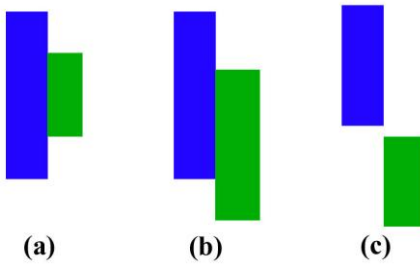


**Figure 1.3 Possible band alignments of two semiconductors in contact: (a) type I, (b) type II, staggered, and (c) type III, broken gap alignments.**

**Table 1.3 Calculated band offsets of dielectrics on GaN (eV) [27]**

| <b>Dielectric</b>              | <b>Conduction Band Offset</b> | <b>Valence Band Offset</b> |
|--------------------------------|-------------------------------|----------------------------|
| HfO <sub>2</sub>               | 1.1                           | 1.6                        |
| ZrO <sub>2</sub>               | 1.1                           | 1.6                        |
| La <sub>2</sub> O <sub>3</sub> | 1.9                           | 0.8                        |
| Sc <sub>2</sub> O <sub>3</sub> | 1.9                           | 0.8                        |
| SrTiO <sub>3</sub>             | -0.1                          | 0.2                        |
| LaAlO <sub>3</sub>             | 1.1                           | 1.3                        |
| Ga <sub>2</sub> O <sub>3</sub> | 0.5                           | 1.1                        |
| Gd <sub>2</sub> O <sub>3</sub> | 1.9                           | 0.7                        |
| SiO <sub>2</sub>               | 2.5                           | 3.2                        |
| Al <sub>2</sub> O <sub>3</sub> | 2.1                           | 3.4                        |

### **1.2.7 Previous Studies on Dielectric Materials for GaN MOSFETs**

#### *Gallium Oxide (Ga<sub>2</sub>O<sub>3</sub>)*

Gallium oxide has been considered as the native oxide of GaN. Thermal oxidation of GaN results in gallium oxide. Both dry and wet oxidations have been tried on GaN [30]. Cross-sectional transmission electron microscopy (XTEM) studies showed that the Ga<sub>2</sub>O<sub>3</sub>/GaN interface is non-uniform. From scanning electron microscopy (SEM), it is found that the films are rough and faceted.

Electrical characterization of the oxide films shows that the breakdown field strengths for dry and wet oxide are 0.2 and 0.1 MV cm<sup>-1</sup>, respectively [30]. Lee et al. [31] studied the performance of GaN MOS devices with Ga<sub>2</sub>O<sub>3</sub> as dielectric grown by a photoelectrochemical method, utilizing a He-Cd laser and H<sub>3</sub>PO<sub>4</sub> solution. The breakdown electric field for this oxide was reported to be 2.80 MV cm<sup>-1</sup> with an interface state density of 2.53×10<sup>11</sup> cm<sup>-2</sup> eV<sup>-1</sup>. It appears that Ga<sub>2</sub>O<sub>3</sub> is not a viable dielectric for GaN [30]. However, Therrien et al. [26] showed significant reduction in interfacial defect densities and redistribution of the surface atom electron charge by forming a GaN/Ga<sub>2</sub>O<sub>3</sub> interface using remote plasma-assisted oxidation (RPAO).

#### ***Gallium Gadolinium Garnet (GGG)***

Due to successful performance of GGG as a gate dielectric in GaAs MOSFETs, attention has turned toward this dielectric for GaN [30]. Amorphous GGG is deposited on GaN by e-beam evaporation of Ga<sub>2</sub>O<sub>3</sub>(Gd<sub>2</sub>O<sub>3</sub>) single crystal [32]. The smoothness of the interface was shown by XRR (X-Ray Reflectivity) and suggested a high carrier mobility and high breakdown electric field. While improvements in leakage current were achieved, the fabricated depletion mode MOSFET could not be modulated at voltages above 3 V.

#### ***Silicon Oxide (SiO<sub>2</sub>)***

Silicon oxide, with a conduction band offset of 3.6 eV and valence band offset of 2.0 eV with GaN, has attracted much attention [33]. Many methods have been used to deposit SiO<sub>2</sub> on GaN. Casey et al. [34] used remote plasma enhanced chemical vapor deposition (PECVD) and found no hysteresis in C-V

measurements. Sawada et al. [35], using the same deposition method, showed an interface state density as low as  $1 \times 10^{11} \text{ eV}^{-1} \text{ cm}^{-2}$ . Despite a low interface state density,  $\text{SiO}_2$  suffers from a low dielectric constant (3.9) that results in high leakage current.

#### ***Silicon Nitride ( $\text{Si}_3\text{N}_4$ )***

Silicon nitride has been extensively used for the passivation of HFET surfaces. Silicon nitride deposited on GaN by electron cyclotron resonance assisted plasma chemical vapor deposition (ECR-PCVD) showed interface state density of  $5 \times 10^{10} \text{ eV}^{-1} \text{ cm}^{-2}$  [36]. However,  $\text{Si}_3\text{N}_4$  forms a type II band alignment with GaN and has a low dielectric constant as 5. As a result, it can only be used as a barrier.

#### ***Aluminum Nitride (AlN)***

Undoped aluminum nitride with a bandgap of 6.2 eV can act as an insulator. The dielectric constant is relatively high, 8-9, and hexagonal aluminum nitride has only 2.4% lattice mismatch with hexagonal gallium nitride on the (0001) plane [37]. In spite of this, AlN has a tendency to deposit with a polycrystalline structure. Unlike amorphous dielectrics, single crystal and polycrystalline AlN films suffer from low breakdown field due to defects and grain boundaries [30]. The AlN deposited by metal-organic molecular beam epitaxy (MOMBE) at 400 °C showed a breakdown field of  $1.4 \text{ MV cm}^{-1}$  [37].

#### ***MgO, and MgCaO Ternary Oxide***

MgO has a bandgap of 8 eV and a dielectric constant of 9.8 and hence it is an alternative gate oxide material for GaN [38]. An interface state density as low as

$2 \times 10^{11} \text{ eV}^{-1} \text{ cm}^{-2}$  was achieved for MgO deposited on GaN using elemental Mg and oxygen plasma [38]. CaO is also a rocksalt dielectric like MgO and has a dielectric constant of 11.8. Although the lattice constant of MgO is smaller than GaN, CaO has larger lattice constant [30]. A ternary oxide consisting of MgO and CaO could thus be closely matched to GaN.  $\text{Mg}_{0.5}\text{Ca}_{0.5}\text{O}$  was found to have the same atomic spacing on (111) plane as GaN [30]. The problem with this material system is that Mg and Ca are immiscible due to the large difference in atomic diameter between Mg and Ca and the film is unstable. Capping the film with stable oxides such as  $\text{Sc}_2\text{O}_3$  can overcome this degradation [39].

### ***Rare Earth Oxides***

Rare earth elements are extremely reactive with oxygen and form very stable oxides. Their cubic and hexagonal phases are interesting as gate oxides for GaN MOSFETs [22]. The rare earth oxides with smaller ionic radii crystallize in the bixbyite structure. The bixbyite crystal structure exhibits similar atomic symmetry in the (111) plane as the GaN (0001), so they could be grown epitaxially on GaN. Another interesting feature of rare earth oxides is their large bandgap, close to 6 eV, and the large band offsets with GaN [22]. The dielectric constant of these oxides is relatively very high ( $\kappa = 7 - 20$ ).

Gadolinium oxide ( $\text{Gd}_2\text{O}_3$ ) is an attractive oxide because of high dielectric constant, 11.4, and a bandgap of 5.3 eV [30]. However, the bond length mismatch between  $\text{Gd}_2\text{O}_3$  (111) and GaN (0001) is about 20% [30]. As a consequence, the dislocations created in the film limit the breakdown field by acting as current leakage paths. Johnson et al. [40] showed that the formation of the stacked gate

dielectric of SiO<sub>2</sub>/Gd<sub>2</sub>O<sub>3</sub> could terminate the formation of the dislocations in the crystalline oxides. The high melting point of these materials suggests high thermal stability.

Scandium Oxide (Sc<sub>2</sub>O<sub>3</sub>) has a much smaller lattice constant than Gd<sub>2</sub>O<sub>3</sub> (9.2% mismatch to GaN), which should make it less defective when deposited on GaN [30]. It has a bandgap of 6.3 eV and a dielectric constant of 14 [30]. Sc<sub>2</sub>O<sub>3</sub> has been grown epitaxially on GaN using MBE [41]. The results showed that a GaO<sub>x</sub> passivation layer is needed to allow for a suitable growth of the epitaxial oxide on GaN and to achieve low leakage current densities. From the I–V and C–V data, a forward breakdown field of 0.7 MV cm<sup>-1</sup> and an interface state density 4×10<sup>11</sup> eV<sup>-1</sup> cm<sup>-2</sup> were calculated [42]. Lanthanum Oxide (La<sub>2</sub>O<sub>3</sub>) is also among the rare earth oxides deposited on GaN [30, 43, 44]. However, the rare earth oxides are hygroscopic [22]. They become hydrated and carbonated in contact with atmosphere at ambient pressure and temperature. In fact, the OH<sup>-</sup> can easily bond to the rare earth atom. Hydroxide contamination results in degradation of the dielectric constant [22].

#### *Aluminum Oxide (Al<sub>2</sub>O<sub>3</sub>)*

Al<sub>2</sub>O<sub>3</sub> is attractive due to its large bandgap, 9 eV, and high breakdown field, ~10 MV cm<sup>-1</sup> [23, 45, 46]. To date MBE [47] and MOCVD [48] have been used to deposit alumina on GaN. One of the advantages of Al<sub>2</sub>O<sub>3</sub> is that it can easily be deposited using atomic layer deposition (ALD) and hence it can have all the advantages of ALD, which are discussed in next section. For example, Ye et al. [45] deposited alumina on GaN using ALD at 300 °C. The midgap interface trap

density was found to be  $10^{11} - 10^{12} \text{ eV}^{-1} \text{ cm}^{-2}$ . Wu et al. [49] made a GaN MOSFET with ALD  $\text{Al}_2\text{O}_3$  as its gate oxide and measured a leakage current less than  $10^{-6} \text{ mA mm}^{-1}$  at a gate voltage of 4V, one order of magnitude less than that of  $\text{Gd}_2\text{O}_3$ . Using remote-plasma ALD, Yun et al. [46] achieved a MOS structure with a leakage current density as low as  $10^{-10} \text{ A cm}^{-2}$  at  $1 \text{ MV cm}^{-1}$  and an interface state density about  $1.2 \times 10^{11} \text{ eV}^{-1} \text{ cm}^{-2}$ . Compared to rare earth oxides, however, the dielectric constant of alumina,  $\sim 9$ , is low.

The properties of the different dielectric materials used as the gate oxide of the GaN MOSFETs are summarized in table 1.4.

**Table 1.4 A summary of some of the properties of dielectric materials used as the gate oxide of the GaN MOSFETs**

| <b>Material</b>         | <b>Bandgap<br/>(eV)</b> | <b>Dielectric<br/>Constant</b> | <b>Breakdown voltage<br/>(MV cm<sup>-1</sup>)</b> | <b>Defect Density<br/>(eV<sup>-1</sup> cm<sup>-2</sup>)</b> | <b>Mismatch<br/>to GaN (%)</b> |
|-------------------------|-------------------------|--------------------------------|---|---|--------------------------------|
| $\text{Ga}_2\text{O}_3$ | 5                       | 10                             | 0.1 – 2.8   | $2.53 \times 10^{11}$                                       | -                              |
| $\text{SiO}_2$          | 9                       | 3.9                            | -   | $1 \times 10^{11}$  | -                              |
| $\text{Si}_3\text{N}_4$ | 5                       | 5                              | -   | $5 \times 10^{10}$  | -                              |
| AlN                     | 6.2                     | 8 – 9                          | 1.4   | -   | 2.4                            |
| MgO                     | 8                       | 9.8                            | -   | $2 \times 10^{11}$  | -                              |
| $\text{Gd}_2\text{O}_3$ | 5.3                     | 11.4                           | -   | -   | 20                             |
| $\text{Sc}_2\text{O}_3$ | 6.3                     | 14                             | 0.7   | $4 \times 10^{11}$  | 9.2                            |
| $\text{Al}_2\text{O}_3$ | 9                       | 9                              | 1-10  | $10^{11}$ - $10^{12}$                                       | -                              |

### 1.2.8 Atomic Layer Deposition (ALD) of Oxides

Atomic layer deposition (ALD) is a key method for depositing of thin films. The International Technology Roadmap for Semiconductors (ITRS) [50] included ALD as a method for fabricating high- $\kappa$  dielectric gate oxides in MOSFET structures. In ALD, precursors are introduced sequentially into a reactor at low

pressures, ~1 torr. Each reactant pulse is followed by a purge step to sweep out the excess reactants and byproducts (See Figure 1.4). ALD is a self-limiting process with a subnanometer control over thickness of layers, with uniform and conformal thin films.

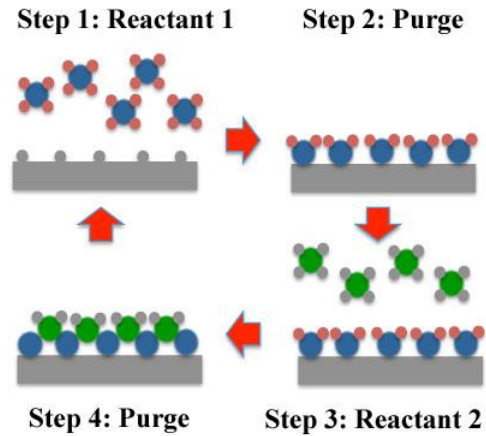


**Figure 1.4 Schematic representation of an ALD cycle.**

Conformality is a key characteristic because unlike the traditional semiconductor technology, the basic building blocks for nanotechnology are not limited to planar type substrates [51]. Another characteristic of ALD is its control over thickness and composition [51]. This makes ALD an ideal technique for depositing high- $\kappa$  dielectrics gate oxides for MOSFET applications. The other feature of ALD is that it is fundamentally a low-temperature deposition technique [51]. For example, ALD of  $\text{Al}_2\text{O}_3$  at 33 °C has been reported by Groner et al. [52]. This feature is more important for depositing polymers and low-k dielectric materials.

The processing temperature range for ALD is called the ALD window. At lower temperatures the reactants may condense on the surface, or the surface

reactions may not have enough thermal energy to proceed [53]. At higher temperatures decomposition or desorption of surface species occurs and the growth rate decreases [53]. A schematic of the ALD window has shown in Figure 1.5.

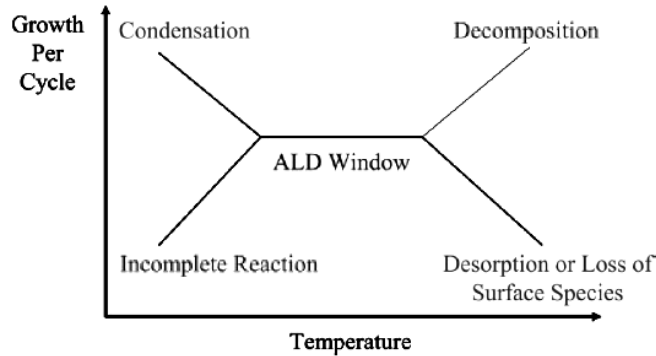


**Figure 1.5 Schematic of ALD window and possible behavior of ALD growth.**

With utilization of ALD in large-scale production for Si-based integrated circuits, attention has been attracted to using ALD for depositing high- $\kappa$  dielectrics on Ge and III-V materials [54]. The native oxide on the surface of III-V semiconductors has a significant impact on the interface state density and results in poor device performance due to Fermi level pinning [54].

$\text{Al}_2\text{O}_3$ ,  $\text{HfO}_2$ , and  $\text{HfAlO}$  ( $\text{Al}_2\text{O}_3/\text{HfO}_2$ ) are among the gate oxide materials deposited by ALD on III-V semiconductors [54]. A lot of progress has been made in understanding the effect of the chemistry of the oxide/semiconductor interface on electrical performance such as Fermi level pinning and the nature of the associated defect states [54]. However, more effort is needed to enable the realization of high-performance MOSFETs using III-V semiconductors. An

introduction and a literature review of ALD of  $ZrO_2$  and  $HfO_2$  are discussed in Chapters 5 and 6, respectively.

### **1.3 Objectives of This Work**

In the last decade, ALD has recently been recognized as an ideal tool for depositing high- $\kappa$  materials on silicon. However, few studies have been done on ALD of high- $\kappa$  dielectrics on GaN.  $HfO_2$  and  $ZrO_2$  are two promising high- $\kappa$  materials, which have rarely been studied for the application as a gate oxide of GaN and ZnO. A fundamental understanding of the nucleation and growth mechanisms is required to control the quality of the ALD oxides and developing new applications. Meanwhile, there is a lack of a systematic study on growth mechanisms and characteristics of  $HfO_2$  and  $ZrO_2$  as well as ZnO thin films deposited by ALD. Two different approaches were used to tackle this problem. In the first approach, different analytical tools including X-ray diffraction (XRD), X-ray photoelectron spectroscopy (XPS), atomic force microscopy (AFM), transmission electron microscopy (TEM), *in-situ* spectroscopy ellipsometry, Hall mobility and four-point probe techniques were used to investigate the  $HfO_2$ ,  $ZrO_2$ , and ZnO thin films properties. The growth models were proposed for ALD of the oxide based on the experimental results. In the second approach, density functional theory (DFT) was utilized to explore the reaction pathways between the precursor molecules and the oxide surface, and to compute the thermodynamic stability of intermediate states and activation energies of various reactions at the deposition temperature and pressure. Finally, metal-oxide-semiconductor capacitors (MOSCAPs) were fabricated and capacitance-voltage (C-V)

measurements were performed on the structure to study the quality of the interface between the semiconductor and high- $\kappa$  oxides.

## **1.4 Outline of Thesis**

An introduction on ALD, GaN, ZnO, and the high- $\kappa$  oxides was presented in this chapter. The objective and the roadmap to tackle the problems were offered as well. Chapter 2 is a brief introduction to the quantum chemical modeling and density functional theory, which are utilized in chapters 4-6 to study the reaction pathways of the ALD oxides. Chapter 3 outlines the experimental procedure and techniques used to explore the ALD oxides. Chapter 4, 5, and 6 discuss a thorough and comprehensive study on characterization of structure, morphology, and chemistry of ZnO, ZrO<sub>2</sub>, and HfO<sub>2</sub> deposited by thermal and plasma-enhanced ALD methods. Chapter 7 introduces the novel method for investigation of nucleation and growth mechanism of ALD oxides utilizing *in-situ* spectroscopic ellipsometry. The overall conclusion of this work is summarized in Chapter 8, along with suggestions for future work.

## Chapter 2

---

# Theoretical Background of Quantum Chemistry

## Calculations

In the early twentieth century, physicists discovered that Newton's classical mechanics did not properly describe the behavior of a system containing very small particles. The groundbreaking contributions of Planck, Einstein, Bohr, Heisenberg, Born, Jordan, Pauli, Fermi, Schrödinger, Dirac, de Broglie and Bose led to discovery of *quantum mechanics*, which described the behavior of such systems. Pauling, Hartree, Fock, Slater, Thomas, Fermi, Bloch, Dirac, Wigner, and Mulliken applied quantum mechanics to the problems in chemistry and laid the foundation of modern *computational quantum chemistry*.

This chapter provides an introductory summary to the theory underlying computational chemistry. The emphasis is on the molecular electronic structure, energetic, geometry and vibrational calculations. More detailed knowledge of quantum chemistry can be found in “Quantum Chemistry” by Levin [55].

### 2.1 Schrödinger Equation for a Many-Body System

To describe the state of a system in quantum mechanics, we have to find the *state function or wave function*,  $\Psi(r, t)$ , of that system.  $\Psi(r, t)$  is a function of the coordinates of the particles in the system and time, and contains all the possible information about the system. The fundamental equation of quantum chemistry is the *Schrödinger wave equation* or *time-dependent Schrödinger equation*.

Analogous to Newton's second law in classical mechanics, the Schrödinger wave equation tells us how to find the future state of a quantum-mechanical system from knowledge of its present state:

$$-\frac{\hbar}{i} \frac{\partial \Psi(r,t)}{\partial t} = \hat{H} \Psi(r,t) \quad (2.1)$$

where  $\hat{H}$  is the Hamiltonian operator,  $i = \sqrt{-1}$ , and  $\hbar$  (*h-bar*) is defined as

$$\hbar = \frac{h}{2\pi} \quad (2.2)$$

The Hamiltonian operator is the total energy operator and consists of kinetics,  $\hat{T}$ , and potential energy,  $\hat{V}$ , operators:

$$\hat{H} = \underbrace{-\frac{\hbar^2}{2m} \nabla^2}_{\hat{T}} + \underbrace{V(r,t)}_{\hat{V}} \quad (2.3)$$

where  $m$  is the mass of the particle and the Laplace operator,  $\nabla^2$ , is the second order differential operator with respect to coordinates of nuclei and electrons.

The time-dependent Schrödinger equation looks formidable. Fortunately, for many problems in quantum chemistry, where the potential energy  $V$  is not a function of time, the simpler *time-independent Schrödinger equation* is applicable:

$$\hat{H} \Psi(r) = E \Psi(r) \quad (2.4)$$

where  $E$  is the energy of the system.

For a system of  $N$  nuclei and  $n$  electrons, as shown in Figure 2.1, the corresponding Hamiltonian is written as following:

$$\hat{H} = -\sum_{\alpha=1}^N \frac{\hbar^2}{2M_{\alpha}} \nabla_{\alpha}^2 - \sum_{i=1}^n \frac{\hbar^2}{2m_i} \nabla_i^2 + \sum_{\alpha=1}^N \sum_{\beta>\alpha}^N \frac{Z_{\alpha} Z_{\beta} e^2}{r_{\alpha\beta}} + \sum_{i=1}^n \sum_{j>i}^n \frac{e^2}{r_{ij}} - \sum_{\alpha=1}^N \sum_{i=1}^n \frac{Z_{\alpha} e^2}{r_{\alpha i}} \quad (2.5)$$

where  $M_\alpha$  and  $Z_\alpha$  are the mass and the atomic number of nucleus  $\alpha$ .  $r$  is the distance between nuclei, between electrons, and between electrons and nuclei as defined in Figure 2.1. The two first terms in equation 2.5 are the kinetic energy of nuclei and electrons, respectively. The third and fourth terms are the coulomb repulsion between nuclei and between electrons, correspondingly. The fifth term is the coulomb attraction between nuclei and electrons.

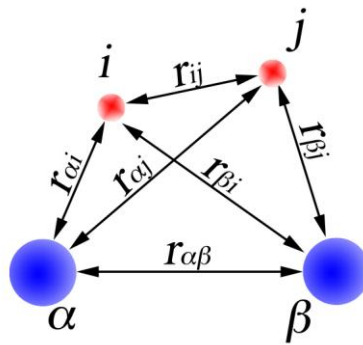


**Figure 2.1** A system of two nuclei and two electrons.  $\alpha$  and  $\beta$  are nuclei and  $i$  and  $j$  represent the electrons in the system.

## 2.2 Born-Oppenheimer Approximation and Variational Theorem

Equation 2.5 is difficult to solve. However, because the nuclei are much heavier than electrons and hence move more slowly, the electrons can be considered to be moving in the potential field of fixed nuclei. This approximation is referred to as the *Born-Oppenheimer Approximation*. With this approximation, the kinetic energy of nuclei can be abandoned and the repulsion between nuclei can be treated as a constant value. As a result, the electronic wave function and its energy can be obtained by solving the *electronic Schrödinger equation*:

$$\hat{H}_{elec}\psi_{elec}(r) = E_{elec}\psi_{elec}(r) \quad (2.6)$$

where the electronic Hamiltonian,  $\hat{H}_{elec}$ , is

$$\hat{H}_{elec} = -\sum_{i=1}^n \frac{\hbar^2}{2m_i} \nabla_i^2 + \sum_{i=1}^n \sum_{j>i}^n \frac{e^2}{r_{ij}} - \sum_{\alpha=1}^N \sum_{i=1}^n \frac{Z_{\alpha}e^2}{r_{\alpha i}} \quad (2.7)$$

Solving the electronic Schrödinger equation is still a challenging task. However, we can make approximate solutions by employing the *variational theorem*. The variational theorem states that any approximate wave function has an energy that is above or equal to that of the exact wave function energy and the equality stands for the exact solution. Practically, a trial wave function is chosen and then the variational theorem is used to indicate accuracy of the trial: the lower the calculation energy, the closer the trial wave function to the real solution.

The common approach is to construct a trial wave function as a linear combination of *basis functions*,  $\varphi_i$ ,

$$\psi_t = \sum_i c_i \varphi_i \quad (2.8)$$

The task is to find the optimum set of basis function coefficient,  $\{c_i\}$ , which gives the lowest possible energy.

### 2.3 Basis Functions

Two most common basis functions are Slater-type functions and Gaussian-type functions. The Slater-type has the form of

$$\varphi_{slater} = e^{-\zeta|r-R_A|} \quad (2.9)$$

and the Gaussian-type function has the form of

$$\varphi_{gaussian} = e^{-\alpha|r-R_A|^2} \quad (2.10)$$

$\zeta$  and  $\alpha$  are Slater and Gaussian orbital exponents. The orbital exponents determine the diffuseness of the basis functions. A small exponent results in a large dense function. The differences between these two type of basis functions occur at  $r = R_A$ , where the Gaussian function has a slope of zero while the Slater functions has a finite slope. Moreover, at large values of  $|r - R_A|$  the Gaussian function falls off more rapidly. In spite of Slater functions, which can only be computed numerically, the integral over Gaussian functions can be solved analytically and this means much faster calculations. However, it is worthy to mention that the exact solution to the Schrödinger equation for the hydrogen atom is a Slater-type orbital (STO). For a better description of the shape of molecular orbitals using the Gaussian functions, a linear combination of the *primitive functions* are used to construct a *contracted Gaussian function*.

Larger basis sets describe molecule orbitals better as they enforce fewer restrictions on the location of the electrons in space. One method is to use more than one basis set to describe each valence orbital. These sets of functions are called split valence basis sets. Adding *polarization functions*, with higher angular momentum, and *diffuse functions*, which allows orbitals to span a larger space, are other ways to improve the basis functions. For the atoms beyond the third row of periodic table, it is common to use *effective core potentials (ECP)*. The ECP describes the electrons near the nucleus while the Gaussian basis functions depicts the valence electrons.

Basis sets denoted by the general nomenclature N-M1G or N-M11G, where N and M are integers. The G in the name simply indicates the Gaussian basis

functions. The N-M1G is a split valence double zeta basis set while the N-M11G is a split valence triple zeta basis set. As an example, in the split valence double zeta basis set 6-31+G(d,p) basis set for carbon atom, N=6 represents the number of the Gaussian functions to describe the core orbital, 1s. M=3 indicates the number of Gaussian primitives to describe 2s and 2p orbitals. The “1” means one Gaussian primitive is used to define the 2s’ and 2p’ basis functions. (d,p) shows that one set of d-type polarization functions is added to all non-hydrogen atoms and one set of p-type polarization functions is added to hydrogen atoms. The + sign means that one set of sp-type diffuse basis functions is added to non-hydrogen atoms. To summarize this example, the 6-31+G(d,p) basis set for carbon contains 19 basis functions and 32 primitive functions:

*1s (6 primitives)*

*2s, 2p, 2p, 2p (4×3=12 primitives)*

*2s’, 2p’, 2p’, 2p’ (4×1=4 primitives)*

*3d, 3d, 3d, 3d, 3d, 3d (6×1=6 primitives)*

*2s+, 2p+, 2p+, 2p+ (4×1=4 primitives)*

## **2.4 Molecular Orbital Methods – Hartree-Fock**

Solving the Schrödinger equation for a molecule is a many-body problem and is difficult to solve. The Hamiltonian depends on the wave function and vice versa because of the two-electron repulsion term. The simplest approach is to overlook this term. In this case, similar to the total probability of the independent events, the wave function of the non-interacting electrons is the product of each single electron wave function, which is called the *Hartree product*. However, the

Hartree product does not satisfy the antisymmetry principle. The antisymmetry principle states that the wave function changes sign with respect to the interchange of any two electrons.

The next approach is to use the Slater determinant:

$$\psi(x_1, x_2, x_3, \dots, x_n) = \frac{1}{\sqrt{n!}} \begin{vmatrix} \psi_i(x_1) & \psi_j(x_1) & \dots & \psi_k(x_1) \\ \psi_i(x_2) & \psi_j(x_2) & \dots & \psi_k(x_2) \\ \vdots & \vdots & \ddots & \vdots \\ \psi_i(x_n) & \psi_j(x_n) & \dots & \psi_k(x_n) \end{vmatrix} \quad (2.11)$$

In the Slater determinant each row involves the same electron and each column involves the same orbital. The Slater determinant satisfies both the antisymmetry principle and the Pauli exclusion principles of quantum mechanics. Moreover, it also stratifies the indistinguishability of the electrons.

In the Hartree-Fock (HF) method, the full Hamiltonian is replaced by the sum of the one-electron Hamiltonians where an electron encounters an average potential of the other electrons,  $V_{HF}$ , and the fixed nuclei. The HF method uses an iterative procedure. This procedure is called the self-consistent-field (SCF):

1. Guess the basis function coefficients for the trial wave function.
2. Calculate the average potential field seen by each electron.
3. Solve the Fock equation for the trial wave function:

$$F_i \psi_i(x_1) = \varepsilon \psi_i(x_1) \quad (2.12)$$

where  $F_i$  is the Fock operator

$$F_i = -\frac{\hbar^2}{2m} \nabla_i^2 - \sum_{\alpha=1}^N \frac{Z_{\alpha} e}{r_{i\alpha}} + V_{HF}^i \quad (2.13)$$

4. Minimize the expectation value of the Fock operator,  $F_i$ , with respect to the basis set coefficients and construct a new set of orbitals and new trial wave function.
5. Calculate the new  $V_{HF}$  from the new trial function and repeat steps 3 and 4 until the potential field and the wave function do not change.

The HF method neglects electron correlation and this can cause a large deviation from the exact solution. Modern methods are implemented to account for the correlation and coupling effects. These methods are categorized as post-HF methods. More description of these methods can be found in quantum chemistry textbooks [55].

## 2.5 Density Functional Theory

Unlike the HF and post-HF methods, density functional theory (DFT) does not calculate the wave function of the electrons. DFT is based on two theorems, known as the Hohenberg-Kohn theorems [56]:

*“1. Knowing the ground-state density,  $n_0(\mathbf{r})$ , it is possible to drive the corresponding wave function. It means that the ground-state wave function is a functional of electron density,  $\rho(\mathbf{r})$ .*

*2. The electron density that minimizes the energy of the overall functional is the exact electron density corresponding to the full solution of the Schrödinger’s equation.”*

Unfortunately, the Hohenberg-Kohn theorems do not describe how to find the electron density, or how to calculate the energy from the electron density. This was done by Kohn and Sham in 1965 [57].

The energy of the system,  $E_{KS}$ , can be written as:

$$E_{KS} = T + V_{e-n} + V_{e-e} + E_{xc} \quad (2.14)$$

where  $T$  is the electronic kinetic energy,  $V_{e-n}$  is the electronic potential energy from attraction of electrons and nuclei,  $V_{e-e}$  is the electronic potential from repulsion of electrons, and  $E_{xc}$  is the exchange-correlation energy.

To determine the energy, the Kohn-Sham equation has to be solved using the variational principle:

$$\left\{ -\frac{\hbar^2}{2m} \nabla_i^2 - \sum_{\alpha} \frac{Z_{\alpha} e^2}{r_{\alpha}} + \int \frac{\rho(r_j) e^2}{r_{ij}} + V_{xc}(r_i) \right\} \psi_i(r_i) = \varepsilon_i \psi_i(r_i) \quad (2.15)$$

where  $\psi_i$  is the Kohn-Sham orbital. The electronic density is calculated using:

$$\rho(r) = \sum_i |\psi_i(r_i)|^2 \quad (2.16)$$

and the exchange-correlation potential,  $V_{xc}$ , is found using:

$$V_{xc} = \frac{\delta E_{xc}[\rho]}{\delta \rho} \quad (2.17)$$

The only unknown is the exchange-correlation energy functional. The improvements in  $E_{xc}$  lead to improvement in the calculated properties and energy of the system under study.

*Local density approximation (LDA)* assumes a uniform electron gas of the same density in the molecule [58]. However, in real molecules the electron gas is not uniform. This resulted in the introduction of the *generalized gradient approximation (GGA)* that involves the gradient corrections.

Another method, known as *Hybrid DFT*, involves the combination of exchange-correlation functional from DFT approaches and HF method. The well-known B3LYP [59-62] method, the most popular DFT method, is an example of this approach.

## 2.6 Geometry Optimization and Frequency Calculations

To find the stable or transition structure of the molecules, the stationary points on the *potential energy surface (PES)* must be found. This is done by performing the *geometry optimization*. PES relates the energy of the system to its molecular configuration, or the nuclei positions. The stable configuration and the transition state are considered as the minimum and the first saddle point, respectively. At both of these configurations the first derivative of energy, which is proportional to the force, is zero. A geometry optimization begins with finding the electronic structure of molecular structure. Then, the gradient of the PES is calculated. The later determines the direction to a stationary point on the PES, which is the new structure. The energy and forces are calculated for this new structure and the procedure repeats until:

1. The maximum force is less than a maximum value.
2. The root mean square (RMS) of the forces is less than a maximum value.
3. The maximum displacement is less than a maximum value.
4. The root mean square (RMS) of the displacements is less than a maximum value.

At this final structure the vibrational frequencies are computed by taking the second-derivative of the energy with respect to the nuclei positions. For the stationary point, all the frequencies must be real. However, for the transition structure, there must be exactly one imaginary frequency [63].

## 2.7 Computational Chemistry Approach to Atomic Layer Deposition

Computational Chemistry has been used to model ALD chemistry of different oxides, and nitrides. From these studies the activation energies of the ALD half-reactions have been computed and the most probable reaction pathways have been found. These data can be used to design new precursors and to provide validation for models. A review on the existing papers in this topic is published by Elliott [64].

Simulation of the ALD reactions can be classified into two categories: *homodeposition* or *product-on-product*, and *heterodeposition* or *product-on-substrate*. The homodeposition refers to the steady-state part of the ALD where the growth rate is constant. The aim of these studies is to find the desirable and undesirable reaction pathways. These data provide to understanding on how the surface reaction sites are consumed and to find the stability of the intermediate complexes formed during ALD half-reactions. Quantitative answers can lead to prediction of growth rate, and its dependence on temperature and dose/purge times.

On the other hand, the heterodeposition refers to the stage where the reactions are between the substrate, for example Si(100) surface, and the ALD precursors. The results of these simulations have been used to determine the influence of reaction site chemistry, for example –H terminated vs. –OH terminated, to control the interface at atomic levels, and to observe the cleaning effect of the precursors.

## 2.8 Computational Method in This Thesis

Computational chemistry calculations have been performed to aid interpretation of the experimental results. The homodeposition of zinc oxide, zirconium oxide, and hafnium oxide was studied by employing the cluster approximation to represent the oxide surface on which the reactions occur. The cluster approximations are explained later in the appropriate sections. GAUSSIAN 09 was used to perform molecular orbital calculations. The geometry of stationary points was located using the B3LYP gradient corrected density functional method. 6-311G(d) and 6-31+G(d,p) basis sets were used to describe the Zn, O, N, C, and H atoms. The LanL2DZ ECP basis set was used for Hf and Zr atoms. The tight optimization convergence criteria (OPT=TIGHT) and ultrafine grid (INT=ULTRAFINE) were used for calculations in ZrO<sub>2</sub> and HfO<sub>2</sub> systems. The frequency calculations were carried out at the same level of theory to identify the nature of the stationary points (local minima and transition states) and to calculate the zero-point energy corrections, and the thermal corrections at ALD temperature and pressure. All energies reported were corrected by the zero-point energy correction value. To be consistent with the most the literature cited in this thesis, we used "kcal/mol" unit to report the calculated energies. In order to test the validity of the calculations, the results were compared with available experimental data whenever possible.

## Chapter 3

---

### Experimental Procedures

This chapter presents the methods used to prepare and characterize the samples using fabricated with ALD. The detailed descriptions of the ALD system and the characterization methods utilized to quantify the samples are also discussed.

#### 3.1 ALD Reactor

All ALD samples were deposited in an ALD-150LX from Kurt J. Lesker Company. This reactor is capable of thermal and plasma-enhanced ALD. A picture of the reactor is shown in Figure 3.1. The samples were loaded into a load-lock connected to the ALD chamber. The load-lock was then evacuated to  $10^{-7}$  torr of vacuum to protect the ALD chamber from contamination.

A schematic view of the ALD is shown in Figure 3.2. The use of high-speed valves in ALD-150LX reactor let the most efficient use of the precursors, with a dose time as low as 20 ms. Inert gases, Ar or N<sub>2</sub>, always flow in the reaction lines to prevent any backflow of the precursors or byproducts from the chamber. The ALD ampoules are heated to provide sufficient vapor pressure of the precursors, if required. During the dose time, the ALD mass flow control (MFC) valves open for a specific time and the Ar flow delivers the precursor vapor to the showerhead in the main chamber.

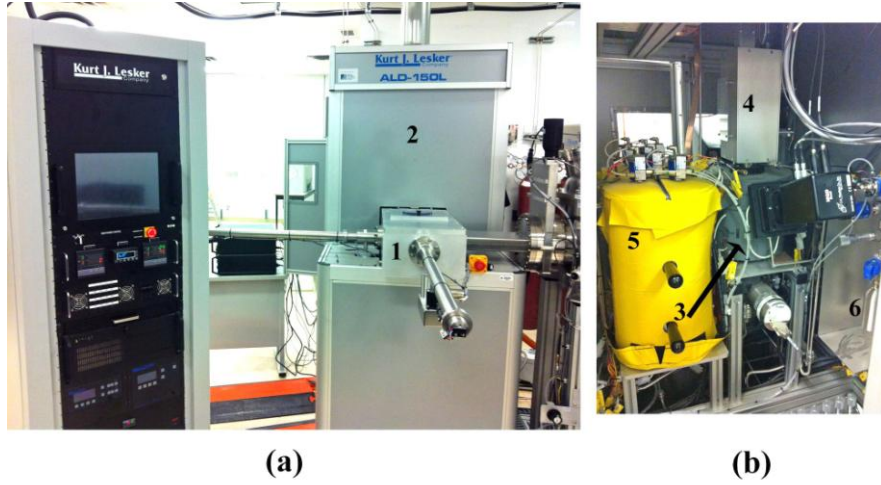


Figure 3.1 Views of (a) the ALD-150LX system and (b) the inside of the ALD cabinet.  
 1: Load-lock; 2: ALD cabinet; 3: ALD chamber; 4: Plasma Source; 5: Ampoule heater box;  
 6: Water ampoule.

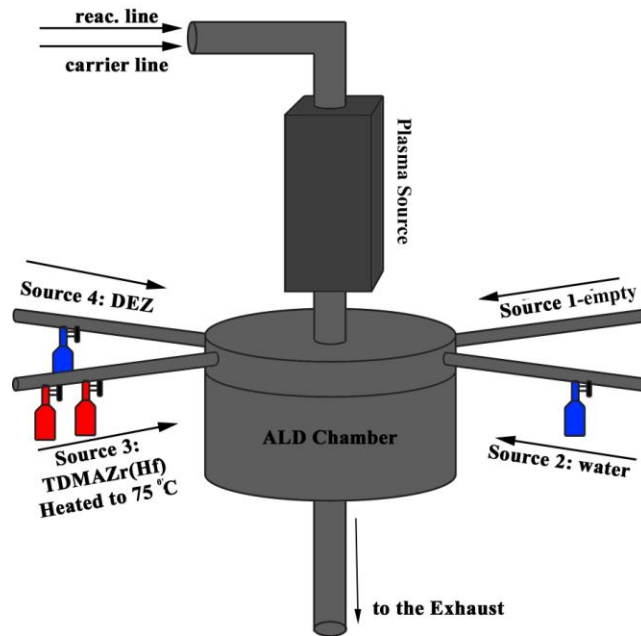


Figure 3.2 Schematic view of the ALD system.

The ALD chamber walls and the spectroscopic ellipsometry ports are protected from any deposition by a flow of inert gas at 500-600 sccm. The flow rate of the gas in the reaction lines that are not in use is 10 sccm to prevent any back streaming. In the thermal process, where the plasma source is not in use, Ar flows at 250 sccm through the plasma source for the same reason. However, in the plasma-enhanced process a mixture of Ar at 100 sccm and O<sub>2</sub> at 60 sccm is used. Table 3.1 summarizes the flow rates in each ALD lines for both thermal and plasma-enhanced ALD of ZnO, HfO<sub>2</sub> and ZrO<sub>2</sub>.

**Table 3.1 Flow rates of ALD line for deposition of the ALD oxides (sccm)**

| Line                          | Flow rate |                                    |       |                                    |
|-------------------------------|-----------|------------------------------------|-------|------------------------------------|
|                               | TALD      |                                    | PEALD |                                    |
|                               | ZnO       | HfO <sub>2</sub> -ZrO <sub>2</sub> | ZnO   | HfO <sub>2</sub> -ZrO <sub>2</sub> |
| Curtain                       | 600       | 600                                | 500   | 500                                |
| Purge 1                       | 300       | 300                                | 250   | 250                                |
| Purge 2                       | 150       | 150                                | 150   | 150                                |
| Source 1 - Empty              | 15        | 15                                 | 15    | 15                                 |
| Source 2 – H <sub>2</sub> O   | 80        | 80                                 | 15    | 15                                 |
| Source 3 – TDMAZr, TDMAHf     | 15        | 80                                 | 15    | 80                                 |
| Source 4 – DEZ                | 80        | 15                                 | 80    | 15                                 |
| Plasma Source – Carrier       | 250       | 250                                | 100   | 100                                |
| Plasma Source – Reactant line | 0         | 0                                  | 60    | 60                                 |

The plasma was created in an inductively coupled plasma source at a power of 600 W with a ramp of 6000 W/s. The plasma process occurred at a total pressure of 1.1 torr. This combination of power and pressure guaranteed the formation of remote plasma (H-Mode) [65].

### 3.2 Sample Preparation

Lightly doped p-type Si(100) wafers, 10  $\Omega$  cm resistivity, were cut using a diamond saw into 2<sup>cm</sup>×2<sup>cm</sup> pieces. The substrates were cleaned using piranha solution (H<sub>2</sub>SO<sub>4</sub>:H<sub>2</sub>O<sub>2</sub> 3:1 mixture) for 15 minutes to remove any organic contamination on the surface.

High purity Ar (5.0 purity, Praxair) was used as the carrier gas in the ALD reactor. Diethylzinc (DEZ), tetrakis(dimethylamido)hafnium (TDMAHf), and tetrakis(dimethylamido)zirconium (TDMAZr), all from Sigma-Aldrich, were used as the metalorganic precursors. Deionized Water (H<sub>2</sub>O: Optima LC/MC, Fisher Scientific, 18M  $\Omega$ ) and remote oxygen plasma were used as the oxidizing agents for thermal and plasma-enhance ALD, respectively. The H<sub>2</sub>O and DEZ ampoules were kept at 25 °C, while the TDMAHf and TDMAZr ampoules heated to 75 °C to maintain the vapor pressure of the precursors constant during the deposition. All the ALD valves and reaction lines were kept at 100 °C and 110 °C, respectively. The substrate temperature was varied from 50 – 300 °C to determine the effect of temperature on the growth rate and the quality of the ALD oxides. The substrate temperature setpoint was calibrated according to table 3.2. The temperatures of the top plate, chamber, chamber ports, exhaust port, and foreline were tabulated in the table 3.3.

**Table 3.2 Calibration table for the setpoint of the substrate temperature**

| Setpoint (°C) | Substrate Temperature (°C) |
|---------------|----------------------------|
| 55            | 50                         |
| 107           | 100                        |
| 158           | 150                        |
| 210           | 200                        |
| 266           | 250                        |
| 328           | 300                        |

**Table 3.3 The temperature of the various parts of the ALD system during the deposition**

| ALD Part      | Substrate Temperature (°C) |     |       |
|---------------|----------------------------|-----|-------|
|               | 50                         | 100 | ≥ 150 |
| Top Plate     | 35                         | 87  | 120   |
| Chamber       | 45                         | 97  | 130   |
| Chamber Ports | 45                         | 97  | 130   |
| Exhaust Port  | 45                         | 97  | 130   |
| Foreline      | 55                         | 107 | 140   |

The T(P)-Mm-TTT format is used to name the samples in this thesis. T or P specifies if the sample is deposited using TALD or PEALD process. Mm is the metal in the oxide (Zn:ZnO, Zr:ZrO<sub>2</sub>, and Hf:HfO<sub>2</sub>), and TTT is the deposition temperature.

### 3.3 *In-Situ* Spectroscopic Ellipsometry

Spectroscopic ellipsometry (SE) is an optical technique that enables determination of the thickness and optical properties of thin films. SE measures the change in polarization of monochromatic polarized light reflected from the material under study and converts the data into two parameters: the amplitude ratio,  $\Psi$ , and the phase change,  $\Delta$ .

$$\rho = \frac{r_p}{r_s} = \tan\psi \cdot e^{i\Delta} \quad (3.1)$$

$r_p$  and  $r_s$  are the complex amplitude reflection coefficients of reflected light parallel (p) and perpendicular (s) to the plane of the incidents [66, 67]. The measured values were used to fit the thickness and optical properties of an optical model iteratively until the lowest mean square error (MSE) was obtained. Figure 3.3 shows schematically how SE works. *In-situ* SE (iSE) is a powerful tool for studying the growth of ALD films in real-time [68]

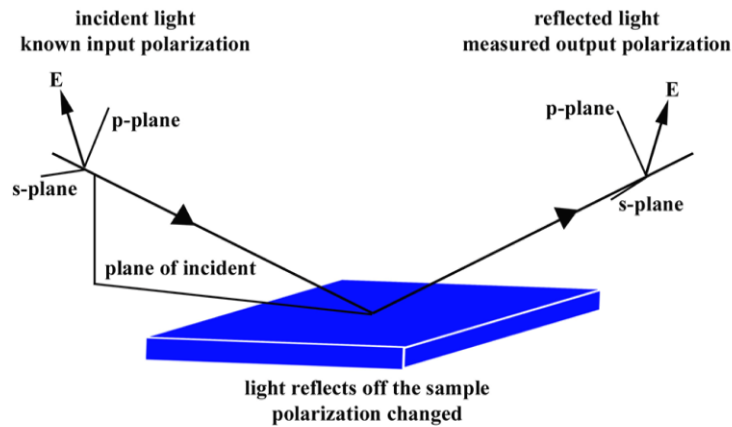


Figure 3.3 A Schematic view of SE.

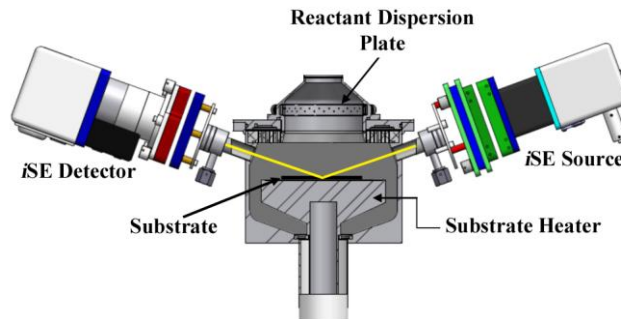


Figure 3.4 A Schematic view of the SE mounted on the ALD chamber. The plasma source on top of the chamber was not shown in this figure.

In this thesis, a J.A.Woollam M-2000DI spectroscopic ellipsometer was used to monitor the thickness and optical constants of the growing oxide *in-situ*. A schematic view of the SE mounted on the ALD chamber is shown in Figure 3.4. The ellipsometric  $\psi$  and  $\Delta$  were acquired at a fixed incident angle of  $70^\circ$  over the photon energy range of 0.735 - 6.464 eV. CompleteEASE software (v4.50 from J.A.Woollam Co. Inc.) [69] was used to analyze the ellipsometric data and determine the thickness of the growing films by applying an appropriate optical model [70]. The optical model consisted of three different layers: Si-Substrate/Si Native Oxide/ALD oxide. Si and the native oxide were modeled using wavelength-dispersed optical constant data available in the CompleteEASE software database. ZnO has a bandgap of approximately 3.3 eV and therefore is not transparent over the wavelength range of the ellipsometer. Both Tauc-Lorentz (TL) and Cody-Lorentz (CL) models have been used for optical modeling of oxides and semiconductors [71, 72]. However, CL model was found to describe the ellipsometry data better, with a lower mean square error (MSE) and therefore was used as an optical model of ZnO thin films. TL models were used for HfO<sub>2</sub> and ZrO<sub>2</sub>, as they have bandgaps of approximately 6.0 eV [73-75]. The optical constants of the ALD film were found by fitting the optical model to the measured data after 100 ALD cycles. To find the thickness of the growing oxide, it was assumed that the optical constants do not change during the ALD growth.

### **3.4 Atomic Force Microscopy (AFM)**

Atomic force microscopy (AFM) is a high-resolution imaging technique based on scanning the surface with an atomically sharp probe. The AFM uses a

microfabricated cantilever to scan the surface. A laser reflected off the cantilever monitors the deflection, or the oscillation amplitude of the cantilever due to the change in the atomic force between the tip and the surface. A feedback-controlled piezoscanner adjusts the detected changes in deflection or amplitude to a setpoint value by actuating the cantilever in Z-direction. The lateral resolution of AFM is limited by the sharpness of the tip, which is on the order of few nanometers. New probes offer a typical tip radius of curvature of less than 8 nm. However, the resolution in Z direction is restricted by the electronic or thermal vibrations and is on the order of an Angstrom [76].

In this study, A Veeco Dimension 3100 Atomic Force Microscope was used to study the roughness and to characterize the quality of the ALD films. The AFM instrument was located on a structurally isolated floor pad on an air table to minimize any vibration from the surrounding environment. All measurements were taken in tapping mode using NanoWorld Pointprobe® NCH probes with a force constant of 42 N/m and a resonance frequency of 320 kHz. Scans were made from a  $1.0 \times 1.0 \mu\text{m}^2$  area with a scan rate of 1 Hz and a resolution of 512 lines in both X and Y direction. All the AFM studies were performed on 20nm-thick films.

After obtaining the AFM images, they were subjected to 3<sup>rd</sup> order flattening using the NanoScope Analysis v1.40r1 software to remove any nonlinear background artifacts due to the piezoscanner. Three different roughness parameters were calculated:

$$R_a = \frac{1}{N} \sum |Z_j| \quad (3.2)$$

$$R_q = \sqrt{\frac{\sum Z_j^2}{N}} \quad (3.3)$$

$$R_{max} = R_p + R_v \quad (3.4)$$

where  $Z_j$  is the height of the profile at point  $j$ ,  $N$  is the number of the points,  $R_a$  is the roughness average,  $R_q$  is the root mean square (RMS) roughness,  $R_p$  is the maximum peak height,  $R_v$  is the maximum valley depth, and  $R_{max}$  is the maximum roughness depth.

### 3.5 X-Ray Photoelectron (XPS) Analyses

X-ray photoelectron spectroscopy (XPS) is a quantitative spectroscopic technique for surface chemical analysis that measures the elemental composition, chemical state, and electronic states of elements. XPS applies a focused monochromatic X-ray beam, usually Al-K $\alpha$ , to study the chemistry of surfaces. The material under study absorbs the photons and emits electrons (photoelectrons) by a process known as the photoelectric effect [77]. The XPS spectrum is then plotted as the count rate of photoelectrons detected versus the binding energy of the electrons,  $E_{binding}$ , according to Ernest Rutherford's equation:

$$E_{binding} = E_{photon} - (E_{kinetic} + \phi) \quad (3.5)$$

where  $E_{kinetic}$  is the kinetic energy of the emitted photoelectron,  $E_{photon}$  is the known photon energy, and  $\phi$  is the work function of the spectrometer. Each element creates a characteristic set of XPS peaks at specific binding energy values. The binding energy of an electron also depends on the oxidation state of the element, and its local chemical and physical environment. For example, an atom of higher positive oxidation state exhibits a higher BE due to extra columbic

attraction between the electron and the nuclei and an atom with a more negative oxidation state has a peak shifted to a lower BE positions. Detection limit of the XPS is in the range of 0.1-1.0 at. %.

In this thesis, X-ray photoelectron spectroscopy (XPS) measurements were performed in an ULTRA (Kratos Analytical) AXIS-165 spectrometer using monochromatic Al-K $\alpha$  radiation ( $h\nu = 1486.6$  eV) run at a power of 210 W. The XPS samples was 20 nm thick and sputter etched by 4 keV Ar $^+$  for 2 min before the analyses. Data was collected under ultrahigh vacuum ( $10^{-9}$  torr) from an area of 300 $\mu\text{m}\times$ 700 $\mu\text{m}$ . High-resolution spectra were collected with step energy of 0.1 eV. A charge neutralizer was used to compensate charging effects. The XPS data were analyzed using CasaXPS software. The binding energy scale was calibrated using the C1s peak at 284.8 eV, presented in all the samples. Background subtraction was done using a nonlinear Shirley-type background model.

### **3.6 X-Ray Diffraction (XRD) Analyses**

X-ray Diffraction (XRD) is a method used for determining the atomic and molecular structure of a crystal. The crystalline materials cause a beam of X-rays to diffract into many specific directions determined by Bragg's law [78]:

$$2d\sin\theta = n\lambda \quad (3.6)$$

where  $d$  is the spacing between diffracting planes,  $\theta$  is the incident angle,  $n$  is an integer, and  $\lambda$  is the wavelength of the beam. These specific directions,  $\theta$ , then are used to determine the interplanar distances,  $d$ , in the material under study.

Rigaku Ultima IV In-plane system was used with Cu-K $\alpha$  radiation (40 kV, 44 mA) with a thin film attachment in order to investigate crystallinity of ALD

samples. The scan speed was  $2.00\text{ }^{\circ}\text{ min}^{-1}$  with a  $0.05^{\circ}$  sampling width and the scan range was from  $20$  to  $90^{\circ}$ .

## Chapter 4

---

# Atomic Layer Deposition of Zinc Oxide

### 4.1 Introduction

Zinc oxide (ZnO) has become one of the most important electronic materials today as a low-cost alternative to gallium nitride (GaN) and indium tin oxide (ITO) [79, 80]. In ZnO, the empty  $4s$  orbital of  $\text{Zn}^{2+}$  and the filled  $2p$  orbital of  $\text{O}^{2-}$  form the conduction and valence bands, respectively [81]. This electronic structure and the ionic nature of ZnO bonds results in the unique properties of ZnO including a direct wide bandgap of 3.3 eV at 300 K and the excellent controllability of carrier types, concentration, and mobility. Due to these properties, ZnO has found many applications in optoelectronics including light emitting diodes (LEDs), photodiodes, transparent thin film transistors, and photovoltaic (PV) cells [1, 82, 83]. Various methods have been utilized to deposit ZnO thin films including sol-gel, pulsed-laser ablation, and sputtering [84]. Atomic layer deposition (ALD) is a deposition technique based on alternative exposures of the surface to the precursors separated by purging of an inert gas [53]. The self-limiting nature of ALD arises from this distinctive precursor delivery to the substrate. Due to this fact, ALD offers precise control over thickness, conformal films, and high uniformity of thin films. Furthermore, using highly reactive precursors enables ALD of oxides at very low temperatures [85, 86]. Due to these exceptional properties, ALD ZnO has attracted attention recently [87-93].

The first successful ALD of ZnO using diethylzinc (DEZ) and water was reported by Yamada et al. [94]. They found an ALD window in the range of 105-165 °C for the process. Ott and Chang [95] achieved a maximum growth rate of 1.9 Å/cycle at 130 °C using the same precursors. It was shown that good quality ZnO could be achieved by ALD at low temperatures by controlling the deposition temperature and dose/purge times without any post-treatment [85, 87, 96]. However, the electrical properties of ALD ZnO thin films were observed to be very dependent on the deposition temperature even in the ALD window temperature range [97]. O<sub>3</sub> [98], O<sub>2</sub> [88], and remote oxygen plasma [89, 91] were utilized instead of H<sub>2</sub>O as the oxidizing reagents in order to lower the growth temperature. However, this led to higher resistivity ZnO films due to the inclusion of Si impurities and oxygen interstitials into the films. Thomas and Cui [99] showed that the resistivity of the films could be controlled using plasma-enhanced thermal-ALD.

In spite of this research on the ALD of ZnO, there is a lack of a fundamental study on growth mechanism of ALD ZnO thin films. In this chapter, a systematic approach to ALD ZnO is presented for both thermal (TALD) and plasma-enhanced ALD (PEALD) at different deposition temperatures. The chemical analysis, crystallography, roughness, optical constants, and electrical properties of the PEALD and TALD films deposited at different temperatures are measured, compared, and discussed. At the end of the chapter a density functional theory (DFT) approach to the growth mechanism of ALD ZnO is presented. A good match between experimental and theoretical results was found.

## 4.2 Experimental Procedure and Theoretical Model

The details of ALD process and substrate preparation were discussed in Chapter 3. The saturation curves for DEZ, H<sub>2</sub>O, and O<sub>2</sub>-plasma were plotted at 100 °C, to find the optimum dose times. These optimal values were used for the deposition of ZnO at all other deposition temperatures. The optical model for the growing oxides were fitted at the end of cycle number 100 and fixed to fit the oxide thickness throughout the ALD process. XPS, XRD, AFM characterizations were done on the 20nm-thick ALD films. More details can be found in Chapter 3. 40-nm thick ALD ZnO oxide was deposited on pre-cleaned glass microscope slides (Fisher: 75×50 mm<sup>2</sup>) for electrical resistivity measurements. The four-point probe measurements were carried out with a Jandel® probe with a Keithley® 2400 source, with probe spacing of 1.575 mm. To avoid the need of applying any additional geometric correction factor, the measurements were performed in the center of the samples, at least 10 mm from the edges.

GAUSSIAN 09 [100] was used to perform molecular orbital calculations. The geometry of stationary points was located using the B3LYP gradient corrected density functional method [59-62] with 6-311G(d) polarized triple split valence basis set [101, 102]. This level of theory has shown reliable results in studying growth mechanisms of chemical vapor deposition (CVD) of ZnO [103-105]. We carried out the frequency calculations at the same level of theory to identify the nature of the stationary points (local minima and transition states) and to calculate the zero-point energy corrections and the thermal corrections at ALD temperature and pressure. All energies reported here are corrected by the zero-point energy

correction value. In order to test the validity of the calculations, we compared our results with available experimental data whenever possible.

## **4.3 Results and Discussion**

### **4.3.1 Optical Constants**

Variations of optical constants, refractive index ( $n$ ) and extinction coefficient ( $k$ ), vs. deposition temperature and energy of the incident photon for TALD and PEALD ZnO films are depicted in Figure 4.1(a-d). TALD ZnO grown at  $T < 100$  °C results in a poor quality oxide with a low refractive index, which reveals the low density of the zinc oxide. PEALD of ZnO leads to higher refractive index than TALD films grown at the same deposition temperature. However, both ALD methods deposit ZnO with the optical constants that are comparable to the bulk ZnO values [106] and films deposited by RF magnetron sputtering [107] at deposition temperatures above 100 °C. An increase in deposition temperature above 200 °C has no noticeable effect on the optical constants of the ALD ZnO.

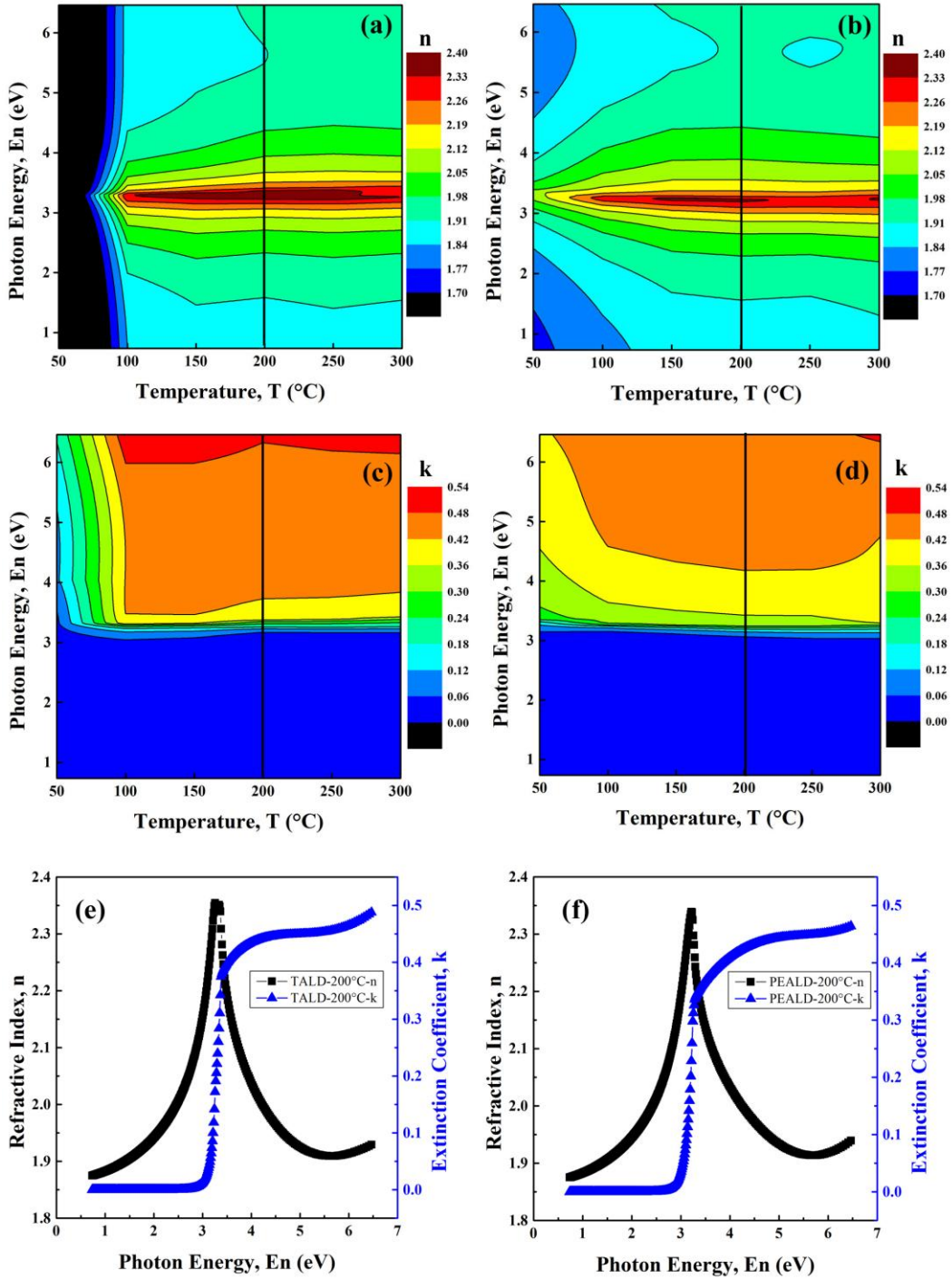


Figure 4.1 Refractive index (a,b) and extinction coefficient (c,d) of TALD (a,c) and PEALD (b,d) ZnO at the deposition temperature. For more clarity the refractive index and extinction coefficient of the samples deposited at 200 °C are shown in (e, f).

The optical bandgaps of the ALD oxides were determined by extrapolations of the near-band gap dielectric function, as shown in Figure 4.2, according to the Cody model [71] the imaginary part of the dielectric function,  $\varepsilon_2^{1/2} = E_n - E_g$ , where  $E_n$  is the photon energy and  $E_g$  is the optical bandgap of the oxide. The optical bandgap values at the deposition temperature are shown in Table 4.1. The optical bandgap of bulk ZnO at room temperature is reported in the range of 3.1 to 3.3 eV, considering the valence band-donor transition at 3.15 eV [108]. The optical bandgap values of ALD films are fairly close to this range.

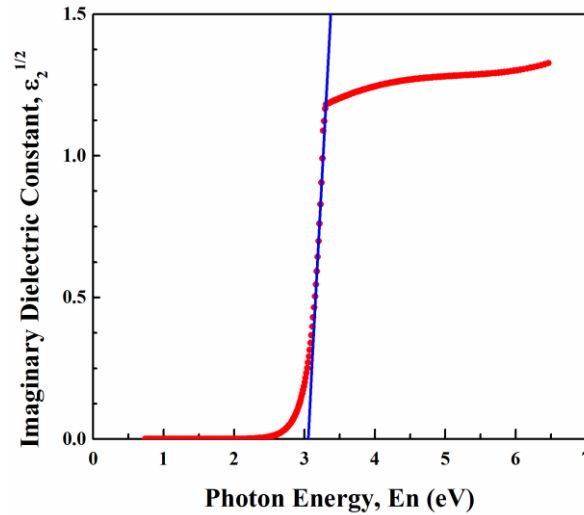


Figure 4.2 Illustration of the procedure of finding the optical bandgap of PEALD ZnO at 100 °C.

Table 4.1 Optical bandgap of ALD ZnO at various deposition temperatures in eV (the error in the calculated bandgap values are about 0.2 eV)

| Deposition Temperature | 50 °C | 100 °C | 150 °C | 200 °C | 250 °C | 300 °C |
|------------------------|-------|--------|--------|--------|--------|--------|
| TALD                   | 2.2   | 3.0    | 3.0    | 3.1    | 3.1    | 3.1    |
| PEALD                  | 3.1   | 3.1    | 3.1    | 3.0    | 3.0    | 2.9    |

The effect of temperature on the optical bandgap was found by measuring the optical bandgap of T-ZnO-200 sample at different temperatures. The results are

shown in Figure 4.3. It has been shown that the optical bandgap of ZnO depends linearly on temperature at  $T > 180$  K [109, 110],

$$E_g = E_0 - \beta T \quad (4.1)$$

where  $E_0$  is the absolute zero value of the optical bandgap and  $\beta = dE_g/dT$  is the rate of change of the bandgap with temperature. These values were determined from the slope and the intercept on the vertical axis, as shown in Figure 4.3. The relatively large error bars are the results of the method of the calculation of the optical bandgaps. The absolute zero value of the optical bandgap and the rate of change with temperature were found to be  $3.55 \pm 0.05$  eV and  $1.47 \pm 0.10$  meV  $K^{-1}$ , respectively. The  $E_0$  value closely matches the reported values in literature [109, 110]. However, the  $\beta$  value is slightly higher than the reported values ( $\sim 0.3$  meV  $K^{-1}$ ) for samples prepared using the sol-gel method. This difference may be due to the dissimilar microstructures that would arise due to the fundamentally different growth methods.

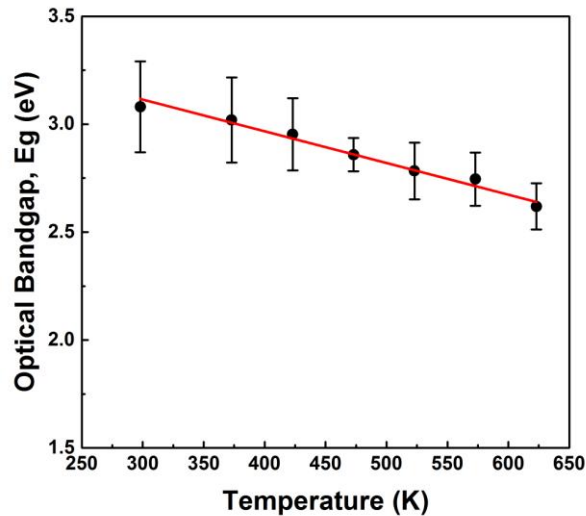


Figure 4.3 Effect of temperature on the optical bandgap of TALD ZnO deposited at 200 °C.

Two explanations have been given for the shift of the direct bandgap with temperature in the semiconductors [111]: (1) lattice thermal expansion which is related to the change of electron energies with the volume, and (2) direct renormalization of the band energies due to the temperature dependence of the electron–phonon interactions.

#### **4.3.2 Saturation curves and GPC**

The ALD saturation curves for TALD and PEALD of ZnO are shown in Figure 4.4. The minimum dose time for saturation of GPC is 20ms for DEZ, 0.1s for H<sub>2</sub>O and 2.0s for oxygen plasma.

The dependence of growth per cycle (GPC) of the ALD oxides on deposition temperature is shown in Figure 4.5. For both ALD techniques the GPC increased with deposition temperature and reached a maximum at 150 °C. The ALD window is in the range of 100-200 °C and is in agreement with the existing literature [89, 97]. More insightful explanation of the behavior of the GPC with deposition temperature is discussed later in section 4.4, where the reaction pathways of surface chemical reactions are discussed using density functional theory (DFT) calculations.

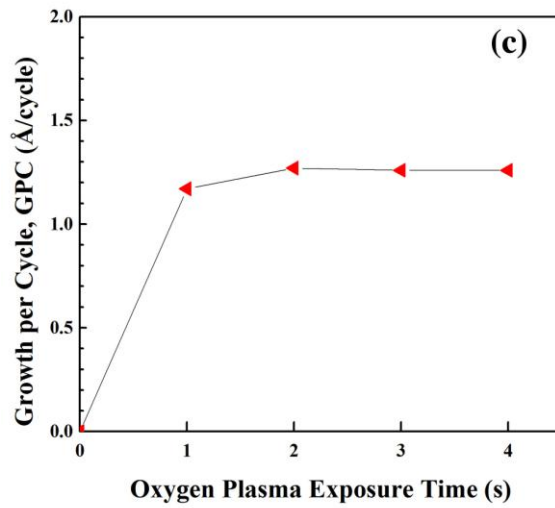
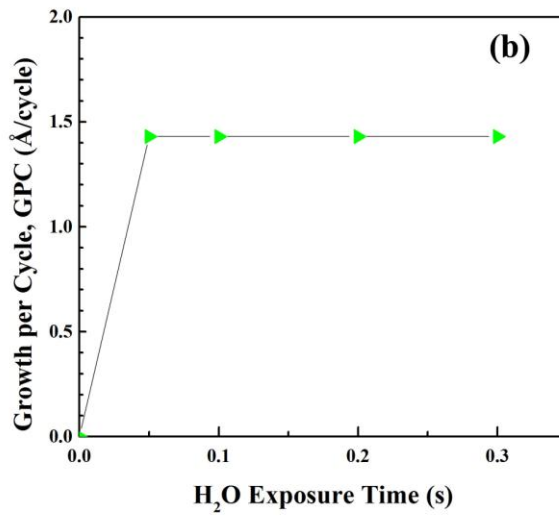
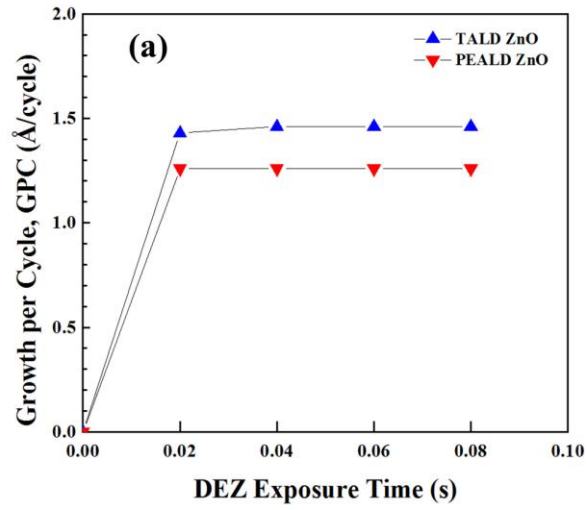
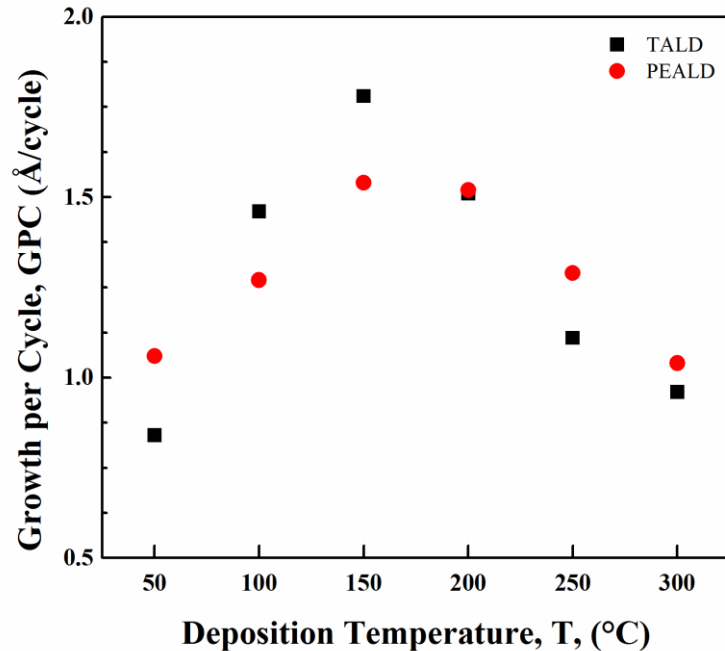


Figure 4.4 Variation of GPC vs. DEZ (a), H<sub>2</sub>O (b), and oxygen plasma (c) exposure times for ALD of ZnO at 100 °C.



**Figure 4.5** Variation of GPC with deposition temperature for TALD and PEALD of ZnO.

### 4.3.3 Chemical Composition

The high-resolution XPS profiles of Zn, O, and C elements in the ALD ZnO films are shown in Figure 4.6. Table 4.2 tabulates the chemical composition of the films. The films show no Si or Ar impurities. The peaks at 1021.1 eV and 1044.3 eV are attributed to Zn2p<sub>3/2</sub> and Zn2p<sub>1/2</sub> in ZnO, respectively [112, 113]. The ratio of the 2p<sub>1/2</sub>:2p<sub>3/2</sub> intensities is well matched with the 1:2 theoretical value determined from the multiplicity of the degenerate 2p<sub>1/2</sub> and 2p<sub>3/2</sub> electron configurations.

The O1s XPS profile (Figure 4.6b) shows the main peak at 529.9 eV of binding energy and a shoulder at 531.6 eV. The former comes from the O in Zn-O bond of ZnO crystal [114] while the latter is assigned to the O atoms in Zn-OH at the grain boundaries of the ZnO polycrystals [88, 115]. While the O1s peak at 529.9

eV intensifies with the ALD temperature, the peak at 531.6 eV vanishes due to reduction in the number of -OH reaction sites at high deposition temperatures.

The C1s profile shows two peaks at binding energies of 284.8 eV and 289.4 eV. The main source of the peak at higher binding energy is unknown and more studies are needed to find the source, however it might be attributed to the  $\text{ZnO}(\text{CH}_3\text{CO}_2)_2 \cdot \text{H}_2\text{O}$  hydrates [112]. The concentration of this C is very low (<1at.%) and decreases with deposition temperature. The  $\text{H}_2\text{O}$  in the plasma process arises from the combustion-like reaction of the ethyl groups in DEZ and oxygen in the plasma [116-118]. The peak at the lower binding energy increases with higher ALD temperatures. This peak can be assigned to the absorbed hydrocarbon fragments formed by dissociation of DEZ at high temperatures [119]. It seems that oxygen plasma increases the dissociation rate of DEZ molecules and the formation rate of hydrocarbons. All the ALD ZnO films show Zn deficiency. Increasing the deposition temperature results in lower O/Zn ratio.

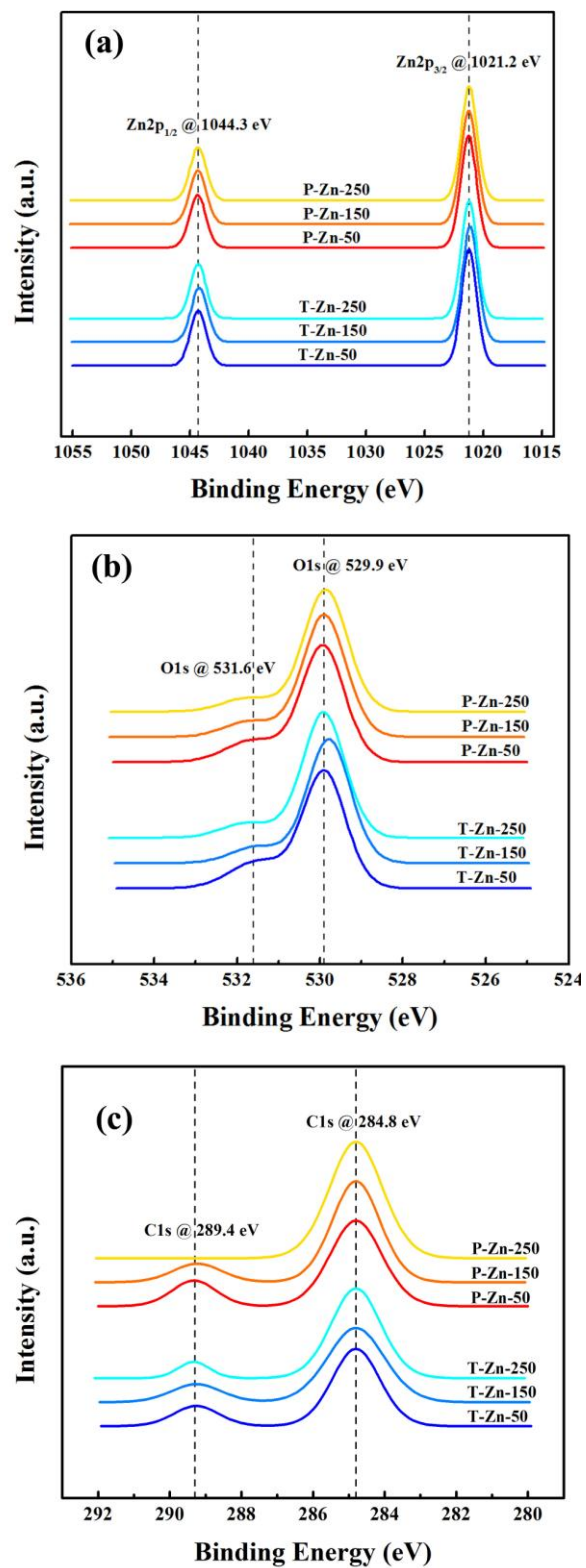


Figure 4.6 High Resolution XPS graphs of Zn2p (a), O1s (b), and C1s (c), for ALD ZnO with different deposition conditions.

**Table 4.2 Chemical compositions of ZnO films (at. %) deposited at various temperatures using thermal and plasma-enhanced ALD**

| <b>Sample Name</b> | <b>O1s<br/>@ 529.9</b> | <b>O1s<br/>@ 531.6</b> | <b>Zn2p<sub>3/2</sub><br/>@ 1021.2</b> | <b>Zn2p<sub>1/2</sub><br/>@ 1044.3</b> | <b>Zn (I<sub>3/2</sub>/I<sub>1/2</sub>)</b> | <b>O/Zn<br/>ratio</b> | <b>C1s<br/>@ 284.8</b> | <b>C1s<br/>@ 289.4</b> | <b>C1s<br/>total</b> |
|--------------------|------------------------|------------------------|--|--|---|-----------------------|------------------------|------------------------|----------------------|
| T-Zn-50            | 40.7                   | 12.0                   | 30.1                                   | 14.6                                   | 2.0   | 1.18                  | 2.1                    | 0.5                    | 2.6                  |
| T-Zn-150           | 44.2                   | 6.9                    | 31.0                                   | 15.0                                   | 2.0   | 1.11                  | 2.4                    | 0.5                    | 2.9                  |
| T-Zn-250           | 44.5                   | 6.6                    | 31.4                                   | 14.6                                   | 2.0   | 1.11                  | 2.6                    | 0.3                    | 2.9                  |
| P-Zn-50            | 41.9                   | 9.8                    | 30.5                                   | 14.7                                   | 2.0   | 1.14                  | 2.5                    | 0.6                    | 3.1                  |
| P-Zn-150           | 44.3                   | 6.7                    | 30.8                                   | 14.8                                   | 2.0   | 1.12                  | 2.8                    | 0.5                    | 3.3                  |
| P-Zn-250           | 44.4                   | 6.0                    | 31.2                                   | 14.7                                   | 2.0   | 1.10                  | 3.6                    | -                      | 3.6                  |

### 4.3.4 Roughness

The AFM images of the ALD ZnO deposited under different conditions are shown in Figure 4.6. Table 4.3 and Figure 4.7 summarize the RMS roughness for the samples. It can be seen that the roughness of the samples decreases with deposition temperature for both TALD and PEALD ZnO. This result is consistent with the previous result obtained by Elam et al. for TALD ZnO [120, 121]. The PEALD ZnO samples have lower roughness than the TALD ZnO films at the same deposition temperature.

**Table 4.3 RMS Roughness parameters of the TALD and PEALD ZnO deposited at various temperatures (the Si substrate roughness was  $0.11 \pm 0.02$  nm)**

| Deposition Temperature<br>(°C) | RMS Roughness (nm) |                 |
|--------------------------------|--------------------|-----------------|
|                                | TALD               | PEALD           |
| 50                             | $2.98 \pm 0.22$    | $2.79 \pm 0.17$ |
| 150                            | $2.57 \pm 0.17$    | $2.09 \pm 0.15$ |
| 250                            | $2.44 \pm 0.13$    | $1.58 \pm 0.33$ |

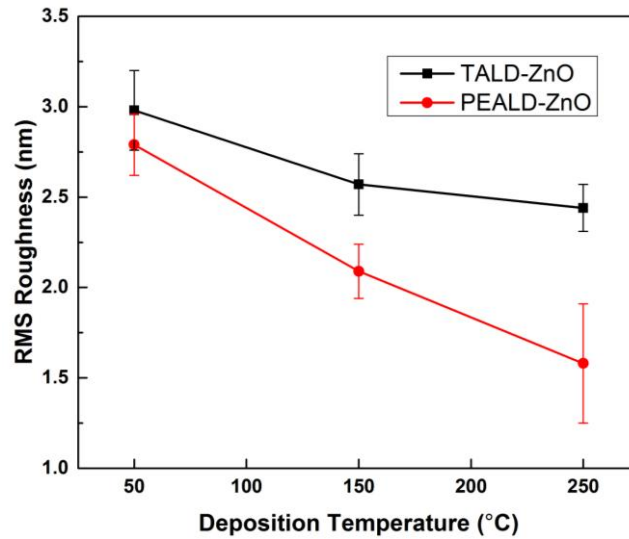


**Figure 4.7 Average RMS roughness of the ALD ZnO thin films vs. the deposition temperature.**

It seems that the crystallinity and crystal size have the most effect on the roughness of the samples. It is believed that amorphous films should follow their substrate surface features and as result must have very smooth surface. Consequently, the peaks in the AFM images can be attributed to the crystal phase in the samples [122]. Elam et al. [120] suggested that the rougher surface is the result of the larger crystals due to the lower nucleation rate or smaller surface diffusion rate of the atoms at low deposition temperatures. However, by looking at the AFM surface plots in Figure 4.8, it can be observed that at lower temperatures the number of the crystals are higher, although their size are smaller. The average grain size calculated from AFM images is summarized in table 4.4 and Figure 4.9. As expected, the grain size increases with deposition temperature, due to higher surface diffusion rate. The PEALD process shows a faster grain growth due to the energy introduced into the films from the plasma source, which increases the surface diffusion rate and results in a smoother surface.

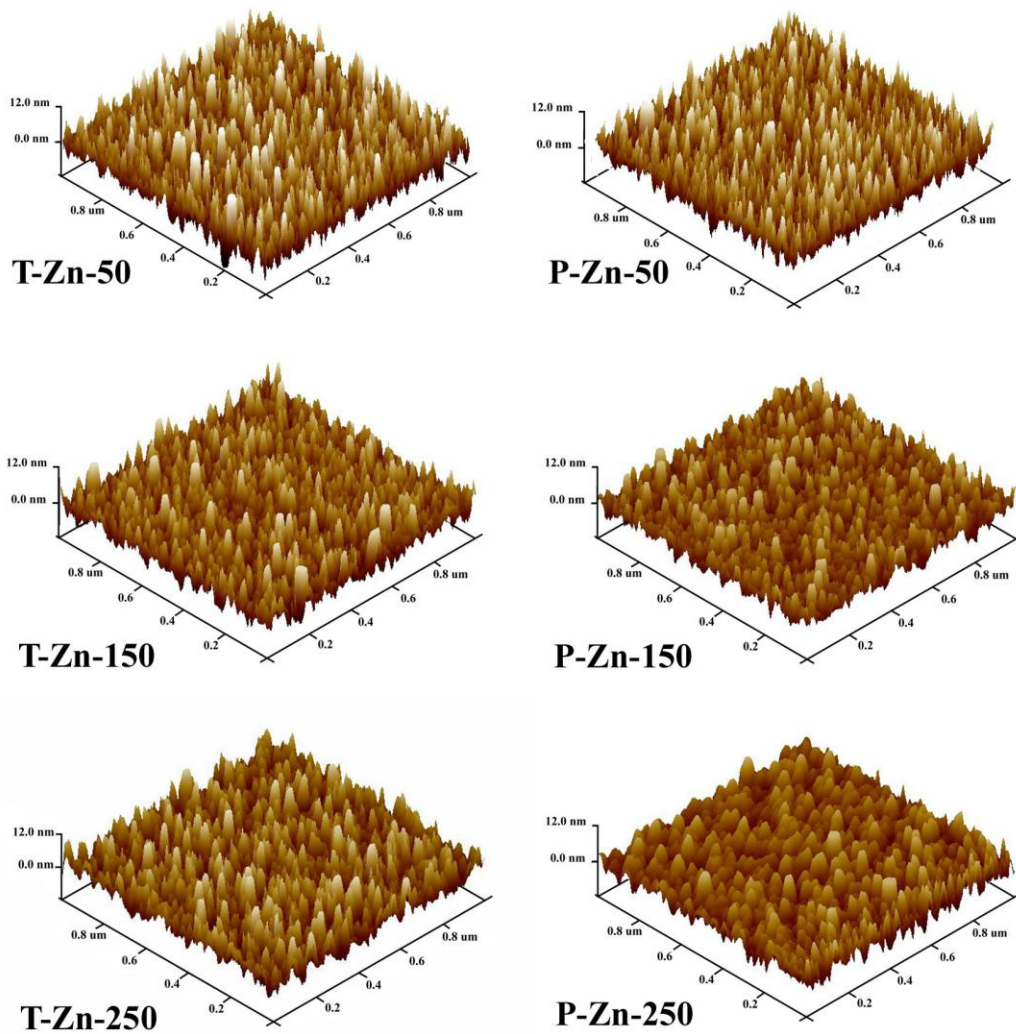


**Figure 4.8** AFM surface plots of the ALD ZnO deposited at different temperatures using thermal and plasma-enhanced approaches.

**Table 4.4** Average grain size of ALD ZnO films (nm)

| Temperature (°C) | TALD         | PEALD        |
|------------------|--------------|--------------|
| 50               | 14.06 ± 0.47 | 14.03 ± 0.58 |
| 150              | 17.26 ± 0.52 | 19.84 ± 0.67 |
| 250              | 22.97 ± 0.54 | 31.33 ± 0.85 |

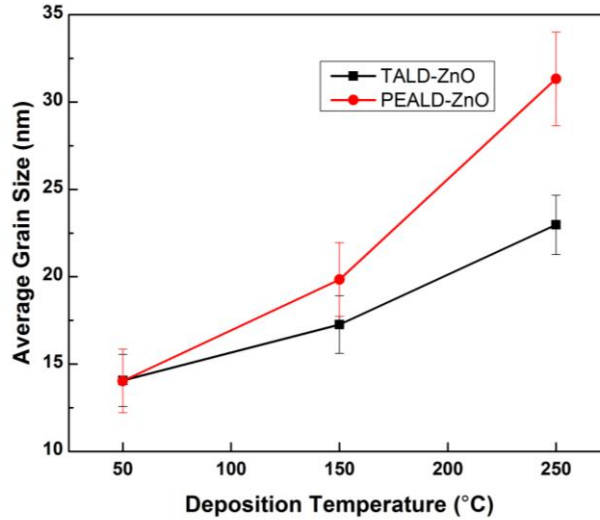


**Figure 4.9 Average grain size of ALD ZnO films vs. the deposition temperature.**

#### **4.3.5 Crystallinity**

The XRD profiles of the ZnO thin films are shown in Figure 4.10. All of the zinc oxides show the hexagonal crystalline microstructure, regardless of the deposition temperature or ALD process, which is consistent with the existing literature [122]. The intensities of the peaks increase with deposition temperature. PEALD samples show higher crystallinity than that of TALD at the same deposition temperature. The ratio of the intensities of the (002) to (100) peaks increases with deposition temperature as well. This shows that the preferential growth of ZnO alters from c-axis perpendicular to the surface to c-axis parallel to the growth direction at elevated temperatures.

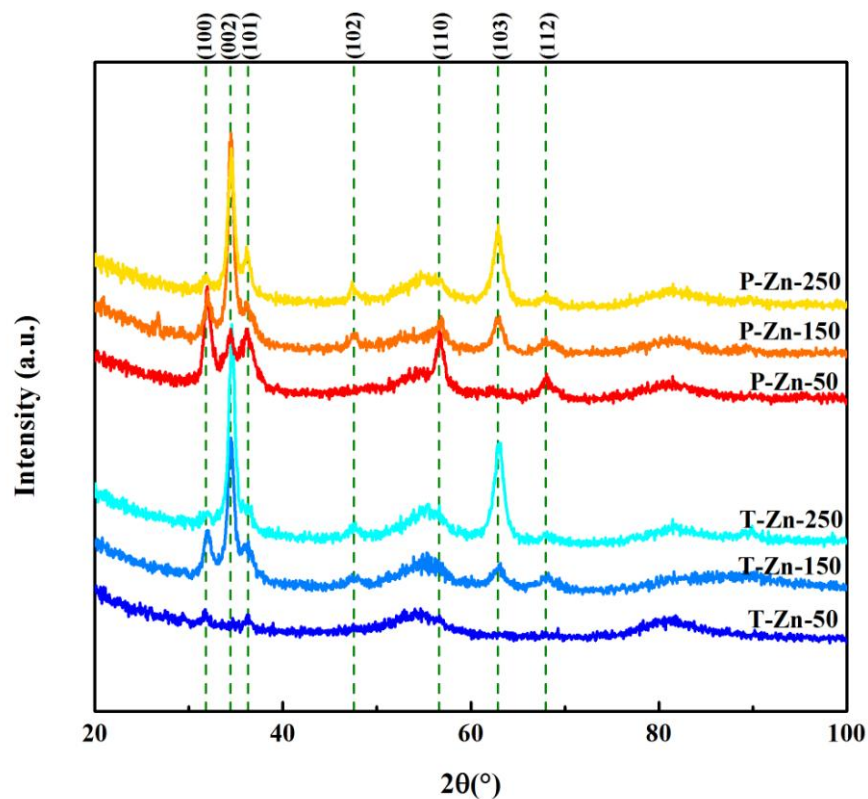


**Figure 4.10 XRD profiles of the TALD and PEALD ZnO samples deposited at various temperatures.**

Makino et al. suggested that the amount of  $-OH$  groups affects the surface mobility and as a consequence the crystallography and texture of the ALD ZnO films [123]. This is consistent with our XPS results, which show lower amount of  $Zn(OH)$  for the films deposited at higher temperatures. Another source of preferential growth of ZnO during the ALD could be blocking of the (002) face by byproducts of dissociation of DEZ (hydrocarbons) at lower temperatures [124]. These products desorb from the surface at elevated deposition temperature and permit growth on the (002) surface [125]. However, in this study, the XPS results show that the amount of hydrocarbons in the films increases with the temperature.

It seems that –OH groups has more influence on the preferential growth of the ZnO than physisorbed hydrocarbon species.

It must be mentioned that chemistry of the substrate and its crystallographic orientation, the chemistry of the precursors, ALD film thickness, and dose and purge time durations can affect the crystallinity and roughness of the ZnO films [125]. All of these parameters were kept constant during this thesis.

Based on the above observations, a model for crystal growth of the ALD ZnO samples is proposed. The ZnO grains nucleate at random crystallographic directions at low deposition temperatures. The surface migration is limited by the high concentration of –OH groups and low deposition temperature. As a result a columnar growth of ZnO crystals is observed, which leads to a rough ZnO surface. By increasing the deposition temperature, the –OH group concentration decreases and the surface diffusion of atoms become more convenient, and the grains start to grow laterally. The [0001] direction is the preferential orientation because of the surface energy considerations [126]. Based on this model, elongating the purge time shifts the preferred orientation towards [0001] direction due to extra time available for the adsorbed species to desorb from the surface and –OH groups to recombine and desorb from the surface in form of H<sub>2</sub>O. This model agrees well with the experimental results from Malm et al. [127], who showed high (002) peak intensities at low temperature by using relatively long purge times. Using oxygen plasma, or molecular oxygen, also changes the crystals orientation towards [0001] due to lower –OH concentration on the surface and at the grain boundaries. This matches with Park and Lee's [128] observations and

our experimental data (Figure 4.10). Figure 4.11 summarizes this proposed model for the nucleation and growth of crystalline ALD ZnO with respect to deposition temperature, purge time, and the ALD process type.

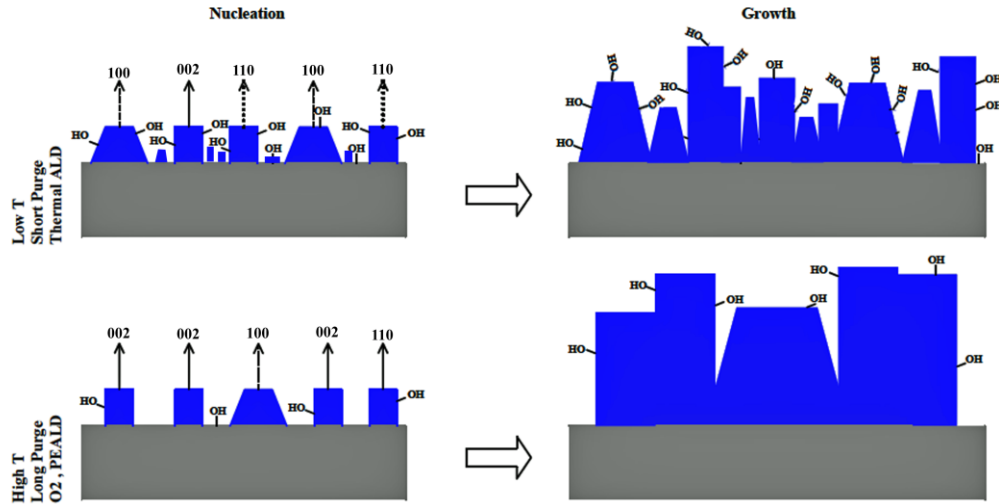


**Figure 4.11** Schematic views of crystallites nucleation and growth of ALD ZnO at different deposition conditions. The gray indicates the substrate and the blue represents the ZnO crystallites. At low deposition temperature, the lateral growth is limited by the slow surface diffusion of atoms due to presence of  $-OH$  groups.

#### 4.3.6 Electrical Resistivity

The resistivity of the ZnO thin films, in the deposition temperature range of 100-150 °C, is summarized in Figure 4.12. A sharp decrease in resistivity is observed as the deposition temperature increases. Hall measurements revealed that the films were n-type, however, the exact physical origin of the n-type carrier in ZnO is unknown. Oxygen vacancies and zinc interstitials are mentioned as plausible origin of the carriers [97]. However, first-principle calculations showed that the main source of n-type carriers is hydrogen impurities [129]. Moreover,

the zinc vacancies,  $V_{Zn}^{-2}$ , act as the compensating sites for n-carriers in n-ZnO [130]. This explanation agrees with our XPS results, which showed that the Zn deficiency of the samples decreases with increasing deposition temperature. On the other hand, although the hydrogen impurities cannot be detected by XPS, our XPS results showed that the amount of hydrocarbons increased with the deposition temperature. These results might indicate that the amount of hydrogen in samples deposited at higher deposition temperatures is larger and as a consequence they show much lower resistivity.

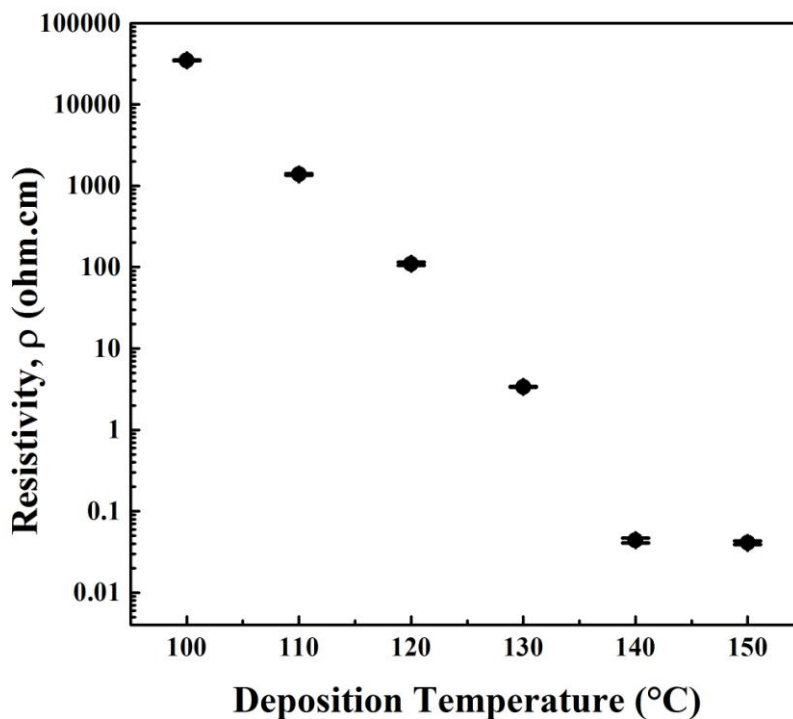


Figure 4.12 Variation of electrical resistivity of TALD ZnO with the deposition temperature.

## 4.4 Growth Mechanism of TALD ZnO: DFT Approach<sup>†</sup>

The variation of growth per cycle (GPC) of ZnO with substrate temperature is shown in Table 4.5. The GPC increases with substrate temperature and reaches a maximum of 1.80Å/cycle at 140°C, which agrees well with published data on ALD of ZnO using the same precursors [88, 89].

**Table 4.5 Variation of GPC with the substrate temperature for the ALD of ZnO**

| Temperature (°C) | GPC* (Å/cycle) |
|------------------|----------------|
| 75               | 1.16           |
| 100              | 1.46           |
| 110              | 1.56           |
| 120              | 1.72           |
| 130              | 1.74           |
| 140              | 1.80           |
| 150              | 1.78           |
| 160              | 1.70           |
| 175              | 1.60           |
| 200              | 1.60           |
| 215              | 1.43           |
| 230              | 1.37           |
| 250              | 1.11           |
| 300              | 0.96           |

\*The errors in the reported GPCs are less than 0.2%

Different mechanisms have been proposed to explain this behavior [53, 131]. Reaction rates and mass transport is slow at lower temperatures and results in incomplete reactions of precursors with surface reaction sites, Zn-OH\*. Considering the thermally activated nature of the half-reactions, increasing the substrate temperature should result in higher reaction rates and higher GPC.

<sup>†</sup> A version of this section has been published. A. Afshar and K.C. Cadien, Appl. Phys. Lett. 103 (25), 251906.

However, increasing desorption rate of surface species and unavailability of surface reaction sites at high temperatures causes GPC to drop.

In this section, we investigate these mechanisms employing a density functional theory (DFT) approach. Representing oxide surface sites using clusters has shown good outcome in quantum chemical studies of different oxide system such as alumina [132], zirconia [133], and hafnia [134]. We used structure *I*, depicted in Figure 4.13, to represent the Zn-OH\* surface reaction sites. This structure is a global minimum among all the possible structures from three Zn(OH)<sub>2</sub> monomers [103] and gives a close value of Zn-O bond length, 1.97Å, compared to 1.99Å of ZnO wurtzite structure with a=3.250Å and c=5.270Å lattice parameters [135]. The Zn-C bond length in the DEZ molecule, *2*, is 1.95 Å, C-Zn-C bond angle is 179.8°, and the Zn-C-C angle is 114.4°. These results agree well with gas electron diffraction (GED) investigations [136].

The first half-reaction for ZnO ALD is written as follows [137]:



where the \* represents the species on the surface and the (g) refers to the gas phase. As shown in Figure 4.13, the ALD reaction starts with the adsorption of DEZ molecules on the ZnO surface. In the adsorbed state, *AS-3*, oxygen in the hydroxyl group on the surface is pointing toward the zinc in DEZ at a distance of 2.12 Å. The C-Zn-C angle in DEZ decreases to 157.8° and ethyl groups move away from the hydroxyl group on the ZnO surface. The optimized geometry suggests that the *AS-3* complex forms through the interaction between the hydroxyl group oxygen lone-pairs and divalent zinc empty orbitals in DEZ. This

structure lies 19.3 kcal/mol below the reactants on the PES (Figure 4.14). The relatively large adsorption energy and strong interaction between DEZ and Zn-OH\* site imply the chemisorbed nature of the adsorption.

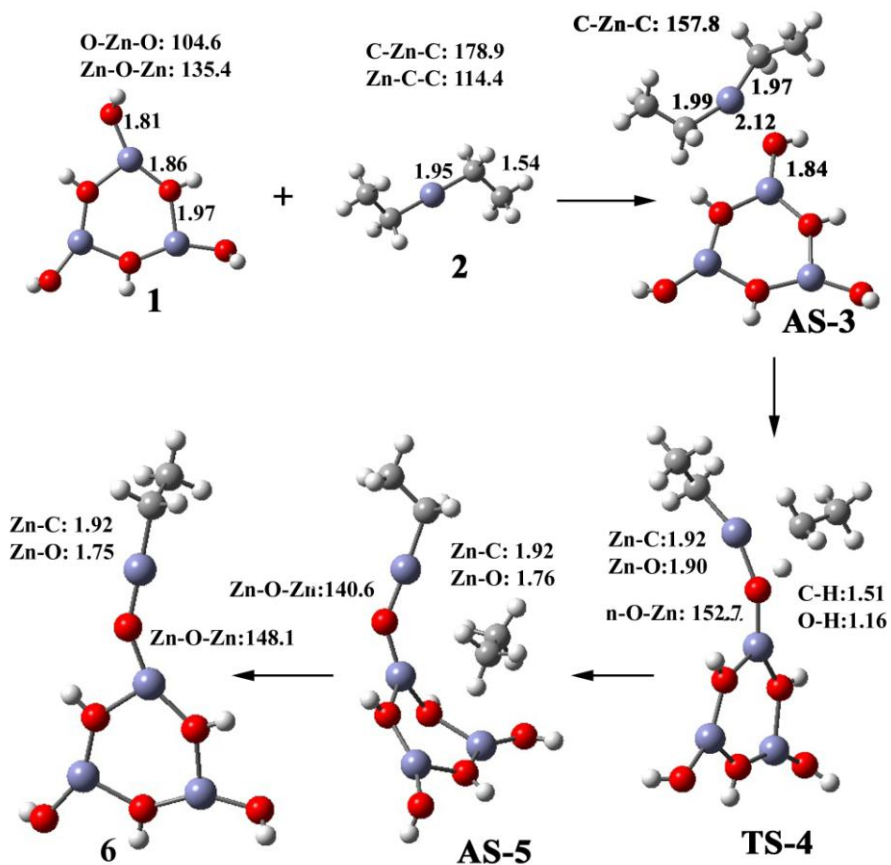


Figure 4.13 Reaction pathway of DEZ half-reaction. The white spheres represent H, red: O, black: C, and blue: Zn atoms. The bond lengths and angles are reported in Å and degrees.

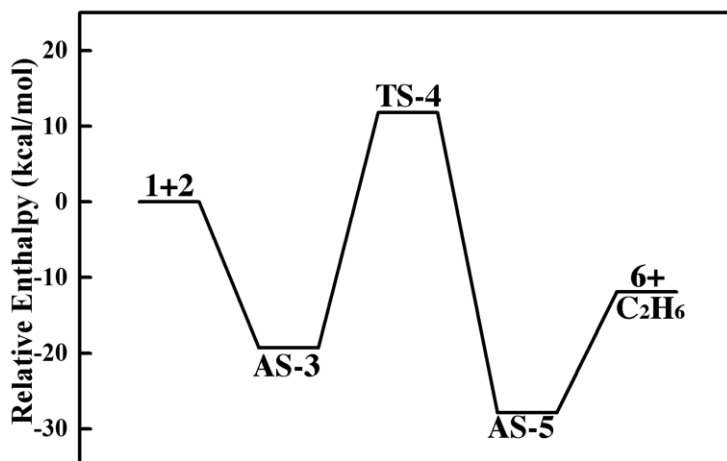


Figure 4.14 Potential energy surface for the DEZ half-reaction. The calculations were carried out at the B3LYP/6-311G(d) level. The enthalpy values are reported at 0 K. For clarity, the ZnO structure in the reactions is shown with a smaller cluster.

The ALD reaction proceeds by formation of a four-center transition state, *TS-4*, between O-H-Zn-C atoms. The transition vector is dominated by the movement of the H atom from a hydroxyl group to an ethyl ligand to form ethane. In *TS-4*, one of the Zn-C bonds in DEZ is broken and the Zn-C distance increases from 1.95Å to 2.38Å. The Zn-O bond forms between Zn in DEZ and O in the hydroxyl site on the ZnO surface and the O-H distance increases from 0.95Å in the chemisorbed state to 1.16Å in the transition state. Concurrently, the C-H distance decreases to 1.51Å from the 3.14Å in AS-3. *TS-4* lies 11.8 kcal/mol above the reactants and 31.1 kcal/mol above the chemisorbed state on the PES, which shows the reaction must gain supplementary energy to proceed.

In the post transition state structure, *AS-5*, C<sub>2</sub>H<sub>6</sub> is adsorbed on the ZnO surface. *AS-5* lies 11.9 kcal/mol lower than the desorbed state, **6** + C<sub>2</sub>H<sub>6</sub>, on the PES and the distance of the ethane molecule is 3.43Å from the oxygen in ZnO. This implies that the interaction of C<sub>2</sub>H<sub>6</sub> with surface is not strong and the

adsorption is more physisorbed in nature than chemisorbed. *AS-5* lies 39.7 kcal/mol lower than transition state, *TS-4*, and 8.6 kcal/mol lower than DEZ chemisorbed state, *AS-3*, on the corresponding PES. This shows that the DEZ half reaction is exothermic. The Gibbs free energy change of the reaction at the ALD pressure and temperatures are negative that indicates the reaction is thermodynamically favorable. The newly formed Zn-O bond length is 1.75Å. To verify the DFT calculations, we compared the vibrational frequency results to the available experimental values. Our unscaled frequency calculations show 3076, 3059, 3020, and 3010 cm<sup>-1</sup> vibrational frequencies for C-H stretching in structure, 6, that are within 5% of those obtained by Ferguson et al. [137] from in situ transmission FTIR vibrational spectroscopy.

The H<sub>2</sub>O half-reaction of ZnO ALD is shown in the following reaction [137]:

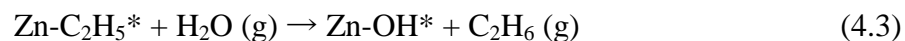
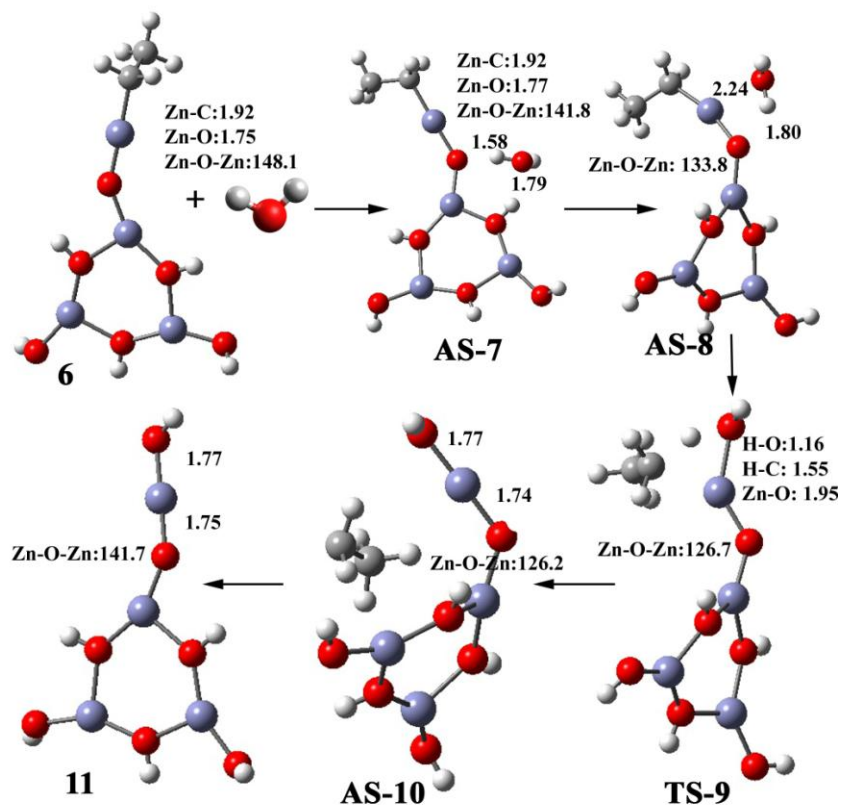


Figure 4.15 and 4.16 show the reaction pathways and the corresponding PES, respectively. The second half-reaction begins with adsorption of water on the surface and the formation of a complex, *AS-7*, which lies 24.1 kcal/mol lower than reactants on the PES. The complex optimized geometry and the high energy of adsorption suggest the formation of hydrogen bonds in this complex. Intrinsic reaction coordinate (IRC) calculations of the transition structure, *TS-9*, show that there should be another local minimum between *AS-7* and *TS-9*. In this structure, *AS-8*, the oxygen in H<sub>2</sub>O points toward the Zn atom in Zn-C<sub>2</sub>H<sub>5</sub>\*. This intermediate structure is formed by the interaction between the oxygen electron lone-pairs in H<sub>2</sub>O and empty orbitals of divalent zinc on the surface. A similar

structure has been observed for the initial growth mechanisms of ALD ZnO on hydroxylated silicon and chemical vapor deposition of ZnO using the same precursors [103, 105].



**Figure 4.15** Reaction pathway of H<sub>2</sub>O half-reaction. The white spheres represent H, red: O, black: C, and blue: Zn atoms. The bond lengths and angles are reported in Å and degrees.

The geometry optimization and frequency calculations with the 6-311G(d) basis set locate this intermediate structure, however the maximum displacement and rms of the displacement did not meet the convergence criteria, which is probably due to a relatively flat PES at this point. The *AS-8* lies 5.8 kcal/mol above the *AS-7* on the PES. Repeating the geometry optimization using the 6-31G(d) basis set confirmed that the *AS-8* structure is a local minimum on the PES. The

corresponding structure of the *AS-8* intermediate complex and the corresponding PES calculated using 6-31G(d) basis set is shown in Figure 4.17.

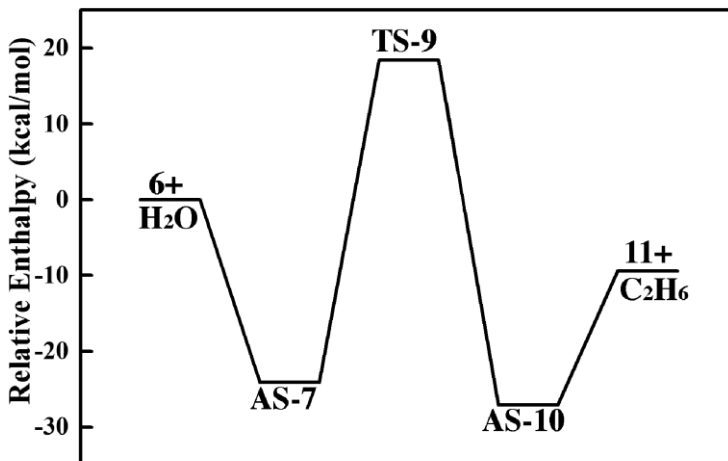


Figure 4.16 PES of  $\text{H}_2\text{O}$  half-reaction. All the calculations were carried out at the B3LYP/6-311G(d) level. The enthalpy values are reported at 0 K.

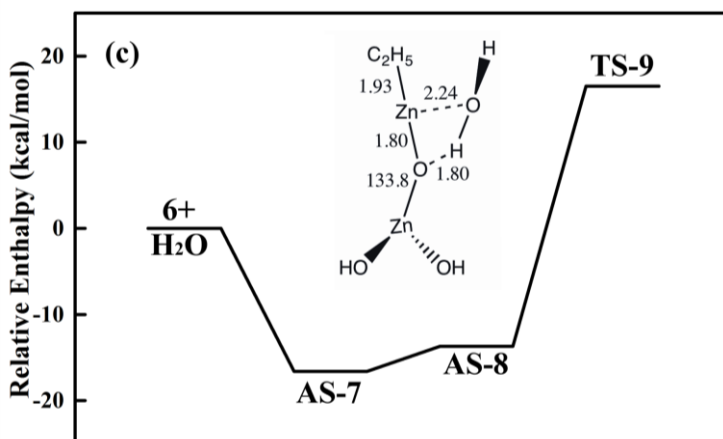


Figure 4.17 PES of  $\text{H}_2\text{O}$  half-reaction and the structure of *AS-8*, calculated at the B3LYP/6-31G(d) level. The enthalpy values are reported at zero Kelvin.

The reaction proceeds by transferring of one of the hydrogen atoms of  $\text{H}_2\text{O}$  to  $\text{C}_2\text{H}_5$ . The transition structure forms a four-center structure of Zn-O-H-C atoms. The motion of the H atom from water to the ethyl ligand dominates the transition vector. The H-O bond in  $\text{H}_2\text{O}$  stretches from  $0.95\text{\AA}$  to  $1.16\text{\AA}$  and the Zn- $\text{C}_2\text{H}_5$

bond breaks completely. The Zn-C distance increases to 2.24Å in the transition structure. The H-C<sub>2</sub>H<sub>5</sub> bond forms and its length is 1.55Å in *TS-9*. The transition structure, *TS-9*, lies 18.4 kcal/mol above the reactants on the PES. This means that the second half-reaction requires an additional energy to proceed.

The post-transition complex, *AS-10* lies 45.2 kcal/mol below the *TS-9* on the PES. The C<sub>2</sub>H<sub>6</sub> locates 3.68Å above the ZnO surface, with one of its C-H bonds pointing towards oxygen in ZnO. The desorbed state of C<sub>2</sub>H<sub>6</sub> from the ZnO surface, *II*, is located 16.7 kcal/mol higher on the PES than the post-reaction complex, *AS-10*. The products of the second ALD half-reaction lie 9.4 kcal/mol lower than the reactants on the corresponding PES, which indicates that the second half-reaction is exothermic. The Gibbs free energy of the reaction is negative at all the ALD temperatures, which means the reaction is thermodynamically favorable. The unscaled 3848 cm<sup>-1</sup> stretching mode for the OH bond on ZnO surface is within 5% of in situ FTIR studies by Ferguson et al. [137].

We also used a smaller, Zn(OH<sub>2</sub>), and a larger cluster, (Zn<sub>9</sub>O<sub>9</sub>H<sub>6</sub>-(OH)<sub>6</sub>), composed of three layers of structure *I*, to study the effect of near neighbor atoms on the surface reactions (Figure 4.18). These clusters were used to calculate the overall half-reaction thermodynamics and the geometry of the reactants and by-products (Table 4.6). The comparison between the half-reaction enthalpies, Gibbs free energies, and the geometries of the surface by-products for different clusters showed that the reactions are fairly insensitive to the cluster size and structure *I* is a good model for the reaction site.

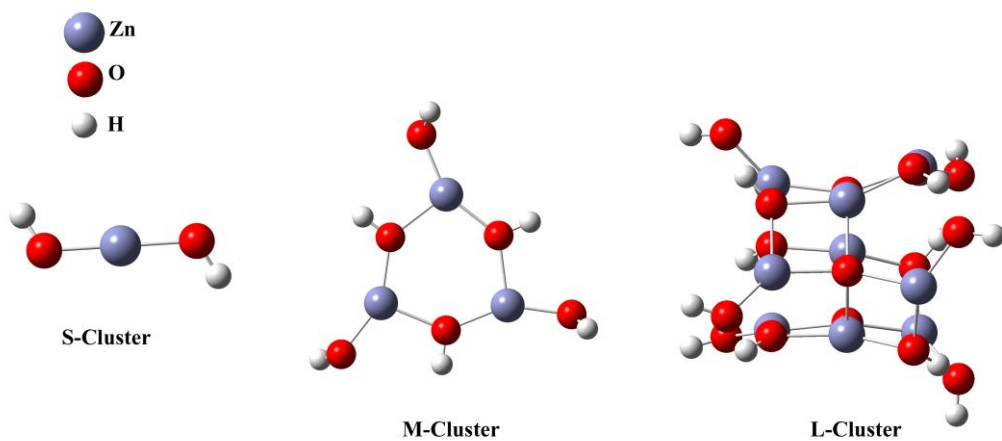


**Figure 4.18** The structure of the ZnO cluster models, which were used to study the effect of near neighbor atoms on the ZnO ALD half-reactions.

**Table 4.6 Effect of cluster size on the half-reactions energies and the geometry of structures 6 and 11**

|                 | S-Cluster  | M-Cluster | L-Cluster | Average | Standard Deviation |      |
|-----------------|--|-----------|-----------|---------|--------------------|------|
| <b>Energy</b>   | 1 <sup>st</sup> half-reaction enthalpy at 0 K (kcal/mol)                   | -13.3     | -11.9     | -16.0   | -13.7              | 2.1  |
|                 | 2 <sup>nd</sup> half-reaction enthalpy at 0 K (kcal/mol)                   | -8.7      | -9.4      | -8.0    | -8.7               | 0.7  |
|                 | 1 <sup>st</sup> half-reaction Gibbs free energy at 298 K, 1 atm (kcal/mol) | -13.0     | -11.1     | -14.5   | -12.9              | 1.7  |
|                 | 2 <sup>nd</sup> half-reaction Gibbs free energy at 298 K, 1 atm (kcal/mol) | -8.4      | -9.6      | -8.5    | -8.8               | 0.7  |
|                 | Zn-C bond length in structure 6 (Å)  | 1.75      | 1.75      | 1.77    | 1.76               | 0.01 |
|                 | Zn-O bond length in structure 6 (Å)  | 1.92      | 1.92      | 1.92    | 1.92               | 0.00 |
| <b>Geometry</b> | Zn-O bond length in structure 11 (Å)                                       | 1.77      | 1.77      | 1.77    | 1.77               | 0.00 |
|                 | Zn-O-Zn angle in structure 6 (°)   | 144.6     | 148.1     | 143.1   | 145.3              | 2.6  |
|                 | O-Zn-C angle in structure 6 (°)  | 178.2     | 178.7     | 177.7   | 178.2              | 0.5  |
|                 | Zn-O-Zn angle in structure 11 (°)  | 141.7     | 141.7     | 142.1   | 141.8              | 0.2  |

It can be deduced from the previous discussion that both ALD half-reactions involve formation of intermediate complexes. These complexes form between DEZ and Zn-OH\* in the 1st half-reaction, *AS-3*, and between H<sub>2</sub>O and Zn-C<sub>2</sub>H<sub>5</sub>\* in 2<sup>nd</sup> half-reaction, *AS-8*. The variations of the Gibbs free energy of formation of these complexes with temperature are shown in Figure 4.19 along with GPC of ALD ZnO. At temperatures higher than 120°C the desorbed state of DEZ is more stable than its chemisorbed state. This occurs for the H<sub>2</sub>O half-reaction at temperatures above 200°C. In other words, the formation of the complexes becomes more thermodynamically unfavorable with increasing ALD temperature. At high temperatures, the entropy-temperature product becomes much larger than the enthalpy and dominates Gibbs free energy. In chemisorbed states, the motions of adsorbates are limited compared to motions in the gaseous state. Consequently, the desorbed states of precursors have higher entropy and become more stable than the adsorbed states with increasing temperature. The stability of the complexes directly influences the growth rate of ALD ZnO. This is shown in Figure 4.19, where the rate of variation of GPC with temperature starts to change at about the same temperatures that the Gibbs free energies of adsorption of the precursors change sign to positive.

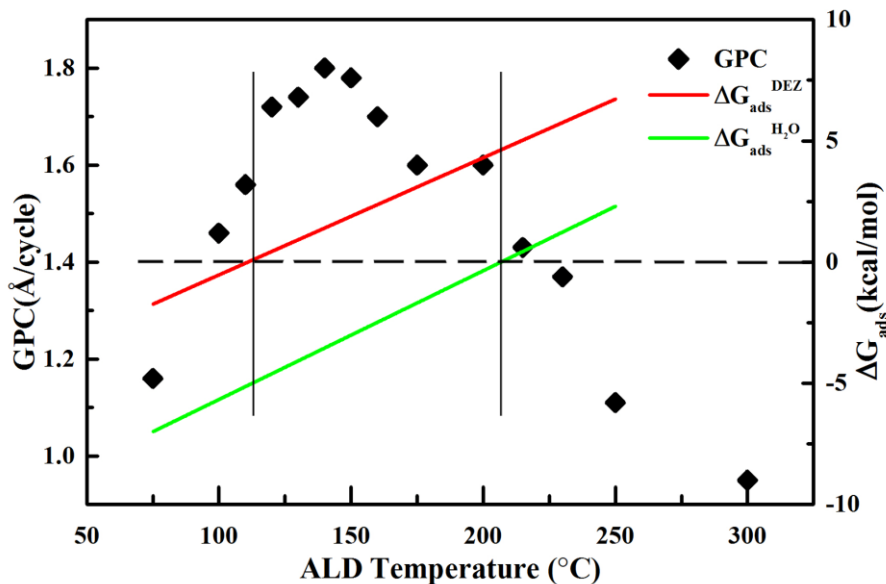


**Figure 4.19** Temperature-dependent variation of GPC, and Gibbs free energies of adsorption of DEZ and H<sub>2</sub>O during ALD of ZnO. The rate of variation of GPC with temperature changes approximately at the same temperature that the Gibbs free energies of adsorption of precursors become positive.

Elimination of  $-\text{OH}^*$  surface sites at elevated temperatures has been mentioned as another reason for the drop of GPC [53]. We studied the reaction between two neighboring  $\text{Zn-OH}^*$  at the B3LYP/6-311G(d) level to find the related thermochemistry. The corresponding reaction is shown as follows [134]:



In this reaction two neighboring hydroxyl groups on the surface react and form a Zn-O-Zn bridge and H<sub>2</sub>O eventually desorbs from the surface. Our findings show that the transition energy for this reaction lies 22.1 kcal/mol above the initial state and the overall barrier for this reaction is 50.8 kcal/mol. This value is close to what has been observed for the reaction of -OH groups on HfO<sub>2</sub> [134]. The high energy required for the transition and the desorbed states suggests that the

elimination of the surface reaction sites is less probable in the temperature range of this study.

## 4.5 Conclusions

The growth mechanisms of thermal and plasma-enhanced ALD of ZnO were studied. The saturation curves showed that the optimum values for the exposure time of DEZ, H<sub>2</sub>O, and O<sub>2</sub>-plasma are 0.02, 0.10, and 2.00s, respectively. The maximum GPC was obtained at 140 °C with a value of 1.80 Å/cycle. The optical constants of the ALD films were calculated by fitting the spectroscopy ellipsometric data to a Cody-Lorentz model and showed to meet the bulk values at deposition temperatures over 100 °C. The optical bandgaps for the samples were approximately 3.0 eV at all the deposition temperatures above 100 °C. The AFM studies showed that the roughness of the ZnO thin films decrease with the deposition temperature. This was attributed to the formation of (002) preferential orientation in ZnO crystallites at high deposition temperatures due to the much less –OH concentration on the surface and the grain boundaries. A model for the growth of ALD ZnO films was proposed based on the experimental results. The chemical composition of the samples from XPS experiment showed that the ZnO thin films had a zinc deficiency. The amount of C in the films was less than 4 at.% for all the deposition temperatures. The main source of the carbon seemed to be the decomposition of DEZ, especially at high deposition temperatures. A DFT approach to the growth mechanism of TALD ZnO revealed that the stability of the intermediate complexes, formed from adsorption of the precursors on the surface, plays an important role in the growth rate of the ZnO.

## Chapter 5

---

# Atomic Layer Deposition of Zirconium Oxide

## 5.1 Introduction

Zirconium oxide ( $\text{ZrO}_2$ ), also known as zirconia, has been investigated as a possible high- $\kappa$  oxide candidate for the gate oxide in integrated circuits. It has a permittivity value of 23 in the monoclinic phase, which can be manipulated by adding stabilizing yttria cations (3-5 at. % ) to as high as 42 [138].  $\text{ZrO}_2$  has a bandgap of 5.8 eV, which makes it a promising gate oxide for wide bandgap semiconductor devices [27, 139]. However,  $\text{HfO}_2$  is currently used for Si devices due to the reactivity of Zr with Si [140].  $\text{ZrO}_2$ - $\text{Al}_2\text{O}_3$ - $\text{ZrO}_2$  (ZAZ) dielectric stack is currently used in 60nm DRAMs [141, 142]. Moreover,  $\text{ZrO}_2$  has a good ion conductivity and can be used in fuel cells as the solid electrolyte [143].

The first ALD of  $\text{ZrO}_2$  was reported by Ritala and Leskela [144] in 1994, using  $\text{ZrCl}_4$  and  $\text{H}_2\text{O}$  as the precursors. The film was deposited between 300 and 500 °C, which was a low temperature range compared to chemical vapor deposition techniques [144-146]. Using metalorganic precursors, which have higher vapor pressure, it is possible to deposit  $\text{ZrO}_2$  at much lower temperatures [147-154]. Among this group of precursors, metal amides are widely used in ALD research and industry [155]. Metal amides (tetrakis(dimethylamido)zirconium TDMAZr, for example) have high volatility and are liquid under the vaporization conditions of ALD, which are benefits in the synthesis, purification, and handling of the precursor, which makes the ALD process more reproducible and cleaner.

Moreover, alkylamides do not harm the substrate surface by producing corrosive byproducts such as hydrochloric acid, which is one ALD byproduct chloride precursors are used [155].

Despite several studies on the application of ALD  $\text{ZrO}_2$  thin films deposited using metal amides and water or oxygen sources, there is a lack of a systematic study on the material characterization of  $\text{ZrO}_2$  ALD films [156-160]. In this chapter, the chemical composition, crystallinity, roughness, and optical characterizations of the  $\text{ZrO}_2$  ALD films deposited using TDMAZr precursor are presented and discussed. Thermal and plasma-enhanced ALD of  $\text{ZrO}_2$  at various deposition temperatures have been studied. TEM images and C-V characteristics of Cr/ $\text{ZrO}_2$ /GaN MOSCAPs show the high quality of the semiconductor/high- $\kappa$  oxide. The results show that  $\text{ZrO}_2$  is a promising candidate for GaN MOSFETs. Finally, a density functional approach to the growth mechanism of  $\text{ZrO}_2$  is presented.

## **5.2 Experimental Procedure**

The details of the ALD process and substrate preparation are discussed in Chapter 3. The saturation curves for TDMAZr,  $\text{H}_2\text{O}$ , and  $\text{O}_2$ -plasma were plotted at 200 °C to find the optimum dose times. The optimized exposure times at 200 °C were used for the deposition at all the other temperature. XPS, XRD, AFM characterization were conducted on the 20nm-thick ALD films. More details on the apparatus and the experimental conditions can be found in Chapter 3.

For the DFT study, GAUSSIAN 09 [100] was used to perform molecular orbital calculations. The geometry of stationary points were located using the

B3LYP gradient corrected density functional method [59-62] with 6-31+G(d,p) polarized double split valence basis set for nonmetallic atoms [161-168], i.e. H, C, N, and O, and Los Alamos ECP plus DZ (LanL2DZ) for Zr [169-171]. This level of theory has shown reliable results in studying growth mechanisms of ALD  $\text{ZrO}_2$  using  $\text{ZrCl}_4$  as the precursor [133, 172, 173]. The frequency calculations were carried out at the same level of theory to identify the nature of the stationary points (local minima and transition states) and to calculate the zero-point energy corrections and the thermal corrections at the ALD temperature and pressure. All reported energies are corrected by the zero-point energy correction value. In order to test the validity of the calculations, we compared our results with available experimental data whenever possible.

## **5.3 Results**

### **5.3.1 Optical Constants**

The dependence of the optical constants of TALD and PEALD of  $\text{ZrO}_2$  on deposition temperature and photon energy is shown in Figure 5.1. The refractive index increases with deposition temperature, as the crystallinity and density of the oxide improve. The maximum refractive index is obtained between 200-250 °C for both thermal and plasma-enhanced ALD oxides. These values are higher than values reported previously for films deposited by magnetron sputtering [174] and e-beam evaporation [175] and match the bulk values [176]. At higher deposition temperature ( $T > 250$  °C) the refractive index decreases due to decomposition of the precursor, which results in incorporation of impurities into the thin films [155]. A smoother change in optical profile vs. deposition temperature is observed for

TALD  $\text{ZrO}_2$  compared to PEALD (Figure 5.1). The energy imposed on the growing films by plasma species is the reason for the faster transition in optical constants.

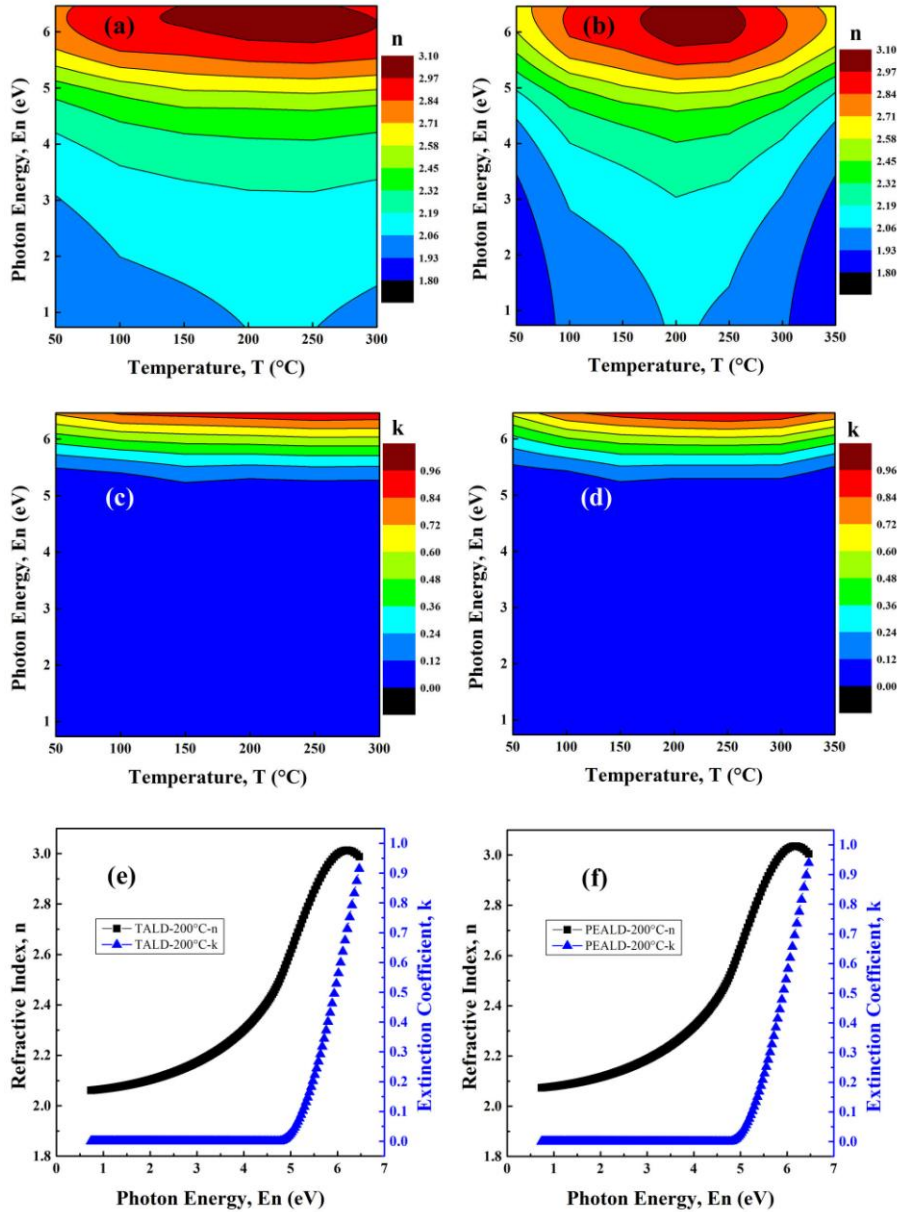


Figure 5.1 Refractive index (a,b) and extinction coefficient (c,d) of TALD (a,c) and PEALD (b,d)  $\text{ZrO}_2$  vs. the incident photon energy and ALD temperatures. For more clarity the refractive index and extinction coefficient of the samples deposited at 200 °C are shown in (e, f).

### 5.3.2 Growth Rate and Saturation Curves

Saturation curves for TDMAZr (both TALD and PEALD), H<sub>2</sub>O, and O<sub>2</sub>-plasma at 200 °C are shown in Figure 5.2. From the saturation curve of TDMAZr for the PEALD process, it is concluded that PEALD is not self-saturating, as a result of gas phase reaction between the O<sub>2</sub> and TDMAZr molecules. However, TDMAZr saturation occurs at 0.04s for the TALD process. Saturation occurs at 0.5 s, and 2.0 s for H<sub>2</sub>O, and O<sub>2</sub>-plasma, respectively. The variation of GPC values with deposition temperature is illustrated in Figure 5.3. The GPC decreases with increasing deposition temperatures and remains approximately constant at 1.0 Å/cycle above 200 °C for the TALD films. The same behavior is seen for PEALD at T<100°C. From these results it can be deduced that condensation of the TDMAZr precursor happens at deposition temperatures lower than 100 °C [177]. For PEALD, the GPC increases with the deposition temperature at T>250 °C. Since we do not see this trend for TALD process, it is concluded that a gas phase reaction between TDMAZr and molecular O<sub>2</sub> happens at high deposition temperatures, which results in high deposition rate [177]. In other words, decomposition of the precursor has less effect on the GPC of the films at high deposition temperatures.

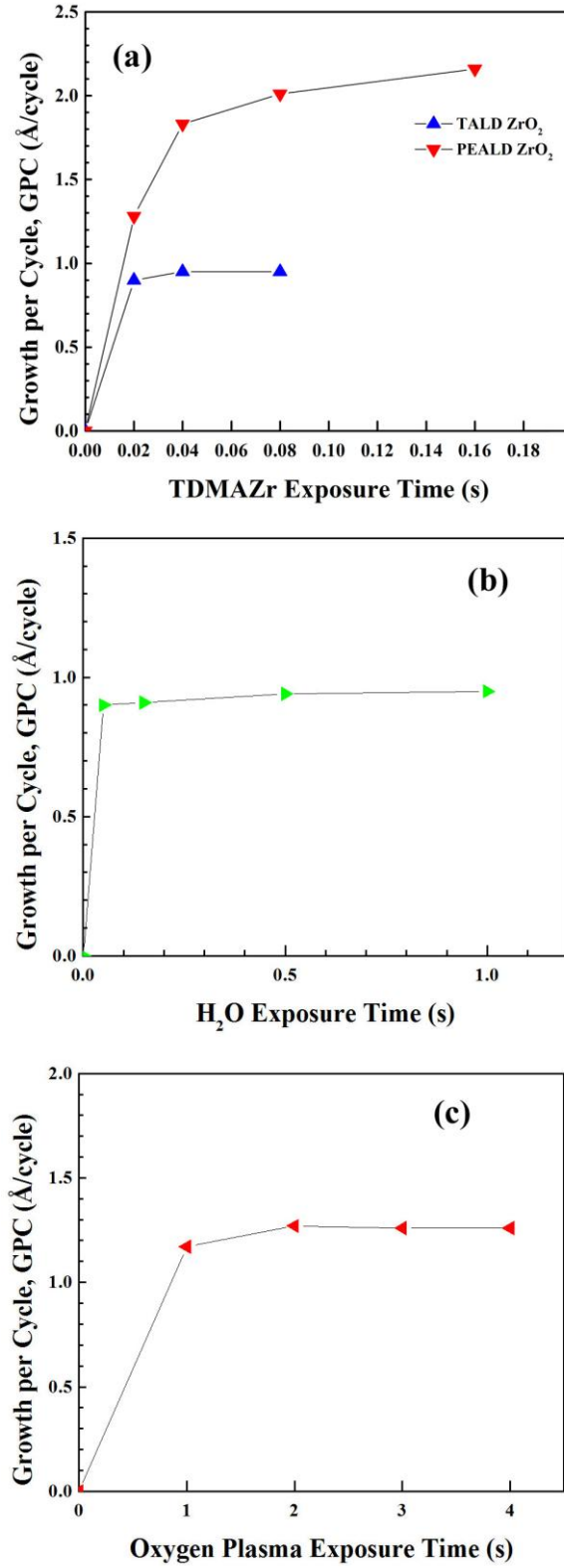


Figure 5.2 Saturation curves for the TDMAZr (a), H<sub>2</sub>O (b), and (c) O<sub>2</sub>-Plasma at 200 °C.

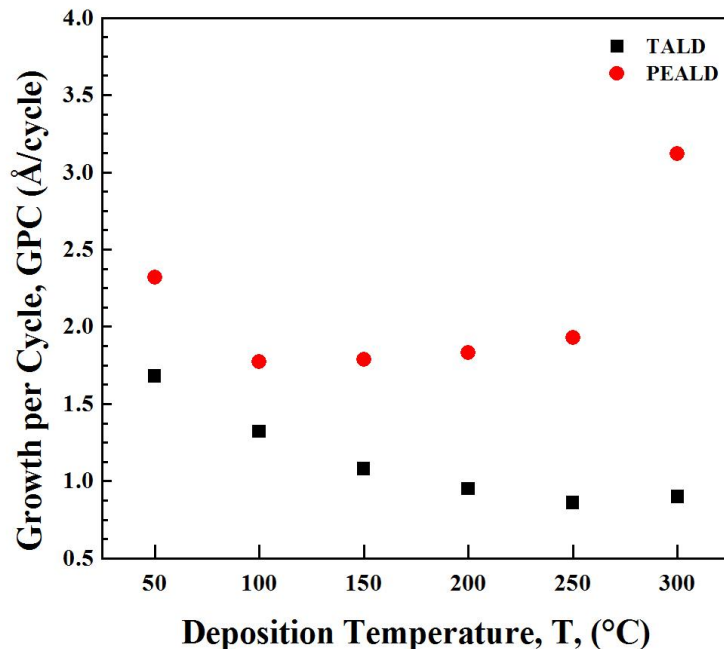


Figure 5.3 GPC of ALD  $ZrO_2$  with deposition temperature for both thermal and plasma-enhanced processes.

### 5.3.3 Chemical Composition

High-resolution XPS profiles of the ALD  $ZrO_2$  thin films are shown in Figure 5.4. The chemical composition of the zirconium oxide is summarized in Table 5.1. The  $Zr3d_{3/2}$  and  $Zr3d_{5/2}$  peaks are depicted in Figure 5.4a. The binding energy difference of 2.4eV and the intensity ratio of 1.5 agree with the published values [178]. The binding energy of  $Zr3d_{5/2}$  has been shown to vary from 180.2 eV to 182.7 eV depending on the oxidation state ( $Zr^{2+}$ : 180.2 eV,  $Zr^{3+}$ : 181.2 eV,  $Zr^{4+}(O^{2-})$ : 181.9 eV, and  $Zr^{4+}(OH)$ : 182.7 eV) [179-182].

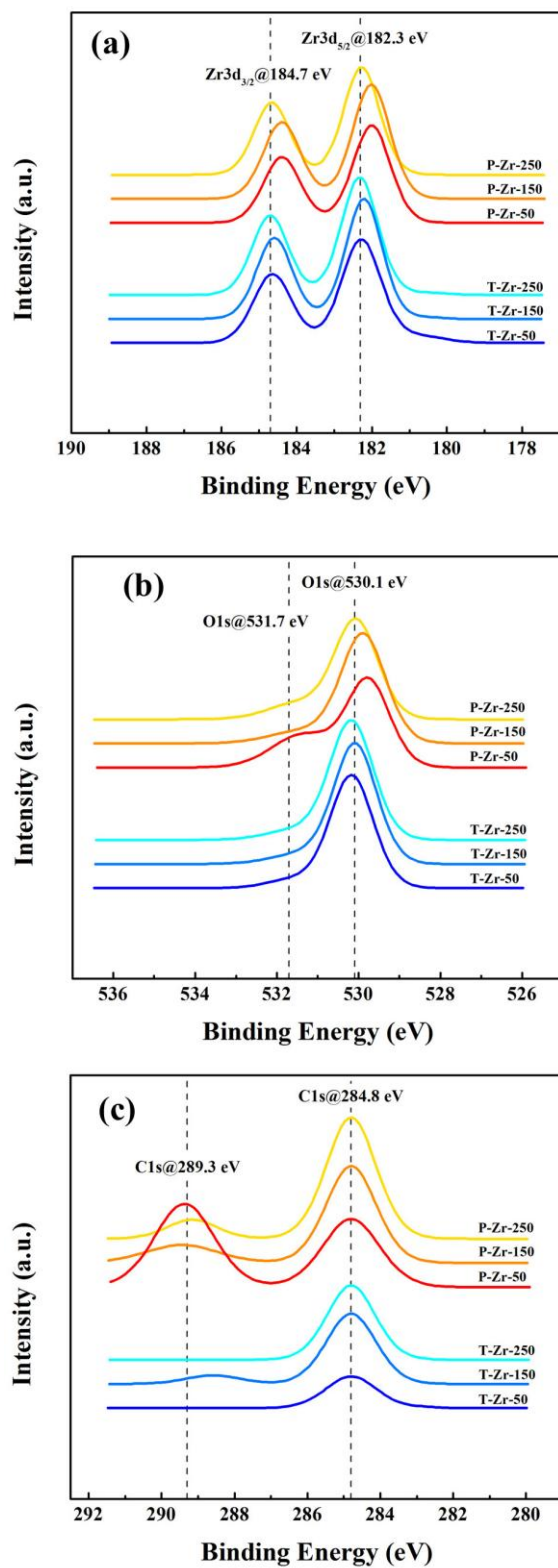


Figure 5.4 High Resolution XPS graphs of Zr3d (a), O1s (b), and C1s (c) for ALD ZrO<sub>2</sub> at different deposition conditions.

The high-resolution XPS for oxygen is shown in Figure 5.4b. The main peak at 530.1 eV is attributed to the oxygen in  $\text{ZrO}_2$  and the peak at 531.7 eV is assigned to the  $\text{Zr}^{4+}(\text{OH})$  and/or the ligand oxygen (carboxyl carbon) [180, 183]. The later peak has lower intensity in the TALD samples compared to PEALD samples. Consequently, it can be deduced the oxygen peak is mainly related to the by-products from the combustion-like reaction between the  $\text{O}_2$ -plasma species and TDMAZr molecules adsorbed on the surface. At higher temperatures, the by-products desorbed from the surface and the intensity of the ligand oxygen in the XPS profile drops sharply. The O1s peak is assigned to  $\text{Zr}^{4+}(\text{OH})$  species in the TALD films, since there is no combustion-like reaction in the thermal process. The exact position of the Zr and O peaks are shown in Table 5.1. The peaks shift to higher binding energies with increasing the deposition temperature. However, the O/Zr ratio is much less than the stoichiometric value of 2.0 in  $\text{ZrO}_2$ . This can be explained by the preferential etching of oxygen atoms by  $\text{Ar}^+$  ions during the surface cleaning of the samples prior to XPS measurements [184].

The carbon XPS profile is shown in Figure 5.4c. The main carbon, 284.8 eV, is attributed to alkyl impurities ( $\text{Zr-C}_x\text{-H}_n$ ), formed from incomplete reaction of water or  $\text{O}_2$ -plasma with TDMAZr molecules during the ALD process [183]. The peak at 289.3 eV can be assigned to carbon in carboxylates, since the intensity of the peak has the same trend as of O1s at 531.7eV for PEALD  $\text{ZrO}_2$  and this peak is not present in the TALD sample [183]. It is worthy to note that no nitrogen impurities were found in the ALD  $\text{ZrO}_2$  samples.

**Table 5.1 Chemical composition of zirconium oxide samples deposited by TALD and PEALD at various temperatures (For each sample the first row shows the binding energy in eV and the second row shows the concentration of the element in at.%)**

| Sample Name | Zr3d <sub>3/2</sub> | Zr3d <sub>5/2</sub> | O1s   | O1s   | O/Zr ratio | C1s   | C1s   |
|-------------|---------------------|---------------------|-------|-------|------------|-------|-------|
| T-Zr-50     | 184.6               | 182.2               | 531.7 | 530.2 | 1.6        | 284.8 | -     |
|             | 14.9                | 22.6                | 4.7   | 55.8  |            | 2.0   |       |
| T-Zr-150    | 184.6               | 182.2               | 531.5 | 530.1 | 1.6        | 284.8 | 288.6 |
|             | 14.7                | 22.1                | 5.8   | 53.0  |            | 3.9   | 0.5   |
| T-Zr-250    | 184.7               | 182.3               | 531.7 | 529.8 | 1.6        | 284.8 | -     |
|             | 14.7                | 22.0                | 5.2   | 54.1  |            | 4.0   |       |
| P-Zr-50     | 184.4               | 182.0               | 531.4 | 529.8 | 1.9        | 284.8 | 289.4 |
|             | 12.2                | 18.1                | 20.3  | 37.8  |            | 4.3   | 5.5   |
| P-Zr-150    | 184.4               | 182.0               | 531.5 | 529.9 | 1.6        | 284.8 | 289.4 |
|             | 14.4                | 21.3                | 7.6   | 49.9  |            | 5.4   | 1.4   |
| P-Zr-250    | 184.7               | 182.3               | 531.5 | 530.1 | 1.6        | 284.8 | 289.2 |
|             | 13.8                | 20.8                | 9.8   | 47.3  |            | 7.2   | 1.1   |

### 5.3.4 Roughness

The AFM plots of the ZrO<sub>2</sub> samples are shown in Figure 5.5, and the roughness values are reported in Table 5.2. The roughness of the samples increases with the deposition temperatures. Meanwhile, the PEALD thin films have rougher surfaces compared to TALD film grown at the same deposition temperature. The sharp peaks, and smooth areas on the surface of the samples can be attributed to the crystalline phase and amorphous phases of ZrO<sub>2</sub>, respectively.

**Table 5.2 RMS Roughness of the TALD and PEALD ZrO<sub>2</sub> deposited at various temperatures (nm) (Roughness of Si(100) substrate was 0.11 ± 0.02 nm)**

| Deposition Temperature (°C) | TALD        | PEALD       |
|-----------------------------|-------------|-------------|
| 50                          | 0.68 ± 0.06 | 3.03 ± 0.18 |
| 150                         | 2.14 ± 0.15 | 4.12 ± 0.47 |
| 250                         | 1.84 ± 0.18 | 4.85 ± 0.41 |

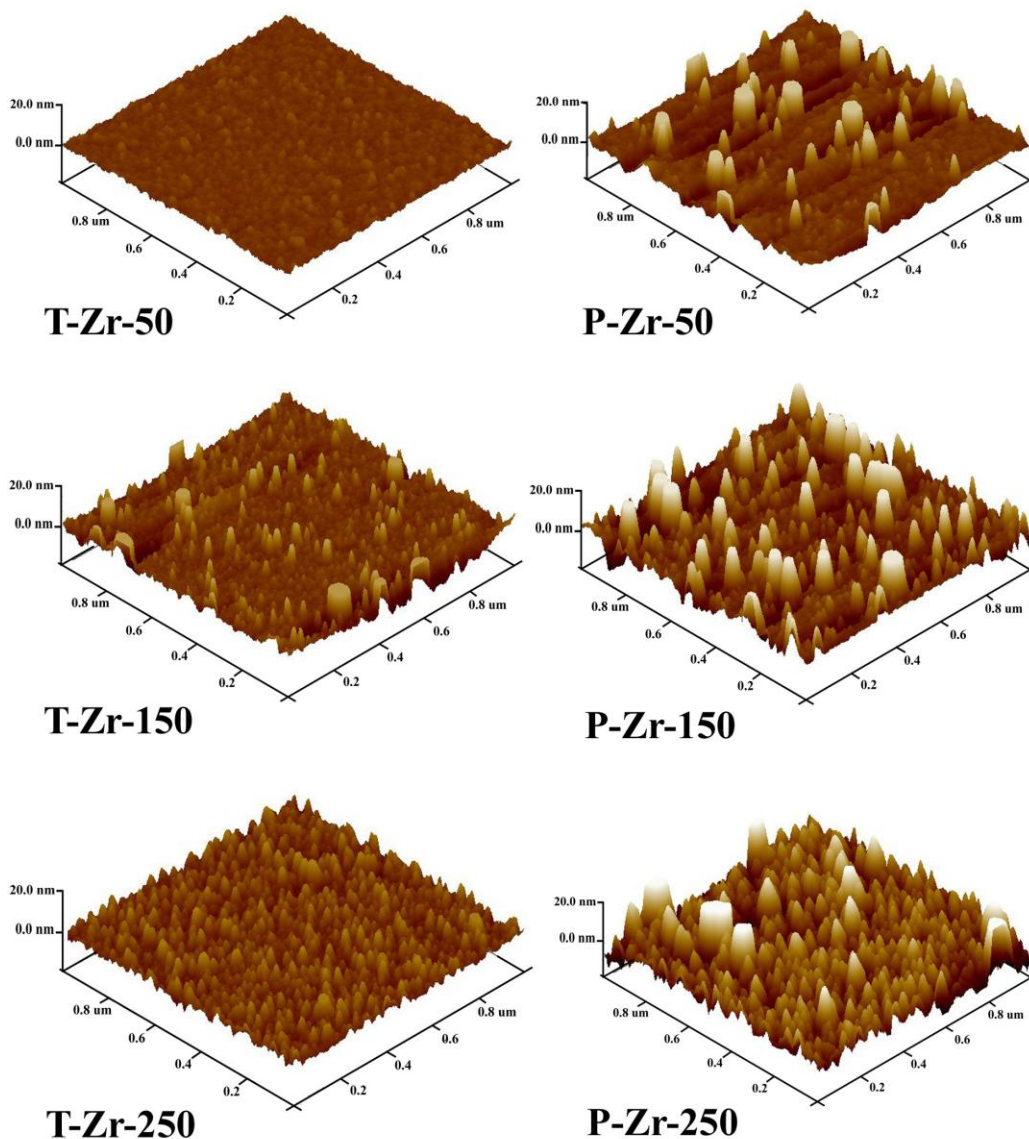


**Figure 5.5 AFM surface plots of the ALD  $ZrO_2$  deposited at different temperatures using thermal and plasma-enhanced approaches.**

From the AFM graphs it is concluded that the thin films are initially amorphous, and crystalline phases nucleate randomly in this amorphous layer [122, 125]. The incoming precursor molecules arriving on the crystalline phase adopt the crystalline structure, and the materials landing on the amorphous phase

take the amorphous form. Increasing the deposition temperature results in a higher rate of crystal nucleation, and as a result more crystalline phase forms. This increases the roughness of the surface. Using plasma as the oxidizing reagent results in higher crystalline phase nucleation due to the energy induced to the films from the plasma source. This explains the higher roughness of the PEALD samples. This model explains results in the existing literature [122, 142, 155, 185]. According to this model, the lateral size of the peaks in the AFM images should increase with the number of the ALD cycles, which agrees well with the existing studies [144]. The crystallinity of the ZrO<sub>2</sub> is discussed in more details in the next section, where XRD results of the thin films are presented.

### 5.3.5 Crystallinity

Figure 5.6 shows the XRD results for the ALD ZrO<sub>2</sub> films. As expected from the AFM results, the films deposited at low temperatures show no crystalline characteristics in the XRD profile. The peaks start to appear with increasing the deposition temperature. The samples deposited at 250 °C show the characteristic of cubic zirconia. The monoclinic phase is the most stable polymorph for bulk ZrO<sub>2</sub> at temperatures below 1150 °C. At high temperatures, tetragonal and cubic phases can be found [186, 187]. However, surface energy plays an important role in the evolution of thin film structures. It has been shown that the monoclinic to tetragonal phase transition temperature shifts to lower temperature regime as a result of decreasing the crystalline size of the ZrO<sub>2</sub> [188, 189]. The cubic structure has even lower surface energy than monoclinic and tetragonal phases and is more energetically favorable for smaller crystallites [190].

To summarize the AFM and XRD results, the ALD of zirconia starts as an amorphous phase and the crystallites nucleate inside this phase, regardless of the precursor chemistry [125]. Increasing the ALD temperature improves surface diffusion and lowers the required number of ALD cycles for the crystalline phase to nucleate and increases the number of the nucleation sites. A schematic view of the crystallites nucleation and growth is shown in Figure 5.7.

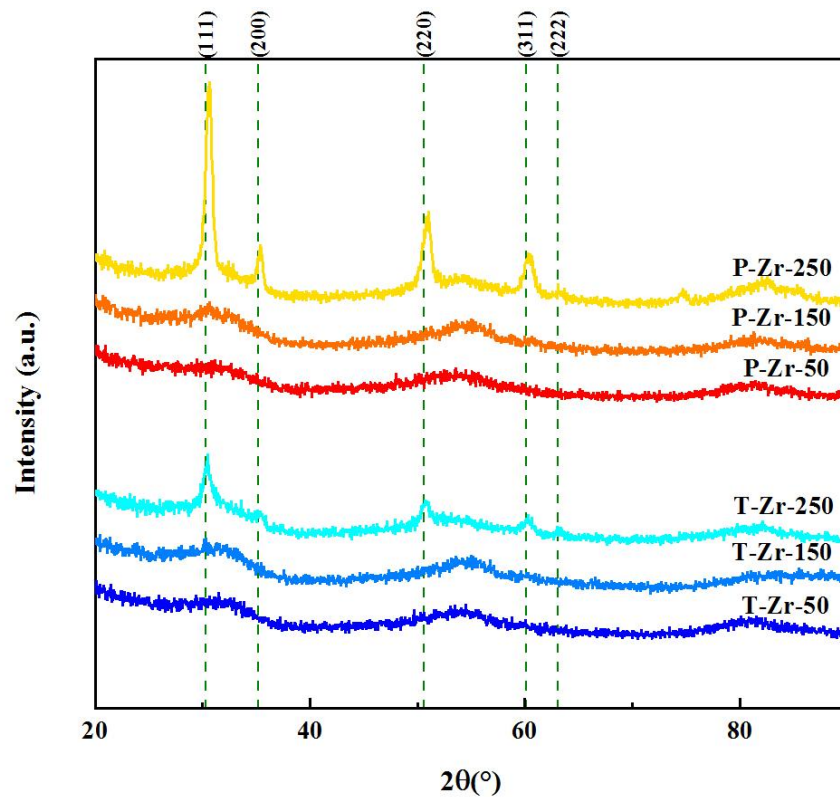
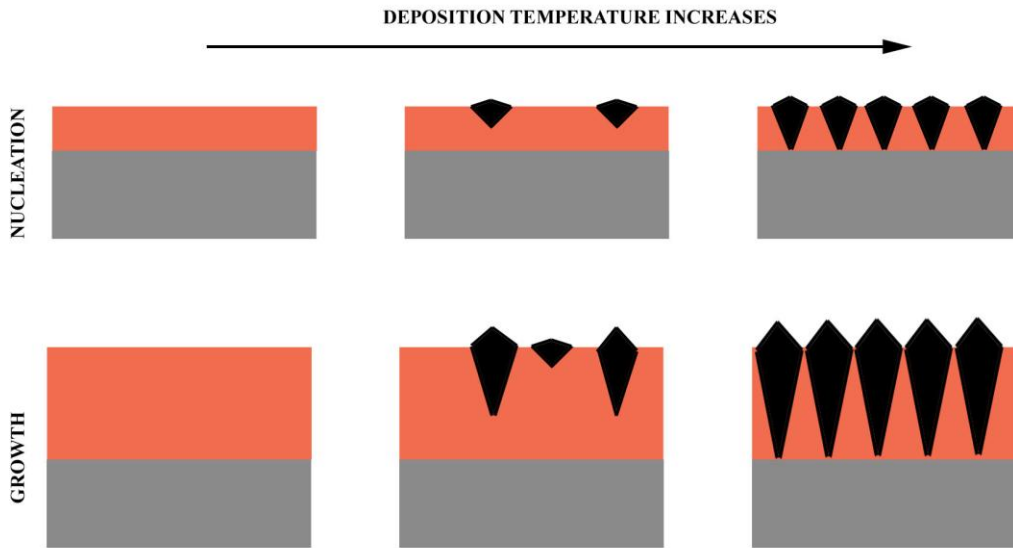


Figure 5.6 XRD profiles of the ALD  $ZrO_2$  samples deposited by thermal and plasma-enhanced ALD processes at different deposition temperatures.



**Figure 5.7** A schematic model for crystallites nucleation and growth in  $\text{ZrO}_2$  and  $\text{HfO}_2$  thin films fabricated by ALD. The grey, orange, and black areas show the substrate, amorphous phase, and crystalline phase of the ALD oxides.

#### 5.4 Characterization of $\text{Cr}/\text{ZrO}_2/\text{GaN}$ MOS<sup>‡</sup>

The bright-field TEM images of  $\text{Cr}/\text{P-Zr-100}/\text{GaN}$  (0001) MOS structure are shown in Figure 5.8. The TEM images show the well-defined  $\text{ZrO}_2/\text{GaN}$  interface. The polycrystalline nature of the  $\text{ZrO}_2$  in the TEM sample is the result of the post-annealing at 415 °C. The thickness of the oxide calculated from the TEM image ( $9.1 \pm 0.5$  nm after 58 cycles of ALD) matches appropriately the growth rate obtained from the ellipsometry data.

<sup>‡</sup> A version of this section has been published. von Hauff et al. Appl. Phys. Lett. 102 (2013) 25160.

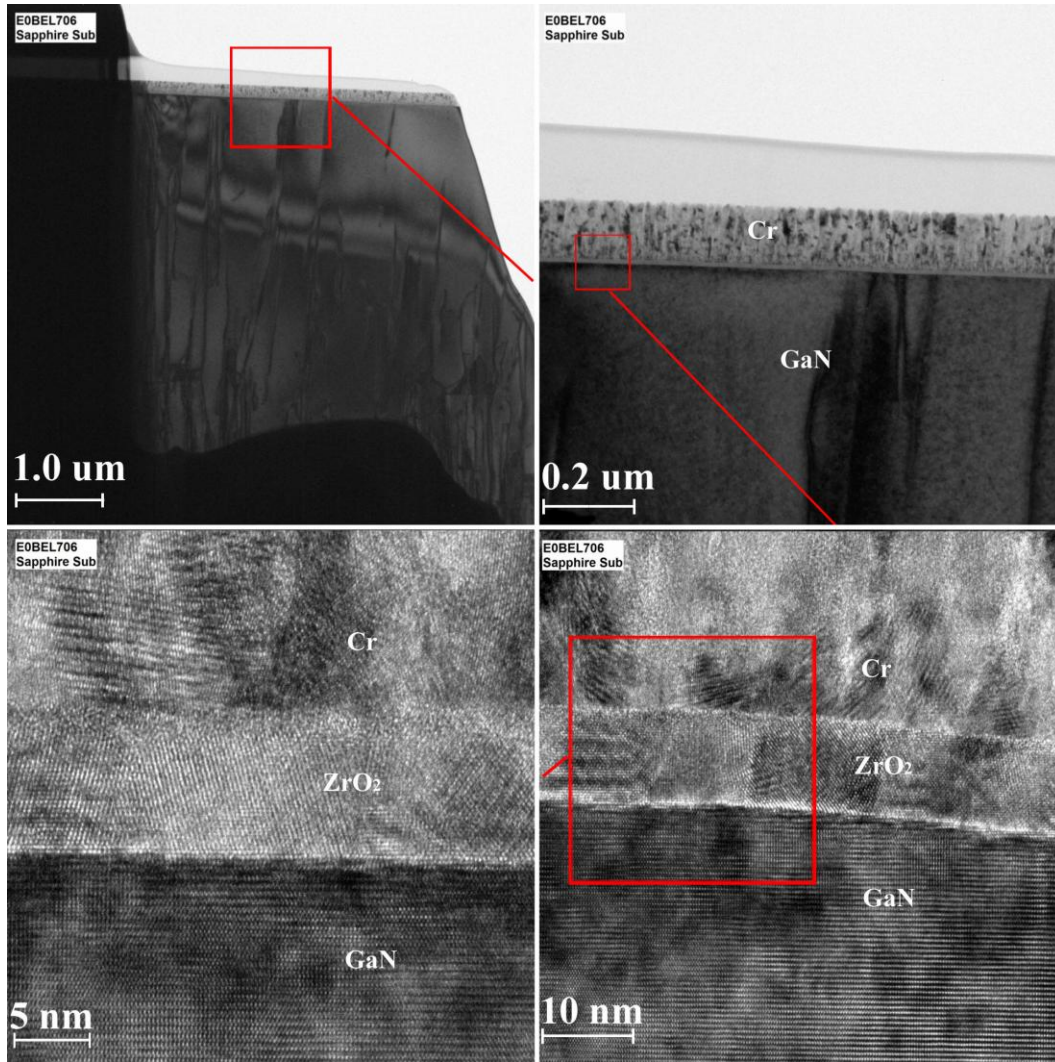


**Figure 5.8 TEM image of Cr/ZrO<sub>2</sub>/GaN MOS structure revealing the polycrystalline microstructure of ZrO<sub>2</sub> and the quality of the ZrO<sub>2</sub>/GaN interface.**

The C-V characteristic of the MOSCAPs is represented in Figure 5.9. The raw data is treated by transformation of a circular distributed capacitance model [159]. The hysteresis in the C-V measurements is 6mV at 20 kHz. The interface trap density,  $D_{it}$ , is calculated from equation 5.1 [191].

$$D_{it} = \frac{\Delta V \cdot C_{ox}}{q} \quad (5.1)$$

For the 6.8 nm PEALD ZrO<sub>2</sub>, we found  $D_{it} = 3.2 \times 10^{10} \text{ cm}^{-2} \text{ eV}^{-1}$ , which revealed the excellent quality of the interface.

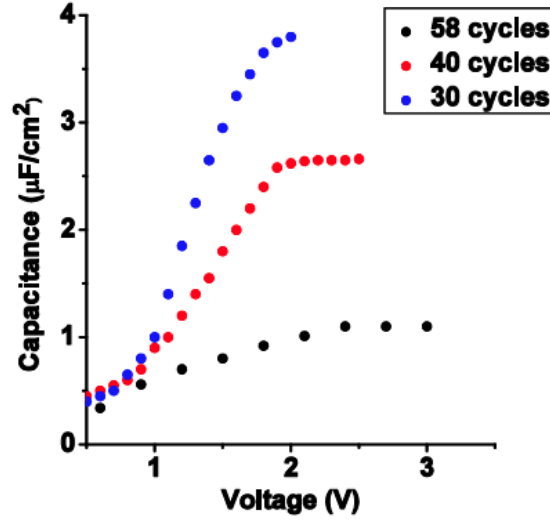
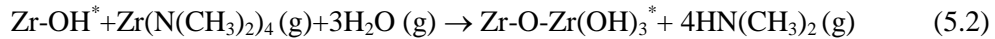


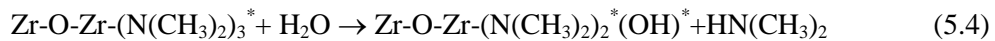
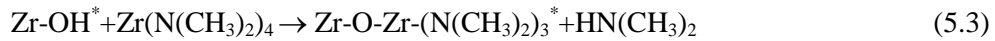
Figure 5.9 C-V characteristics of the Cr/P-Zr-100/GaN MOSCAPs.

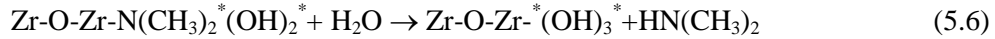
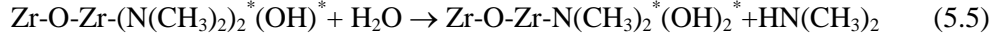
## 5.5 Growth Mechanism of TALD ZrO<sub>2</sub>: DFT Approach

The chemical reactions involved in the adsorption of TDMAZr and H<sub>2</sub>O on the growing film surface and desorption of the byproducts from the surface are discussed in this section. The overall ALD reaction for formation of one monolayer of ZrO<sub>2</sub> from TDMAZr and H<sub>2</sub>O is:



where the \* shows the species on the surface and (g) shows the species in the gas phase. This reaction can be split into 4 partial reactions (5.3 to 5.6).





The first half-reaction involves the reaction between TDMAZr and the Zr-OH\* reaction sites on the surface. The reaction pathway of this partial reaction is depicted in Figure 5.10. The cluster model has been used before for the growth mechanism of ALD ZrO<sub>2</sub> from ZrCl<sub>4</sub> as the precursor [133]. We used a Zr<sub>4</sub>O<sub>9</sub>H<sub>3</sub>(OH) cluster, **I**, to model the ZrO<sub>2</sub> surface. Although using a large cluster costs more computational time, it mimics the effect of surrounding atoms much better than a smaller cluster. The size of the cluster can affect the calculated energies and the optimal size should be determined [132]. However, in this thesis it is assumed that our cluster is big enough to consider the effect of the neighboring atoms on the reaction. One of the OH groups is considered as the reaction site. The other H atoms, terminating the Zr-O bonds, are needed to satisfy charge neutrality in the crystal. The ZrO<sub>2</sub> cluster has a cubic crystallinity and the Zr-O and Zr-Zr bond lengths are 2.00 and 3.55 Å, respectively. The Zr-O-Zr and O-Zr-O bond angles are 125.7 and 100.3°. These values match closely the values for cubic ZrO<sub>2</sub> nanocrystalline stabilized at room temperature [192]. The optimized geometry of TDMAZr is shown in Figure 5.10, **2**. For the TDMAZr molecule the calculated bond length and angles are as follows; Zr-N: 2.09 Å, N-C: 1.46 Å, C-H: 1.10 Å, Zr-N-C: 124.1°, N-Zr-N: 109.7°, and C-N-C: 111.8°. These values agree well with the results obtained from gas-phase electron diffraction by Hagen et al. [193]: Zr-N:2.07 Å, N-C:1.46 Å, C-H: 1.12 Å, Zr-N-C: 124.4°, N-Zr-N:109.5°, and C-N-C: 111.2°. The calculated vibrations for ZrN<sub>4</sub> symmetric stretch, NC<sub>2</sub> symmetric and antisymmetric stretches, and CH<sub>3</sub> rocking,

deformation, and symmetric stretches are all in agreement within the 5% error of the experimental values from Kim et al. [194].

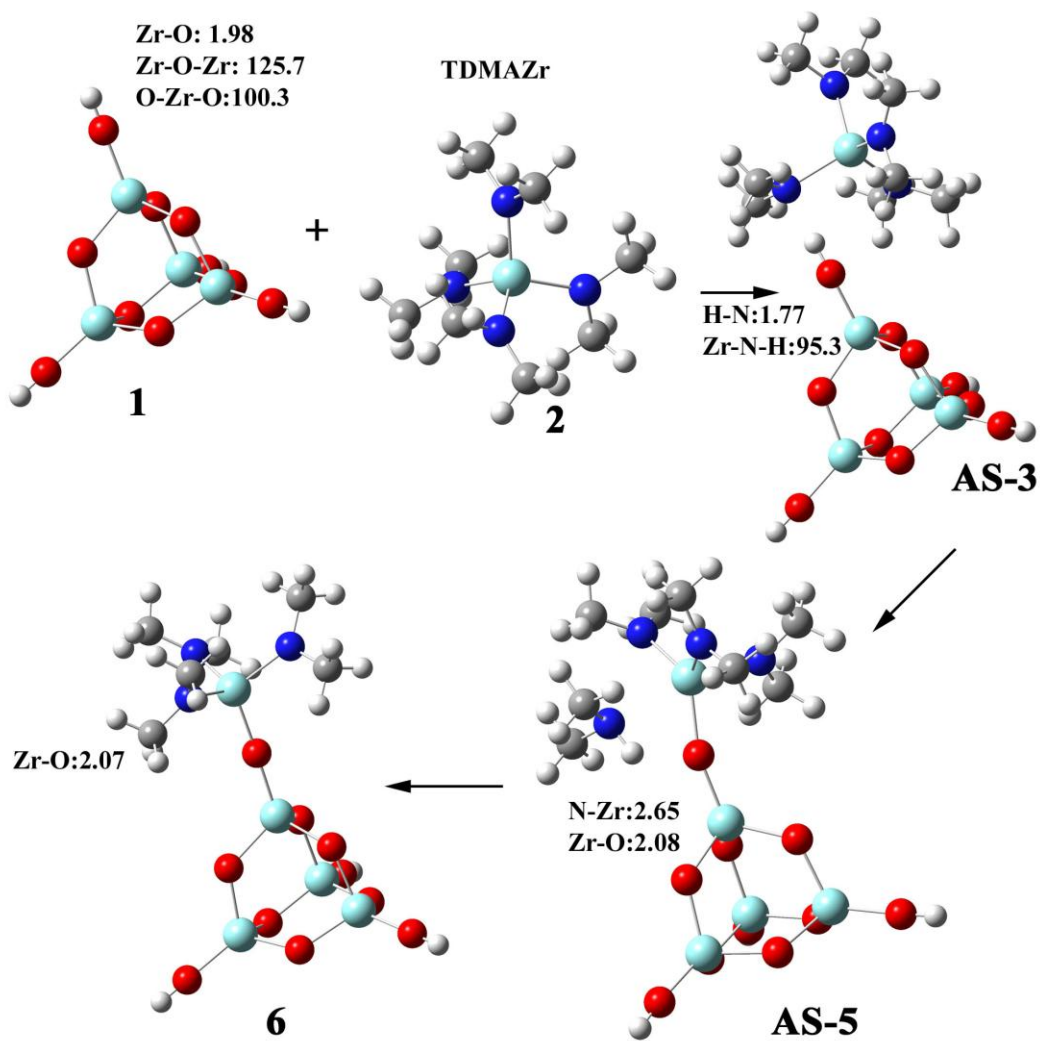
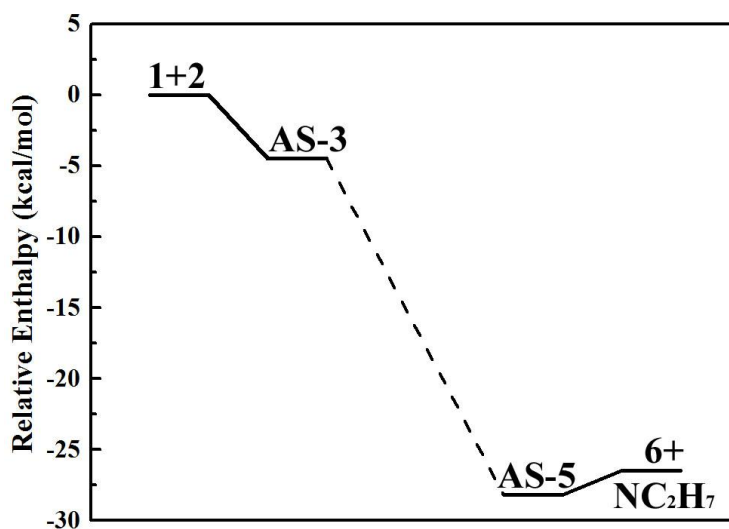


Figure 5.10 Reaction path for first partial reaction of ZrO<sub>2</sub> ALD, involving TDMAZr and Zr-OH\* surface reaction sites. The bond lengths are reported in Å and the angles are reported in °.



**Figure 5.11** PES of the first partial reaction of the ALD  $\text{ZrO}_2$ , between TDMAZr and  $-\text{OH}$  surface reaction sites.

The potential energy surface (PES) of the first partial reaction is shown in Figure 5.11. The reaction starts by adsorption of TDMAZr on the surface, *AS-3*. The  $-\text{OH}$  group on the surface points towards one of the N atoms in TDMAZr. The N-H distance is 1.77 Å and the O-H bond stretches from 0.96 Å to 1.00 Å. This is an indication of the formation of a hydrogen bond between H in  $-\text{OH}^*$  and N in TDMAZr. The calculated adsorption energy is 4.5 kcal/mol. The adsorption energy value and the N-H distance are very close to reported values for the OH...N hydrogen bond [195]. Unfortunately, the geometry calculations for the transition structure did not converge. However, from the post-transition structure it is deduced that the reaction continues by proton transfer,  $\text{H}^+$ , from  $-\text{OH}^*$  to the N in the transition state, *TS-4*. In the post-transition state, *AS-5*, the  $\text{HN}(\text{CH}_3)_2$  formed and adsorbed on the surface. This structure is located 28.2 kcal/mol lower than the reactants on the PES. The N atom in adsorbed  $\text{HN}(\text{CH}_3)_2$  points towards the Zr at a distance of 2.65 Å. A bond is formed between O on the surface and the

Zr with a length of 2.08 Å. In the desorbed state, **6**, this bond shortens to 2.01 Å. The desorbed state is located 1.7 kcal/mol above the *AS-5* on the PES. The low value of enthalpy of desorption indicates the byproduct can easily desorb from the surface. Overall, the first partial reaction is exothermic.

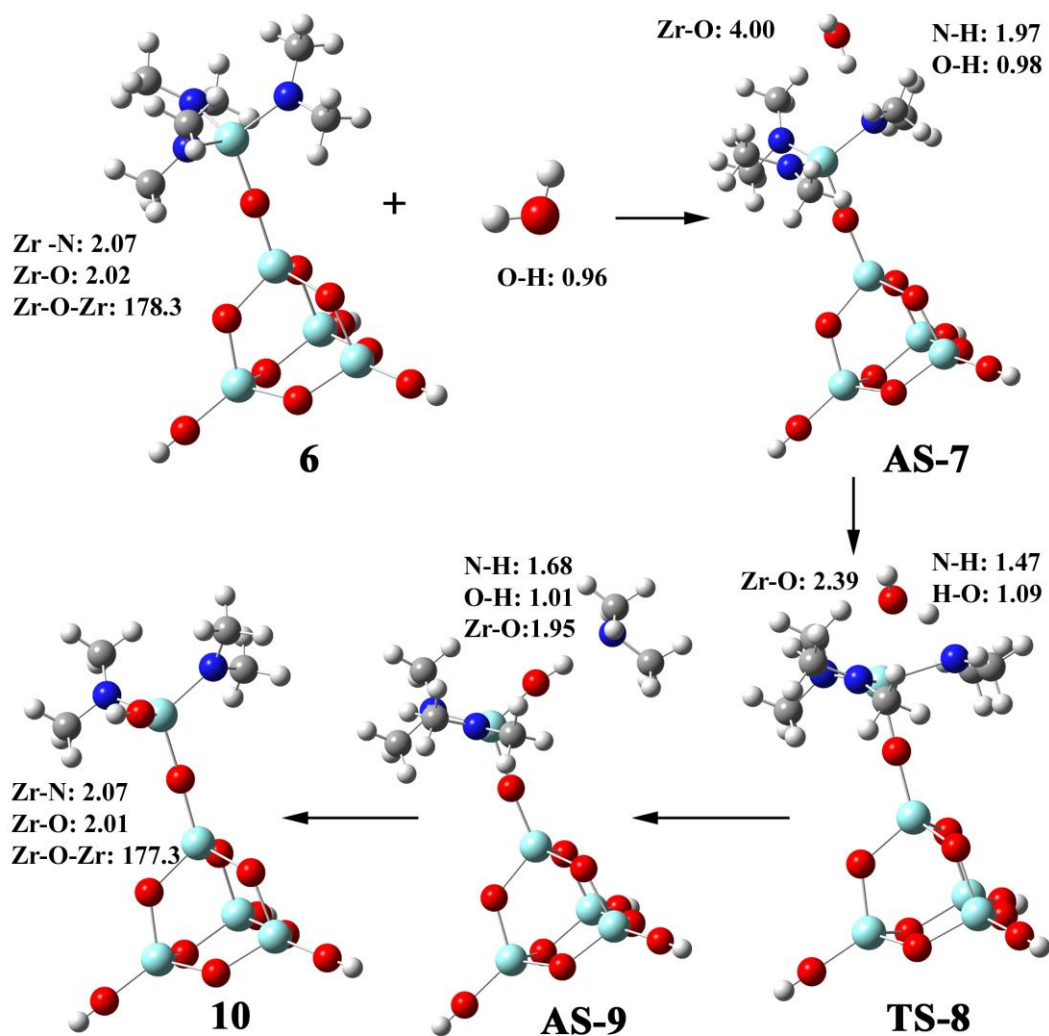


Figure 5.12 Reaction path for second partial reaction of ZrO<sub>2</sub> ALD, involving H<sub>2</sub>O and -Zr-(N(CH<sub>3</sub>)<sub>2</sub>)<sub>3</sub>\* surface reaction sites. The bond lengths are reported in Å and the angles are reported in °.

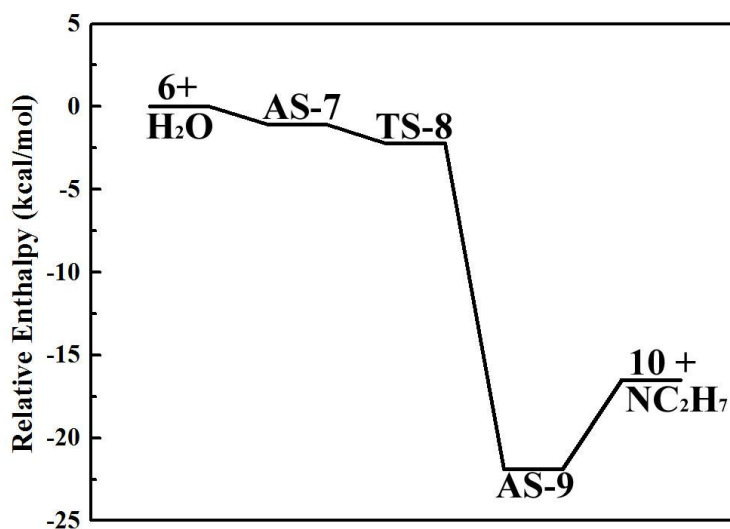
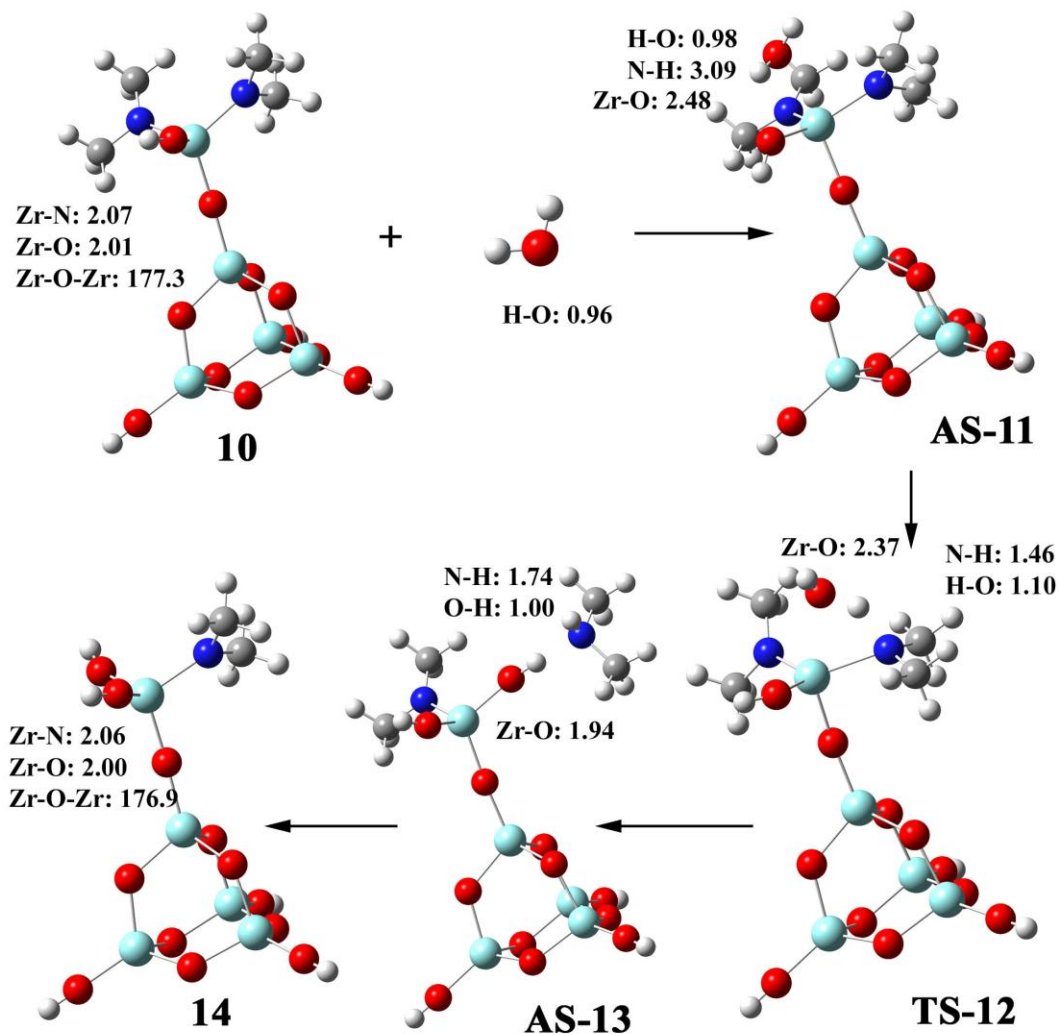


Figure 5.13 PES of the second partial reaction of the ALD ZrO<sub>2</sub>, between H<sub>2</sub>O and -Zr-(N(CH<sub>3</sub>)<sub>2</sub>)<sub>3</sub><sup>\*</sup> surface reaction sites.

The second partial reaction (reaction 5.4) occurs between H<sub>2</sub>O molecules and -Zr-(N(CH<sub>3</sub>)<sub>2</sub>)<sub>3</sub><sup>\*</sup>, **6**, on the surface. The reaction pathway is shown in Figure 5.12. The water is adsorbed on the surface via formation of a hydrogen bond between HOH...N(CH<sub>3</sub>)<sub>2</sub>, **AS-7**. The distance between N and H atoms is 1.97 Å and the OH bond in water stretches from 0.96 Å to 0.98 Å. The adsorption releases 1.1 kcal/mol energy, as shown in Figure 5.13. The reaction continues by formation of a four-center-transition state between Zr-O-N-H atoms, **TS-8**. The transition vector is dominated by the movement of H from water to N to form a HN(CH<sub>3</sub>)<sub>2</sub> molecule. The PES shows that the second half-reaction is barrier-less. The distance between O and H becomes larger, 1.09 Å, and H atom is closer to the N atom, 1.47 Å. The distance between Zr and O becomes shorter, from 4.00 Å in **AS-7** to 2.39 Å in **TS-8**. In the post-transition structure, **AS-9**, the HN(CH<sub>3</sub>)<sub>2</sub> is formed. The newly formed -OH on the surface is pointing towards the N atom at a distance of 1.68 Å, indicating the formation of a hydrogen bond. The newly

formed Zr-O bond is 1.95 Å long. The overall enthalpy change for the second partial reaction is -16.5 kcal/mol.



**Figure 5.14** Reaction pathway for the third partial reaction of ZrO<sub>2</sub> ALD, involving H<sub>2</sub>O and  $-\text{Zr}(\text{OH})-(\text{N}(\text{CH}_3)_2)_2^*$  surface reaction sites. The bond lengths are reported in Å and the angles are reported in °.

The reaction pathway and PES of the third partial reaction (reaction 5.5) are shown in Figures 5.14 and 5.15, respectively. The third partial reaction starts by adsorption of H<sub>2</sub>O on the surface, *AS-11*. A hydrogen bond forms between the H in the water molecule and O on the surface (formed in the last partial reaction).

The enthalpy change is -4.9 kcal/mol, which is higher than the same reaction in the second partial reaction. It seems that another weak hydrogen bond formed between the other H in the water and the one of the N on the surface. The distance between the O in H<sub>2</sub>O and Zr on the surface is 2.48 Å. This distance shortens to 2.37 Å in the transition state, *TS-12*. The water molecule rotates and the N-H distance becomes shorter, from 3.09 to 1.46 Å. The four-center transition state is formed between N-H-O-Zr and movement of H from water to N dominates the transition vector. The transition state is 2.5kcal/mol above the *AS-11* but is still 2.4 kcal/mol lower than the reactants. The post-transition state, *AS-13*, is located 22.6 kcal/mol lower than reactants on the PES. A hydrogen bond is formed between newly formed OH on the surface and HN(CH<sub>3</sub>)<sub>2</sub> molecules, as the OH points towards the N at a distance of 1.74 Å. Desorption of the byproduct from the surface is endothermic, 6.3 kcal/mol. However, the total enthalpy change for the third partial reaction is -16.3 kcal/mol. The Zr-O bond length is 2.00 Å in the byproduct on the surface, *14*.

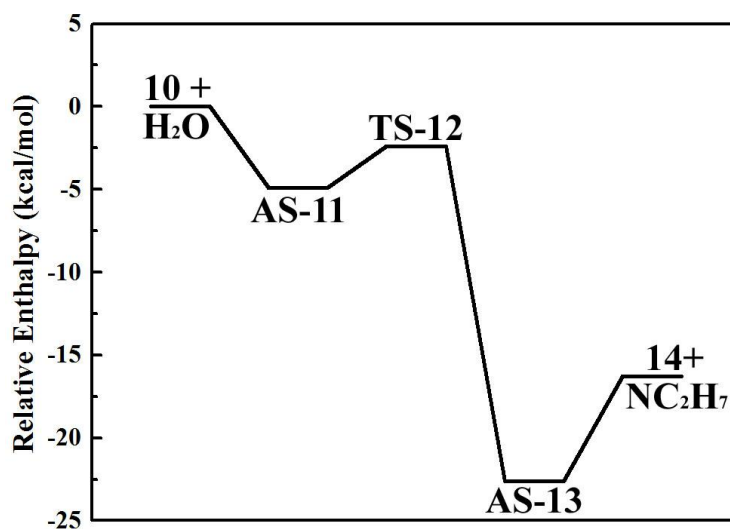


Figure 5.15 PES of the third partial reaction of the ALD ZrO<sub>2</sub>, between H<sub>2</sub>O and -Zr-(N(CH<sub>3</sub>)<sub>2</sub>)<sub>2</sub>\* surface reaction sites.

The fourth partial reaction (reaction 5.6) is very similar to the third one. The reaction pathway and the corresponding PES are shown in Figures 5.16 and 5.17. The enthalpy energy of adsorption of water on the surface is -6.8 kcal/mol, *AS-15*. The transition state, *TS-16*, locates 4.0 kcal/mol above the *AS-15* and the reaction mechanism is the proton transfer from water to N and formation of HN(CH<sub>3</sub>)<sub>2</sub>. The post-transition state, *AS-17*, is located -23.2 kcal/mol lower than reactants. The overall reaction is exothermic by a value of -16.4 kcal/mol. The Zr-O in the final state, *18*, is 1.98 Å.

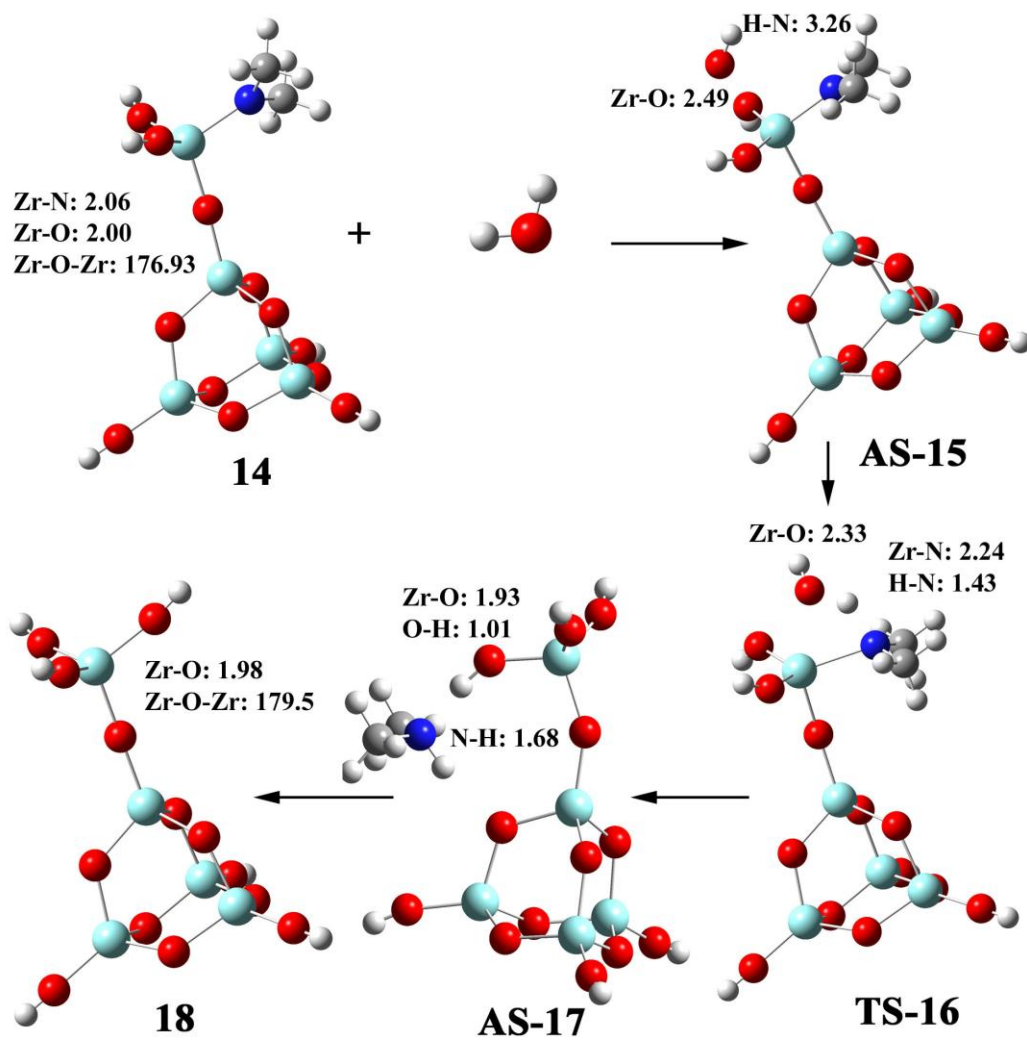
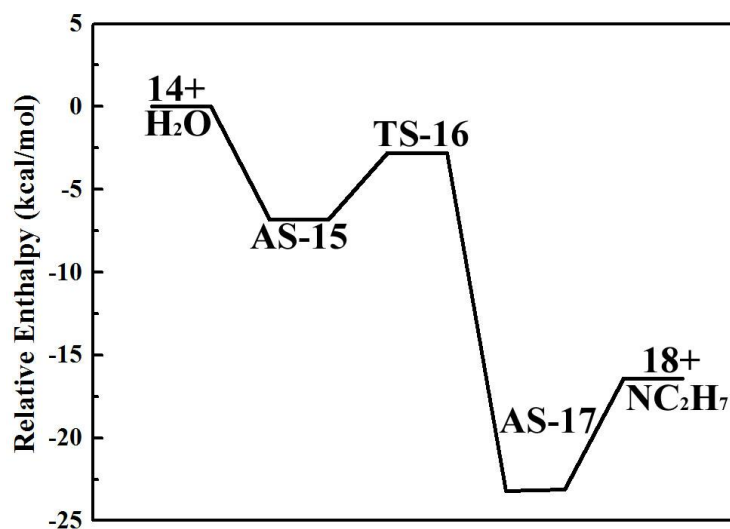


Figure 5.16 Reaction path for fourth partial reaction of  $\text{ZrO}_2$  ALD, involving  $\text{H}_2\text{O}$  and  $-\text{Zr}(\text{OH})_2-\text{N}(\text{CH}_3)_2^*$  surface reaction sites. The bond lengths are reported in Å and the angles are reported in °.



**Figure 5.17** PES of the fourth partial reaction of the ALD ZrO<sub>2</sub>, between H<sub>2</sub>O and –Zr(OH)<sub>2</sub>-N(CH<sub>3</sub>)<sub>2</sub>\* surface reaction sites.

It is concluded from the previous discussion that all the ALD half-reactions involve formation of intermediate complexes. These complexes form between TDMAZr and Zr-OH\* in the 1st half-reaction, *AS-3*, and between H<sub>2</sub>O and surface reaction site in 2<sup>nd</sup> to 4<sup>th</sup> half-reactions, *AS-7*, *AS-11*, and *AS-17*. The variations of the Gibbs free energy of formation of these complexes with temperature are shown in Figure 5.18 along with GPC of ALD ZrO<sub>2</sub>. The calculated Gibbs free energies of formation of the surface complexes at the ALD chamber pressure, 1.0 torr, are positive at all the deposition temperatures. This justifies to the dependence of GPC on deposition temperature. The decrease of GPC with deposition temperature is consistent with the DFT results. It must be mentioned that here we have not considered the possibility of the reaction of TDMAZr with two –OH\* groups on the surface simultaneously. This mechanism could also affect the growth mechanism and growth rate of the ALD oxide and it should be considered in future work.

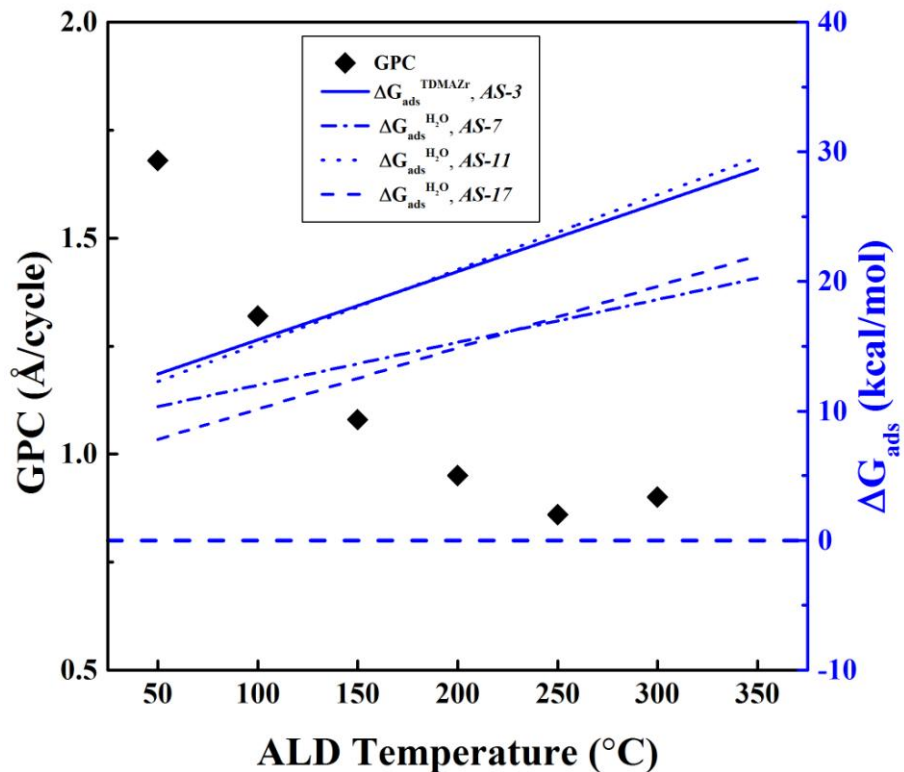


Figure 5.18 Temperature-dependent variation of GPC, and Gibbs free energies of adsorption of TDMAZr and H<sub>2</sub>O during ALD of ZrO<sub>2</sub>.

## 5.6 Conclusions

A model for the growth mechanism of thermal and plasma-enhanced ALD ZrO<sub>2</sub> was represented. The saturation curves showed that the optimum values for the exposure time of TDMAZr, H<sub>2</sub>O, and O<sub>2</sub>-plasma are 0.04, 0.50, and 2.00s, respectively. The GPC decreased with deposition temperature and leveled off at temperatures above 150 °C for both TALD and PEALD. However, a rapid increase in GPC of PEALD ZrO<sub>2</sub> was observed due to the gas phase reaction of TDMAZr and O<sub>2</sub> molecules. The optical constants of the ALD films were calculated by fitting the spectroscopic ellipsometry data to a Tauc-Lorentz model

and agreed with the bulk values at the deposition temperatures. The optical bandgaps for the samples were approximately 5.0 eV at all the deposition temperatures with a slight drop at higher temperatures. The AFM studies showed that the roughness of the ZrO<sub>2</sub> thin films increases with the deposition temperature due to formation of crystallites. The XRD results showed that the crystallites have a cubic crystal structure. Based on these results, a model for the growth of ALD ZrO<sub>2</sub> films was proposed. The TEM images revealed the well-defined nature of the GaN/ZrO<sub>2</sub> interface. The density of interface trap states was shown to be  $3.2 \times 10^{-10} \text{ cm}^{-2} \text{ eV}^{-1}$  by the C-V measurements. The chemical compositions of the thin films were studied with XPS. It was found that ALD ZrO<sub>2</sub> was free from any N contamination. The amount of C in the samples varied from 2.0 to 9.8 at.% depending on the deposition temperature. The PEALD contained higher amount of carbon due to decomposition of TDMAZr. A DFT approach to the growth mechanism of TALD ZrO<sub>2</sub> was represented.

## Chapter 6

---

# Atomic Layer Deposition of Hafnium Oxide

## 6.1 Introduction

Hafnium oxide ( $\text{HfO}_2$ ) has a high dielectric constant of 22-25 and a large bandgap of 5.5-6.0 eV [196, 197]. It is more stable than  $\text{SiO}_2$  (-53 kcal/mol higher heat of formation) and it has 1.48 eV and 3.04 eV barrier heights at the interface with Si for conduction and valence bands, respectively [196]. Hafnia also has good thermal and chemical stability with Si [198]. These properties made  $\text{HfO}_2$  an ideal gate oxide to replace  $\text{SiO}_2$  in MOSFETs (Metal-Oxide-Semiconductor Field-Effect-Transistors), which are the main components of the CMOS (complementary metal oxide semiconductor) devices [139].  $\text{HfO}_2$  is already used in 32-nm (2<sup>nd</sup> Generation Gate-Last High-k Metal Gate) and 22-nm (First to Implement Tri-Gate) Intel transistors [199].  $\text{HfO}_2$  has been studied as the gate material for the enhanced channel mobility MOSFETs, using III-V semiconductors such as GaN [200, 201]. The conduction and valence band offsets for  $\text{HfO}_2/\text{GaN}$  are 1.1 and 1.6 eV, respectively and the conduction band offset for  $\text{HfO}_2/\text{ZnO}$  is 2.2 eV [27].

ALD of  $\text{HfO}_2$  has been performed using different precursor materials. Hafnium halides ( $\text{HfCl}_4$  and  $\text{HfI}_4$ ) were used successfully to grow  $\text{HfO}_2$  at high deposition temperatures (330-500 °C) [202, 203]. However, using halides as the precursor resulted in highly crystalline films, which are not favorable because of high leakage current [144, 204-206]. The crystalline nature of the ALD  $\text{HfO}_2$  using

halides was attributed to the high deposition temperature of the process. ALD using halides at low deposition temperatures showed high level of impurities in the films [207]. ALD of HfO<sub>2</sub> using anhydrous hafnium nitrate (Hf(NO<sub>3</sub>)<sub>4</sub>) also needs post-annealing at temperatures above 400 °C to remove NO<sub>3</sub> and NO<sub>2</sub> contaminations [208]. Consequently, complex metalorganics precursors have been studied for HfO<sub>2</sub> ALD as a route to low deposition temperatures [154, 209, 210]. Metal amides are highly reactive and can react at temperatures as low as 50 °C [122]. They have high vapor pressure needed for atomic layer deposition [211, 212]. The ALD of HfO<sub>2</sub> using three different alkylamide precursors (tetrakis(dimethylamido) hafnium (TDMAHf), tetrakis(diethylamido) hafnium (TDEAHf) , and tetrakis(ethylmethylamido)hafnium (TEMAHf)) were studied by Hausmann et al. [155], and found to be self-limiting and to enable low deposition temperatures. Kukli et al. [213, 214] performed an extensive study on the ALD of HfO<sub>2</sub> using TEMAHf and TDMAHf precursors at deposition temperatures above 200 °C. Deshpande et al. [215] used water and TDMAHf at temperatures between 250-350 °C to grow ALD HfO<sub>2</sub>. Ozone and oxygen plasma have been to replace water as the oxidizing agent for the deposition of HfO<sub>2</sub> at T>200 °C [216, 217]. However, there is lack of studies on ALD HfO<sub>2</sub> using alkylamides at low deposition temperatures.

In this chapter, the thermal and plasma-enhanced ALD of HfO<sub>2</sub> using TDMAHf are investigated in the temperature range 50 – 300 °C. The optical constants, chemical composition, roughness, crystallinity, and C-V characteristics

of the thin films are studied. An atomistic model of thermal ALD of HfO<sub>2</sub> is presented using density functional theory approach.

## **6.2 Experimental Procedure and Computational Calculations**

The details of experimental procedure can be found in Chapter 3 and 5. GAUSSIAN 09 [100] was used to perform molecular orbital calculations. The geometry of stationary points was located using the B3LYP gradient corrected density functional method [59-62] with 6-31+G(d,p) basis set [161-168] for nonmetallic atoms, and Los Alamos ECP plus DZ (LanL2DZ) for Hf [169-171]. This level of theory has shown reliable results in studying growth mechanisms of ALD HfO<sub>2</sub> using HfCl<sub>4</sub> and alkylamides [134, 218-220]. Frequency calculations were carried out at the same level of theory to identify the nature of the stationary points (local minima and transition states) and to calculate the zero-point energy corrections and the thermal corrections at ALD temperature and pressure. All energies reported are modified by the zero-point energy correction value.

## **6.3 Results**

### **6.3.1 Optical Constants**

The refractive index and extinction coefficient of TALD and PEALD HfO<sub>2</sub> are plotted against deposition temperature and incident photon energy in Figure 6.1. Good agreement between these results and literature values was found [221, 222]. Both *n* and *k* increase with the deposition temperature. As expected, the refractive indices of the films increase with deposition temperatures due to higher density. However, a small decrease in *n* is observed at 350 °C due to decomposition of the

precursor at elevated temperatures. This is discussed further in section 6.3.3, where the chemical composition of the films is presented. The refractive index of the PEALD films show an abrupt variation at deposition temperatures below 100 °C. The refractive index and extinction coefficient remain roughly constant over the deposition temperature range of 100-300 °C. The optical bandgaps of the films deposited using the same ALD system and deposition recipes were discussed by Foroughi [223]. It was found that the optical bandgap of the ALD HfO<sub>2</sub> varies from 5.4 to 5.6 eV depending on the deposition temperature and is slightly lower than bulk values due to presence of impurities.

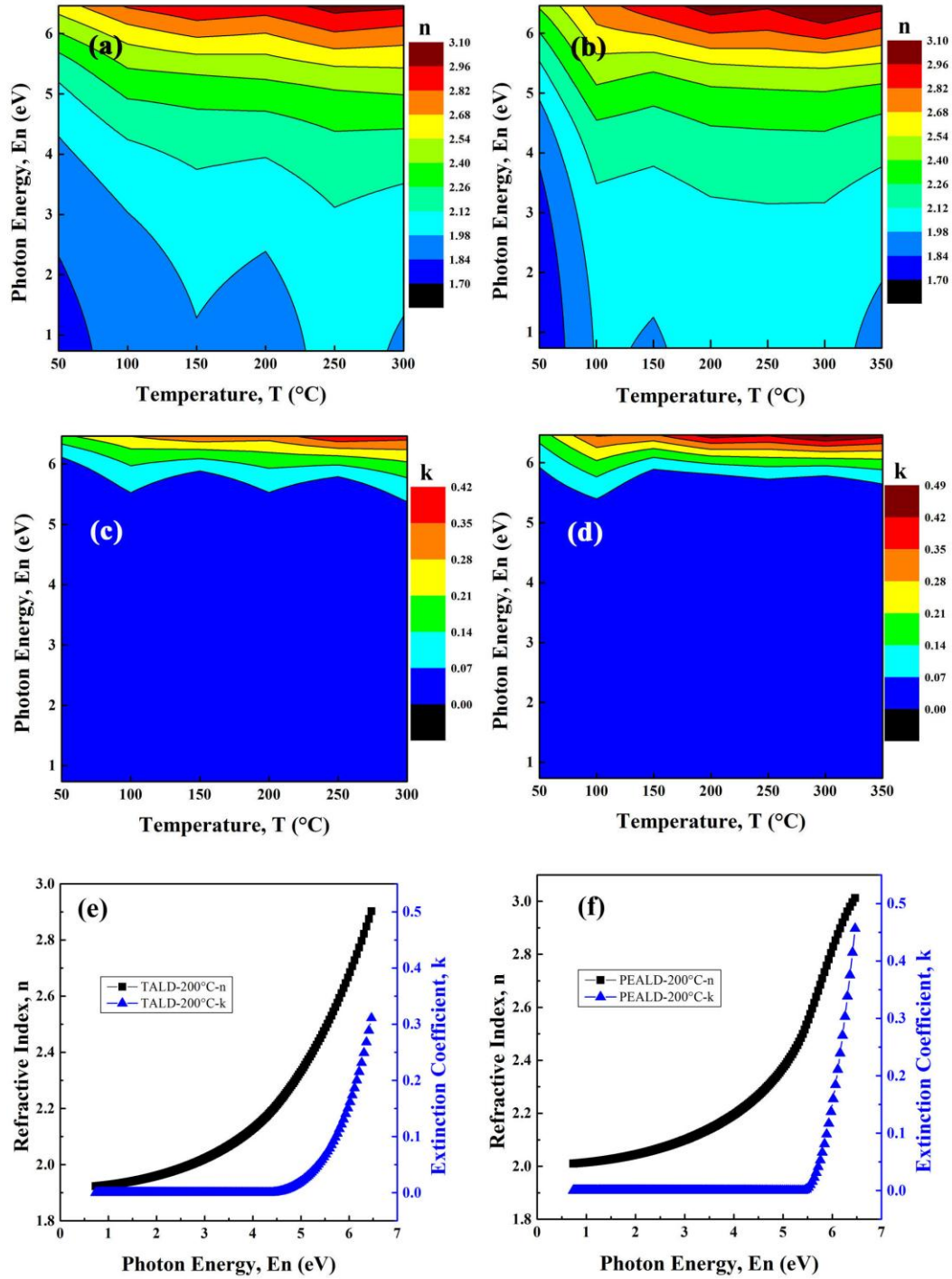


**Figure 6.1** Refractive index (a,b) and extinction coefficient (c,d) of TALD (a,c) and PEALD (b,d) HfO<sub>2</sub> vs. the incident photon energy at various deposition temperatures. For more clarity the refractive index and extinction coefficient of the samples deposited at 200 °C are shown in (e, f).

### 6.3.2 Growth Per Cycle (GPC)

The saturation curves of both the TALD and PEALD HfO<sub>2</sub> thin films deposited in the same deposition system and recipe were discussed elsewhere [223]. It was found that the GPC reaches the saturation points at 0.04 s, 0.50 s, and 2.00 s for TDMAHf, H<sub>2</sub>O, and oxygen plasma exposures, respectively. The GPC of ALD HfO<sub>2</sub> is depicted in Figure 6.2. The high growth rate at low deposition temperature is due to condensation of precursors on the surface. GPC levels off with increasing the deposition temperature. However, a slight increase in GPC is observed for PEALD process at temperatures above 200 °C due to the CVD-like reaction between TDMAHf and molecular O<sub>2</sub>. This behavior is similar to ALD of ZrO<sub>2</sub> (Figure 5.3). Nevertheless, the increase in GPC of HfO<sub>2</sub> PEALD is not as large as that observed for of ZrO<sub>2</sub> because of the higher stability of TDMAHf compared to TDMAZr [155].

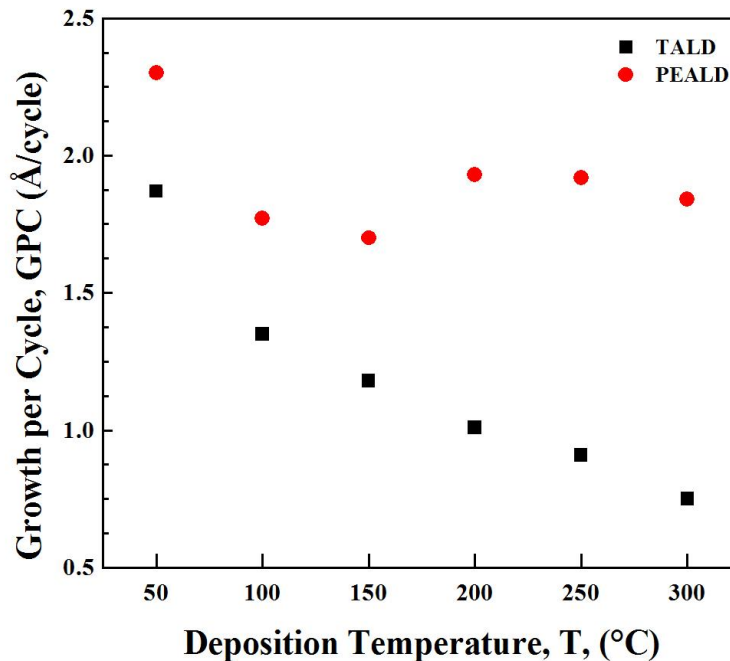
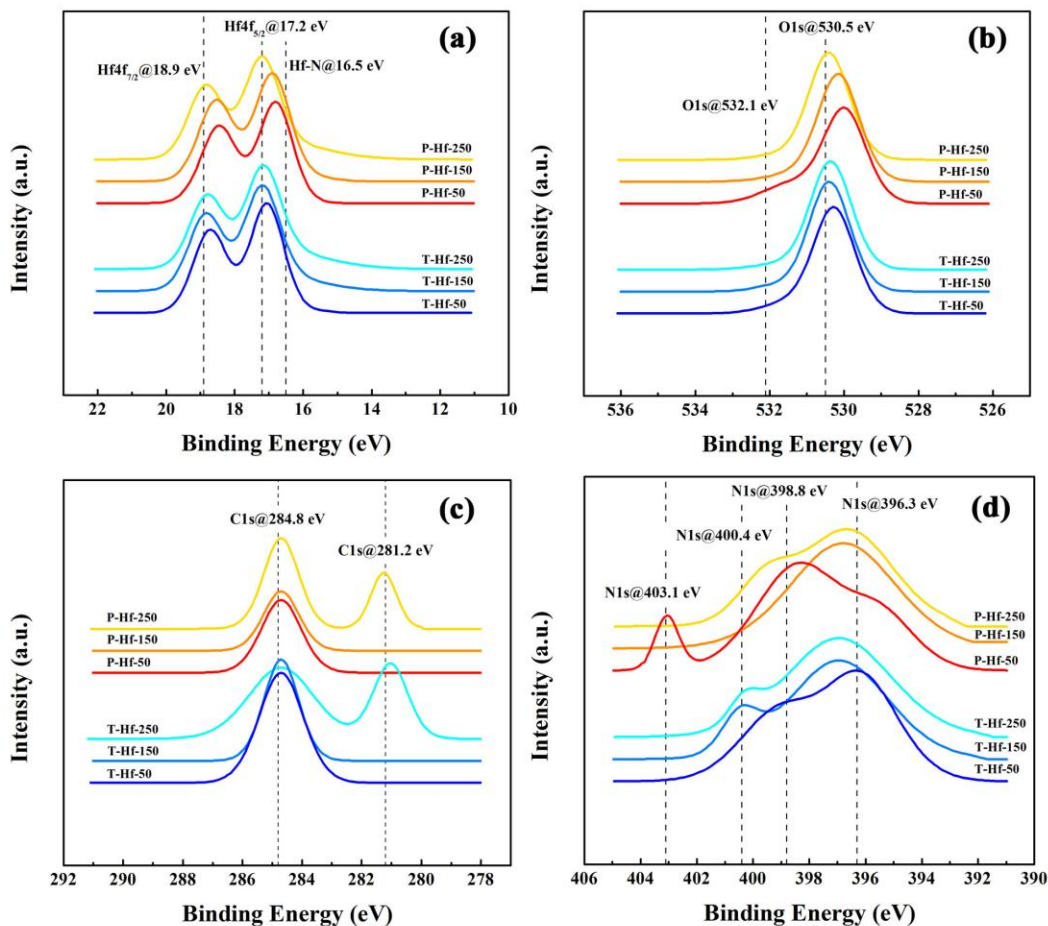


Figure 6.2 Variation of GPC with deposition temperature for TALD and PEALD of HfO<sub>2</sub>.

### 6.3.3 Chemical Composition

High-resolution XPS profiles of Hf, O, C, and N elements are shown in Figure 6.3. Table 6.1 summarizes the binding energies and amount of each element in the films. The Hf profile shows two distinct peaks at binding energies of 17.2 and 18.9 eV attributed to Hf4f<sub>7/2</sub> and Hf4f<sub>5/2</sub> doublets [224-226]. The intensity ratio of these peaks agrees well with 4/3 value of theory. The spin-orbital split value i.e. the difference between the binding energies of Hf4f<sub>7/2</sub> and Hf4f<sub>5/2</sub>, matches the 1.66 eV reported by Kaichev et al. [184]. The ALD films at deposition temperature of 250 °C show another peak at the binding energy of 16.4 eV related to hafnium bonding with nitrogen [225, 227]. The appearance of this peak at higher deposition temperature is an indication of decomposition of the precursor.

The O1s profile depicted in Figure 6.3b, shows the main peak at approximately 530.5 eV. This peak is attributed to Hf-O bond in HfO<sub>2</sub> [225]. The difference between O1s and Hf4f<sub>7/2</sub> binding energies is 513.3 eV and agrees with the reported value for HfO<sub>2</sub> thin films on Si [184]. As shown in Table 6.1, the marginal shifts of O1s and Hf4f peaks to higher binding energies indicate a transition from suboxide to full oxide for HfO<sub>2</sub> with increasing the deposition temperature [228]. This also appears as the higher O/Hf ratio in Table 6.1. However, it is worthy to recall that the preferential etching of O atoms by Ar<sup>+</sup> ions must be considered in treating the results [184]. The other oxygen peak at 532.1 eV can be attributed to the Hf-OH species. The intensity of this peak reduces with increasing deposition temperature, due to desorption of the -OH from the surface in the form of H<sub>2</sub>O.



**Figure 6.3** High-Resolution XPS profiles of Hf4f (a), O1s (b), C1s (c), and N1s for ALD HfO<sub>2</sub> at different deposition conditions.

The C1s binding energy in adsorbed hydrocarbons is defined at 284.8 eV. The amount of the carbon is less than 2.0 at.% in all the samples. At high deposition temperatures a peak appears at 281.3 eV. This peak is ascribed to the Hf-C bond [229]. The nitrogen profile shows a very broad peak, related to different Hf-N. The peaks at higher binding energies, BE > 400eV, can be assigned to NO<sub>2</sub> and NO molecules trapped in the thin films [227]. The peaks at lower binding energies are attributed to the O-Hf-N bond [225]. The amount of nitrogen in the films is less than 3.5 at.% and decreases with the deposition temperature.

**Table 6.1 Chemical compositions of hafnium oxide samples deposited by TALD and PEALD at various temperatures (For each sample the first row shows the binding energy in eV and the second row shows the concentration of the element in at. %)**

| Sample Name | Hf4f <sub>5/2</sub> | Hf4f <sub>7/2</sub> | ΔBE  | I <sub>7/2</sub> -I <sub>5/2</sub> | Hf-N | O1s   | O1s   | O1s   | O/Hf ratio | C1s   | C1s   | N1s |
|-------------|---------------------|---------------------|------|------------------------------------|------|-------|-------|-------|------------|-------|-------|-----|
| T-Hf-50     | 18.7                | 17.1                | 1.67 | 1.3                                | -    | 531.8 | 530.4 | 284.8 | 1.7        | 284.8 | -     | 3.3 |
|             | 14.8                | 19.8                | -    | -                                  | -    | 4.8   | 55.2  | 2.2   | -          | -     | -     | -   |
| T-Hf-150    | 18.8                | 17.2                | 1.64 | 1.3                                | 16.2 | 532.1 | 530.5 | 284.8 | 1.8        | 284.8 | 281.3 | 2.9 |
|             | 13.9                | 18.2                | -    | -                                  | 4.1  | 2.2   | 56.6  | 1.6   | -          | 1.6   | 0.6   | -   |
| T-Hf-250    | 18.8                | 17.2                | 1.65 | 1.3                                | 16.5 | 532.2 | 530.5 | 284.8 | 2.0        | 284.8 | 281.1 | 2.9 |
|             | 12.6                | 16.0                | -    | -                                  | 7.7  | 2.3   | 55.4  | 2.0   | -          | 2.0   | 1.1   | -   |
| P-Hf-50     | 18.5                | 16.8                | 1.66 | 1.3                                | -    | 531.6 | 530.1 | 284.8 | 1.9        | 284.8 | -     | 3.5 |
|             | 14.5                | 18.3                | -    | -                                  | -    | 12.5  | 49.9  | 1.3   | -          | 1.3   | -     | -   |
| P-Hf-150    | 18.6                | 16.9                | 1.66 | 1.3                                | -    | 531.7 | 530.3 | 284.8 | 1.7        | 284.8 | -     | 2.9 |
|             | 15.6                | 20.6                | -    | -                                  | -    | 3.6   | 56.4  | 1.0   | -          | 1.0   | -     | -   |
| P-Hf-250    | 18.9                | 17.2                | 1.64 | 1.3                                | 16.4 | 532.1 | 530.5 | 284.8 | 1.9        | 284.8 | 281.4 | 2.9 |
|             | 13.4                | 17.0                | -    | -                                  | 6.6  | 1.6   | 56.4  | 1.4   | -          | 1.4   | 0.7   | -   |

### 6.3.4 Roughness and Crystallinity

The roughness parameters for HfO<sub>2</sub> thin films are reported in Table 6.2. The AFM images are shown in Figure 6.3. The TALD samples have lower roughness than PEALD. For both the processes, the roughness increases with the deposition temperatures. The AFM images reveal that peaks appear on the surface of the thin films with increasing temperatures. The number, height, and lateral size of these peaks increase with the deposition temperature. At the same deposition temperature, the PEALD process results in rougher surface than of TALD. These peaks can be assigned to the crystallites in the ALD films [122]. The same model discussed for the crystal nucleation and growth in ZrO<sub>2</sub> ALD appears to be valid for HfO<sub>2</sub> as well. However, because of the stronger bonding in HfO<sub>2</sub> (boiling point of 5400 °C) compared to ZrO<sub>2</sub> (4300 °C), crystal nucleation shifts to higher temperatures.

**Table 6.2 RMS Roughness of the TALD and PEALD HfO<sub>2</sub> deposited at various temperatures (nm) (the Si substrate roughness was 0.11 ± 0.02 nm)**

| Deposition Temperature (°C) | TALD        | PEALD       |
|-----------------------------|-------------|-------------|
| 50                          | 0.63 ± 0.06 | 1.41 ± 0.11 |
| 150                         | 0.92 ± 0.09 | 4.32 ± 0.25 |
| 250                         | 1.99 ± 0.12 | 8.69 ± 0.48 |

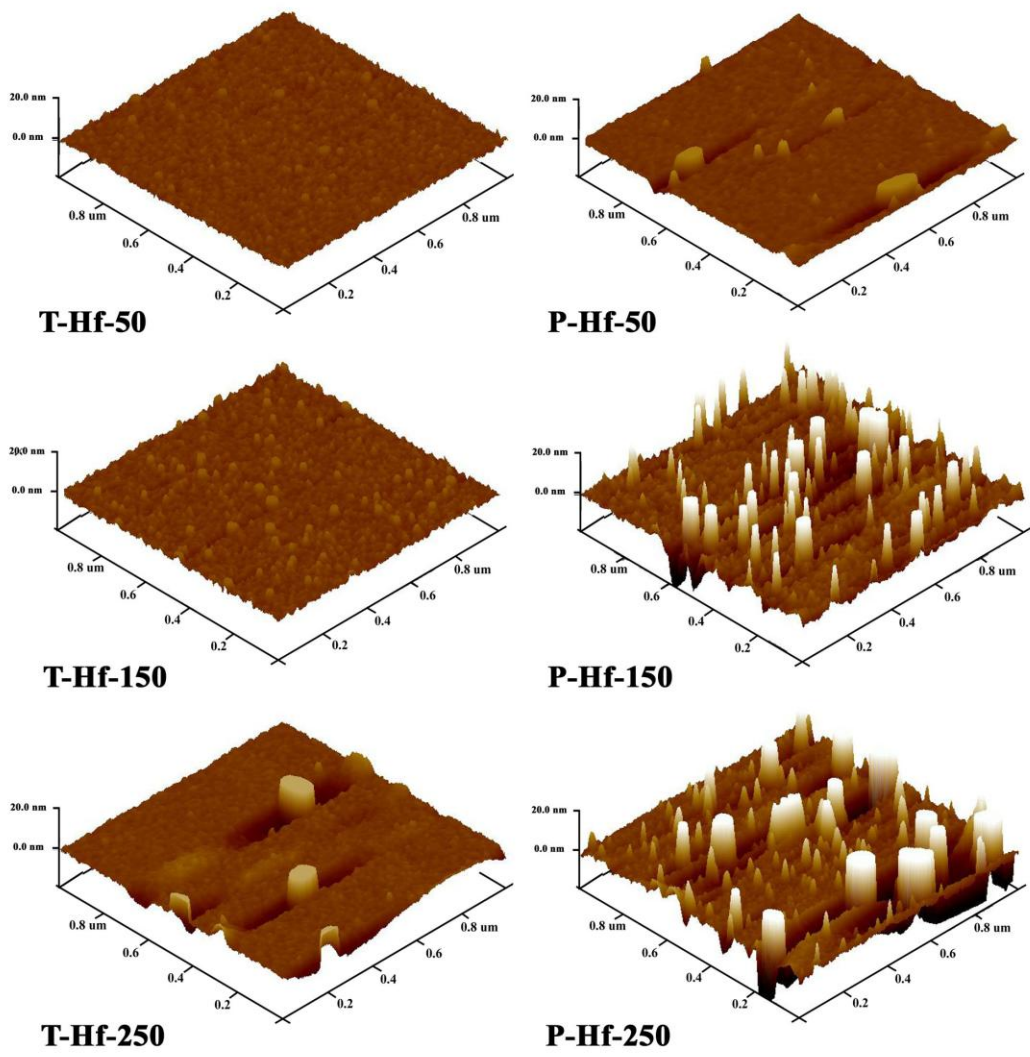


**Figure 6.4 AFM surface plots of the ALD HfO<sub>2</sub> deposited at different temperatures using thermal and plasma-enhanced approaches.**

The XRD results shown in Figure 6.5 agree with the AFM results. The films deposited at low deposition temperature for both TALD and PEALD films shows no peaks attributed to the crystalline phase, which agrees well with AFM results. Two broad peaks at 32.0 and 54.8° can be related to the short-range order. It has been observed that for the very thin films the XRD profiles show no or small peaks [122, 204].

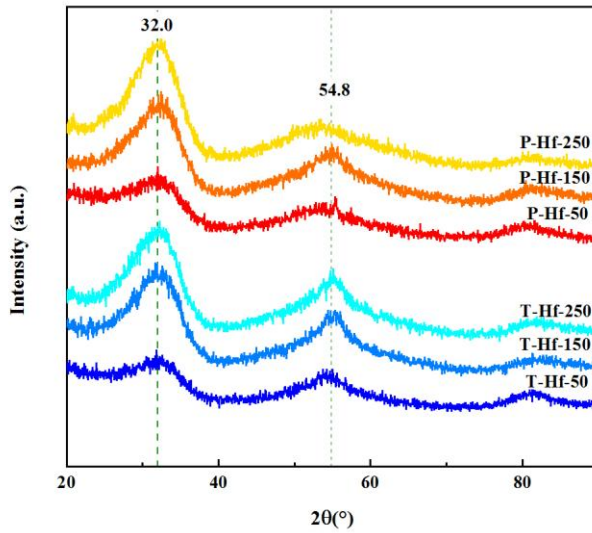


**Figure 6.5 XRD profiles of the ALD HfO<sub>2</sub> samples deposited by thermal and plasma-enhanced ALD processes at different deposition temperatures.**

#### **6.4 Characterization of Cr/HfO<sub>2</sub>/GaN MOS**

A detailed study on the electrical characteristic of Cr/P-Hf-100/GaN MOSCAPs was published elsewhere [230]. The C-V measurements are shown in Figure 6.6 for three different oxide thicknesses. The hysteresis in the C-V measurement of 7.0nm HfO<sub>2</sub> at 20kHz was 100mV. The  $D_{it}=4.6\times 10^{11}eV^{-1}cm^{-2}$  was calculated by applying equation 5.1. This value is approximately one order of magnitude higher than that of ZrO<sub>2</sub>/GaN system. This shows that HfO<sub>2</sub> does not have a good quality interface with GaN possibly due to the presence of N in HfO<sub>2</sub> thin films. It has been shown that nitrogen electron lone pairs act as hole traps at interface [231].

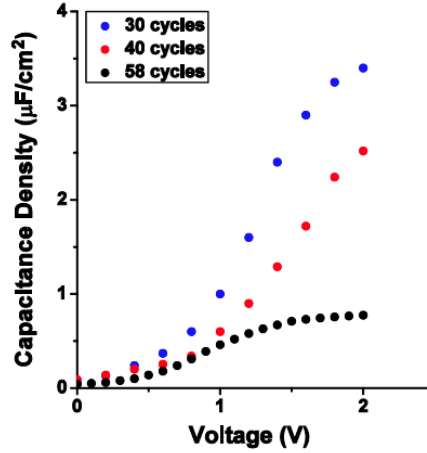


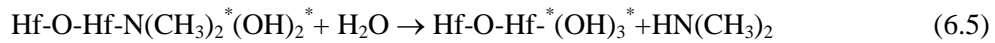
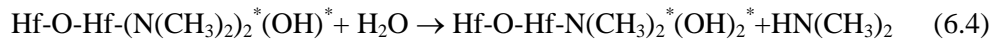
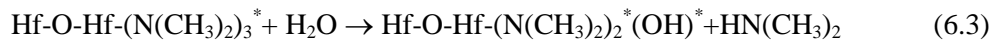
Figure 6.6 C-V characteristics of the Cr/P-Hf-100/GaN MOSCAPs.

## 6.5 Growth Mechanism of TALD HfO<sub>2</sub>: DFT Approach

The HfO<sub>2</sub> growth mechanism is analogous to what was presented for ZrO<sub>2</sub> in Chapter 5 due to the similar chemistry of the precursors. The overall ALD reaction for HfO<sub>2</sub> from TDMAHf and H<sub>2</sub>O is written as following:



where the \* indicates that the specie is on the surface and (g) indicates that the specie is in the gas phase. Reaction 6.1 can be divided into 4 partial reactions, 6.2 to 6.5.



The reaction pathway of reaction 6.2 is depicted in Figure 6.7. The cluster model was used before for growth mechanism of ALD  $\text{HfO}_2$  using  $\text{HfCl}_4$  as the precursor [134]. The  $\text{Hf}_4\text{O}_9\text{H}_3(\text{OH})$  cluster is shown in Figure 6.7. The average Hf-O and Hf-Hf bond lengths are 1.97 and 3.49 Å, respectively. The Hf-O-Hf and O-Hf-O bond angles are 125.3 and 100.5°, respectively. The optimized geometry of TDMAHf is shown in Figure 6.7, 2. For the TDMAHf molecule the calculated bond length and angles are as follows; Hf-N: 2.06 Å, N-C: 1.46 Å, C-H: 1.10 Å, Hf-N-C: 124.2°, N-Hf-N: 109.5°, and C-N-C: 111.6°.

The potential energy surface (PES) of the first partial reaction is shown in Figure 6.8. The reaction begins with adsorption of TDMAHf on the surface, **AS-3**. A hydrogen bond is formed between the H in  $-\text{OH}^*$  and N in TDMAHf. The N-H distance is 1.81 Å and the O-H bond is stretched from 0.96 Å to 1.00 Å. The enthalpy change during the adsorption is 4.4 kcal/mol. The adsorption energy value and the N-H distance are very close to reported values for OH...N hydrogen bond [195]. The transition state geometry calculations was not converged at this level of theory. It is believed that the reaction continues by proton transfer,  $\text{H}^+$ , from  $-\text{OH}^*$  to the N in the transition state, **TS-4**. The post-transition structure is located 28.9 kcal/mol lower than the reactants on the PES. A bond is formed between O on the surface and the Hf with a length of 2.03 Å. In structure, **6**, this bond length reduces to 1.99 Å. The enthalpy change of desorption of  $\text{HN}(\text{CH}_3)_2$  1.9 kcal/mol.

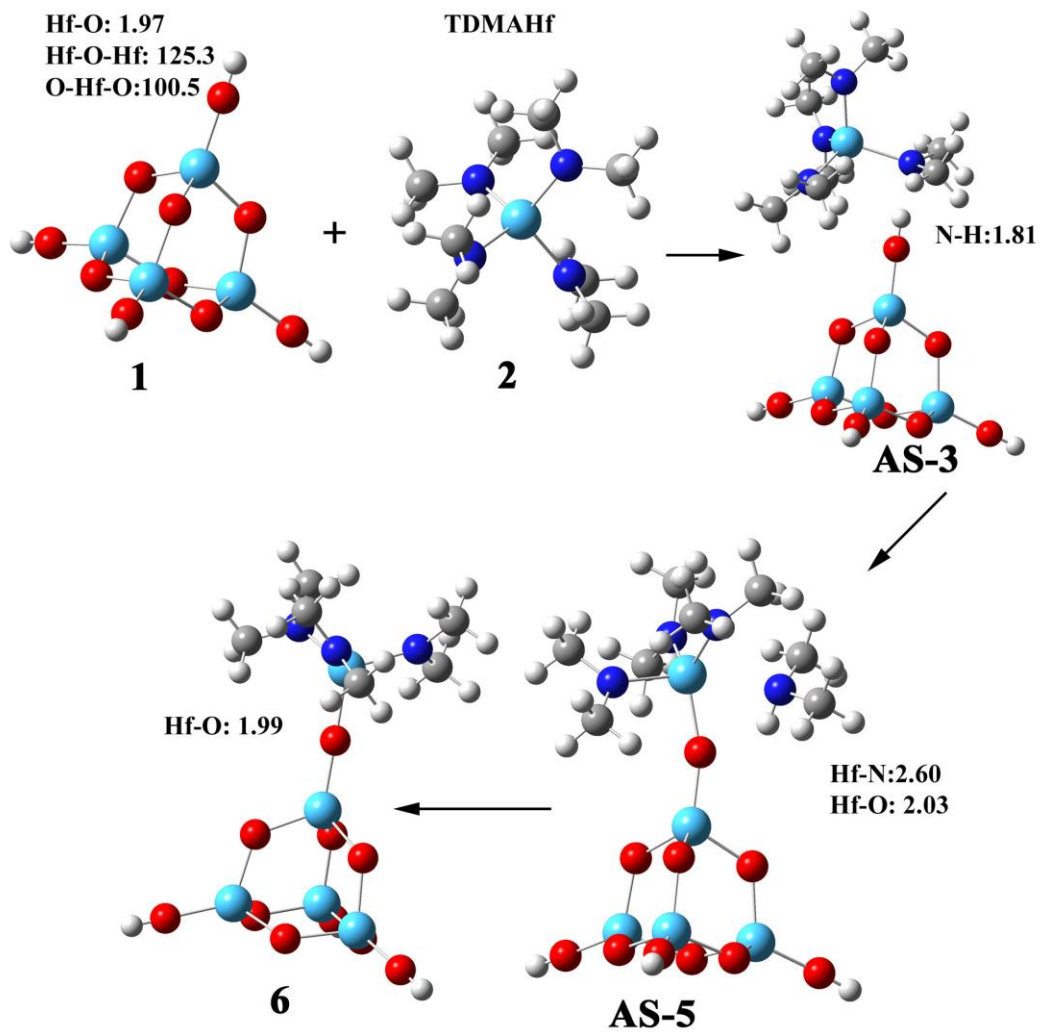
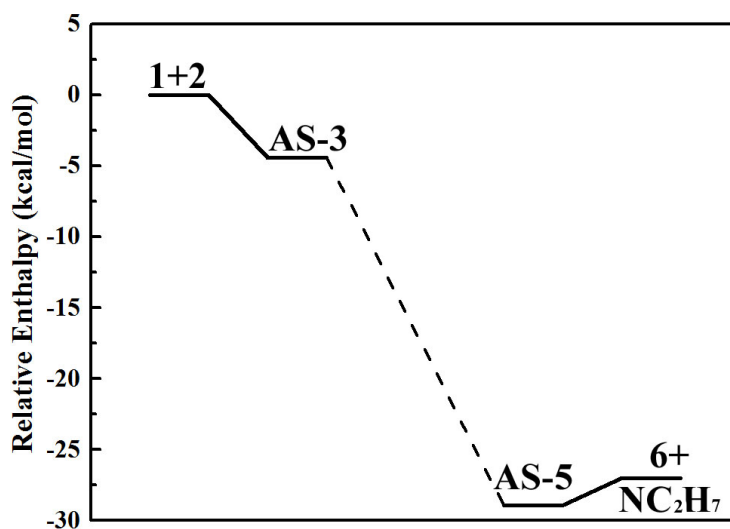


Figure 6.7 Reaction path for first partial reaction of  $\text{HfO}_2$  ALD, involving TDMAHf and  $\text{Hf-OH}^*$  surface reaction sites. The bond lengths are reported in  $\text{\AA}$  and the angles are reported in  $^\circ$ .



**Figure 6.8** PES of the first partial reaction of the ALD HfO<sub>2</sub>, between TDMAHf and –OH surface reaction sites.

The second partial reaction occurs between H<sub>2</sub>O molecules and structure **6**. The reaction pathway is shown in Figure 6.9. The water is adsorbed on the surface via formation of hydrogen bonds between HOH...N(CH<sub>3</sub>)<sub>2</sub>. The enthalpy of adsorption is 1.0 kcal/mol, as shown in Figure 6.10. The reaction continues by formation of a four-center-transition state between Hf-O-N-H atoms, *TS-8*. The transition vector is dominated by the movement of H from water to N to form a HN(CH<sub>3</sub>)<sub>2</sub> molecule. The second partial reaction is barrier-less. The distance between Hf and O becomes much shorter, from 3.99 Å in *AS-7* to 2.34 Å in *TS-8*. The –OH group on the surface points towards the N atom at a distance of 1.77 Å. The newly formed Hf-O bond length is 1.98 Å. The overall enthalpy change for the second partial reaction is -17.6 kcal/mol.

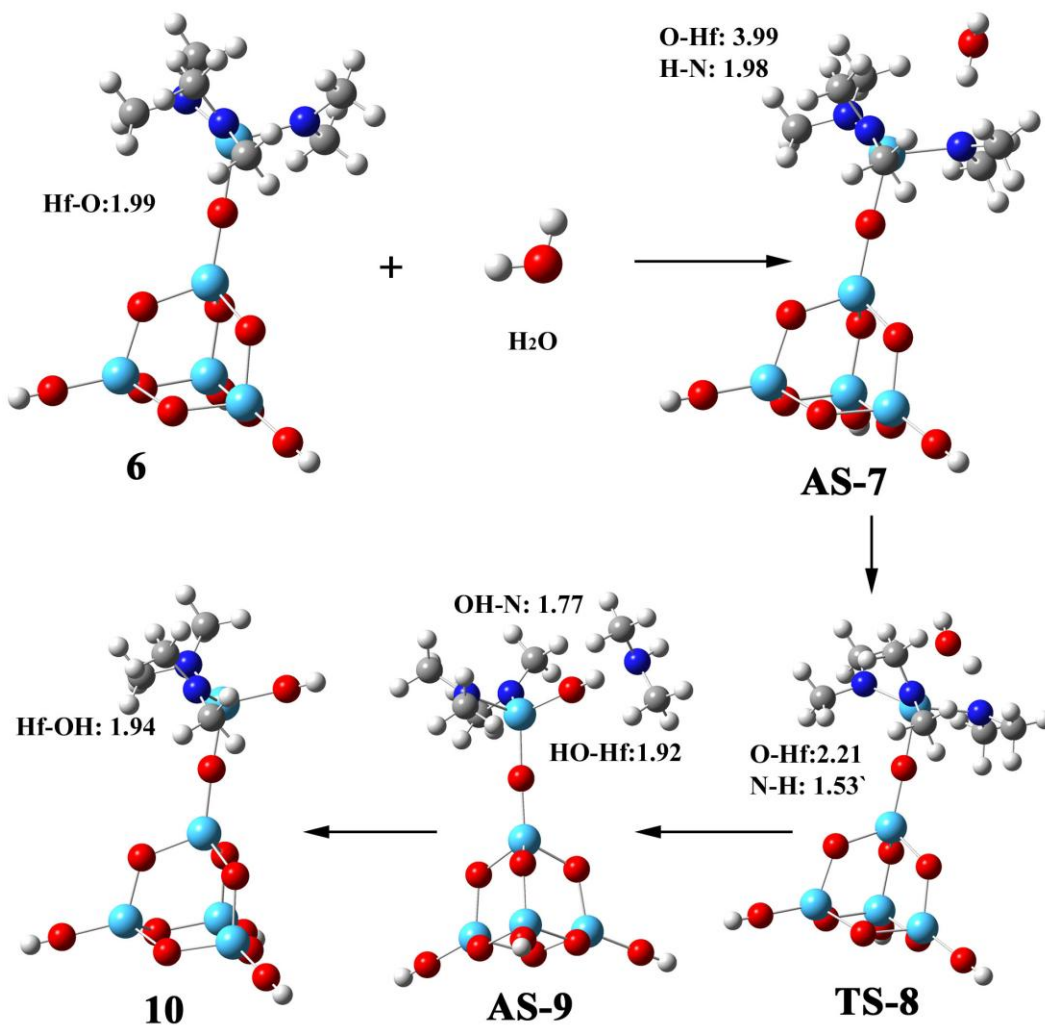


Figure 6.9 Reaction path for second partial reaction of HfO<sub>2</sub> ALD, involving H<sub>2</sub>O and -Hf-(N(CH<sub>3</sub>)<sub>2</sub>)<sub>3</sub>\* surface reaction sites. The bond lengths are reported in Å and the angles are reported in °.

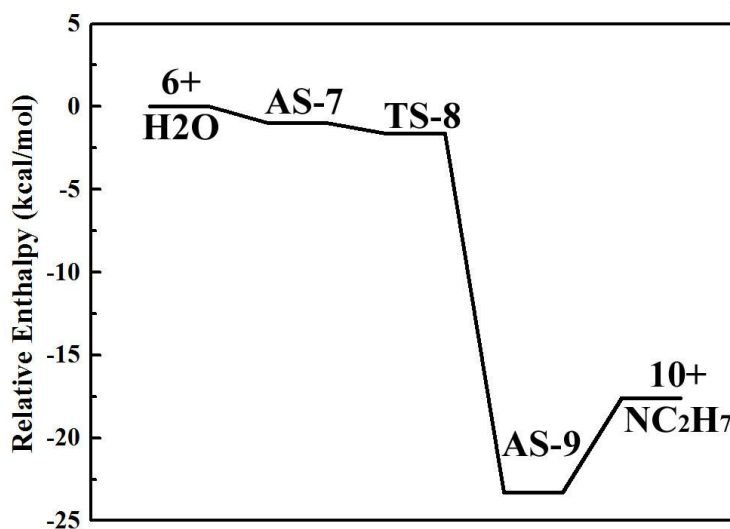


Figure 6.10 PES of the second partial reaction of the ALD  $\text{HfO}_2$ , between  $\text{H}_2\text{O}$  and  $-\text{Hf}-(\text{N}(\text{CH}_3)_2)_3^*$  surface reaction sites.

The reaction path and PES of the third partial reaction are shown in Figures 6.11 and 6.12, respectively. The third partial reaction starts by adsorption of  $\text{H}_2\text{O}$  on the surface, *AS-11*. A hydrogen bond forms between the H in the water molecule and O on the surface. The enthalpy change is  $-5.0$  kcal/mol, which is much higher than the second partial reaction. It seems that another weak hydrogen bond formed between the other H in the water and the one of the N on the surface. The distance between the O in  $\text{H}_2\text{O}$  and Hf on the surface is  $2.43 \text{ \AA}$ . This distance shortens to  $2.30 \text{ \AA}$  in the transition state, *TS-12*. The water molecule rotates and the N-H distance becomes shorter, from  $2.98$  to  $1.46 \text{ \AA}$ . The four-center transition state is formed between N-H-O-Hf and movement of H from water to N dominates the transition vector. The transition state is  $0.9$  kcal/mol above the *AS-11* but is still  $-4.1$  kcal/mol lower than the reactants. The post-transition state, *AS-13*, is located  $24.1$  kcal/mol lower than reactants on the PES. A hydrogen bond is formed between newly formed OH on the surface and  $\text{HN}(\text{CH}_3)_2$  molecule, as the

OH points towards the N at a distance of 1.75 Å. Desorption of the byproduct from the surface is endothermic by a value of 6.4 kcal/mol. However, the total enthalpy change for the third partial reaction is -17.7 kcal/mol. The Hf-O bond length is 1.97 in the byproduct on the surface, **14**.

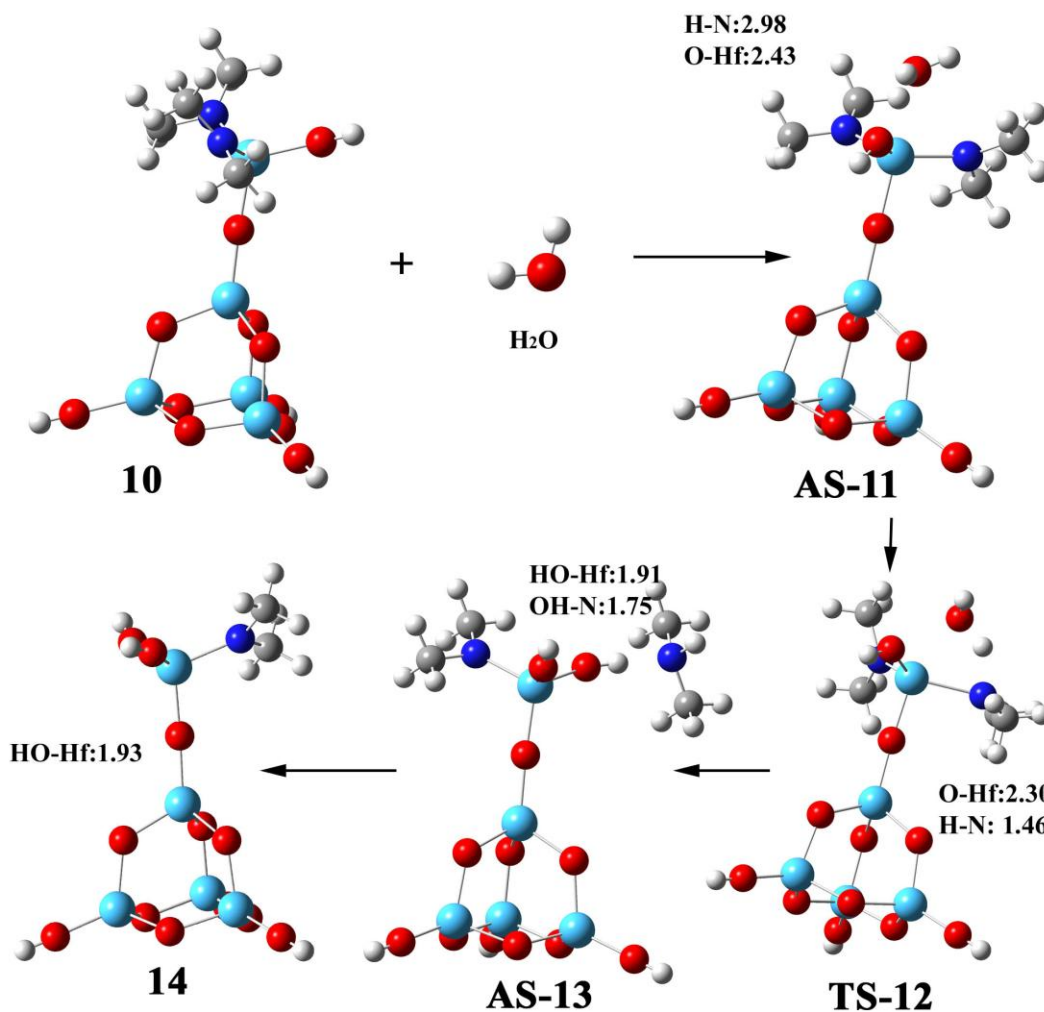


Figure 6.11 Reaction path for third partial reaction of HfO<sub>2</sub> ALD, involving H<sub>2</sub>O and -Hf(OH)-(N(CH<sub>3</sub>)<sub>2</sub>)<sub>2</sub>\* surface reaction sites. The bond lengths are reported in Å and the angles are reported in °.

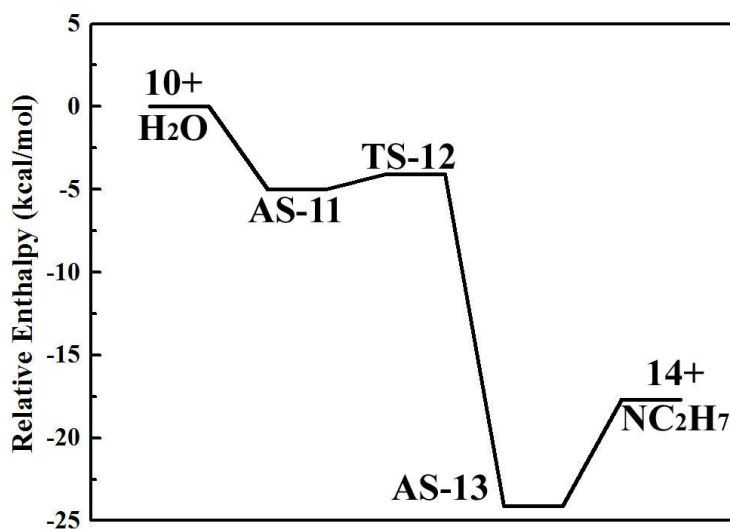


Figure 6.12 PES of the third partial reaction of the ALD HfO<sub>2</sub>, between H<sub>2</sub>O and -Hf-(N(CH<sub>3</sub>)<sub>2</sub>)<sub>2</sub>\* surface reaction sites.

The final partial reaction is very similar to the third one. The reaction pathway and the corresponding PES are shown in Figures 6.13 and 6.14. The distances and bond length are shown in Figure 6.13. The adsorption energy of water on the surface is -6.9 kcal/mol, *AS-15*. The transition state, *TS-16*, locates 3.9 kcal/mol above the *AS-15*. The reaction mechanism is the proton transfer from water to N to form a HN(CH<sub>3</sub>)<sub>2</sub>. The post transition state, *AS-17*, is located -24.2 kcal/mol lower than reactants. The overall reaction is exothermic by a value of 17.8 kcal/mol, as seen in Figure 6.14. The Hf-O distance in the final state, *18*, is 1.96 Å.

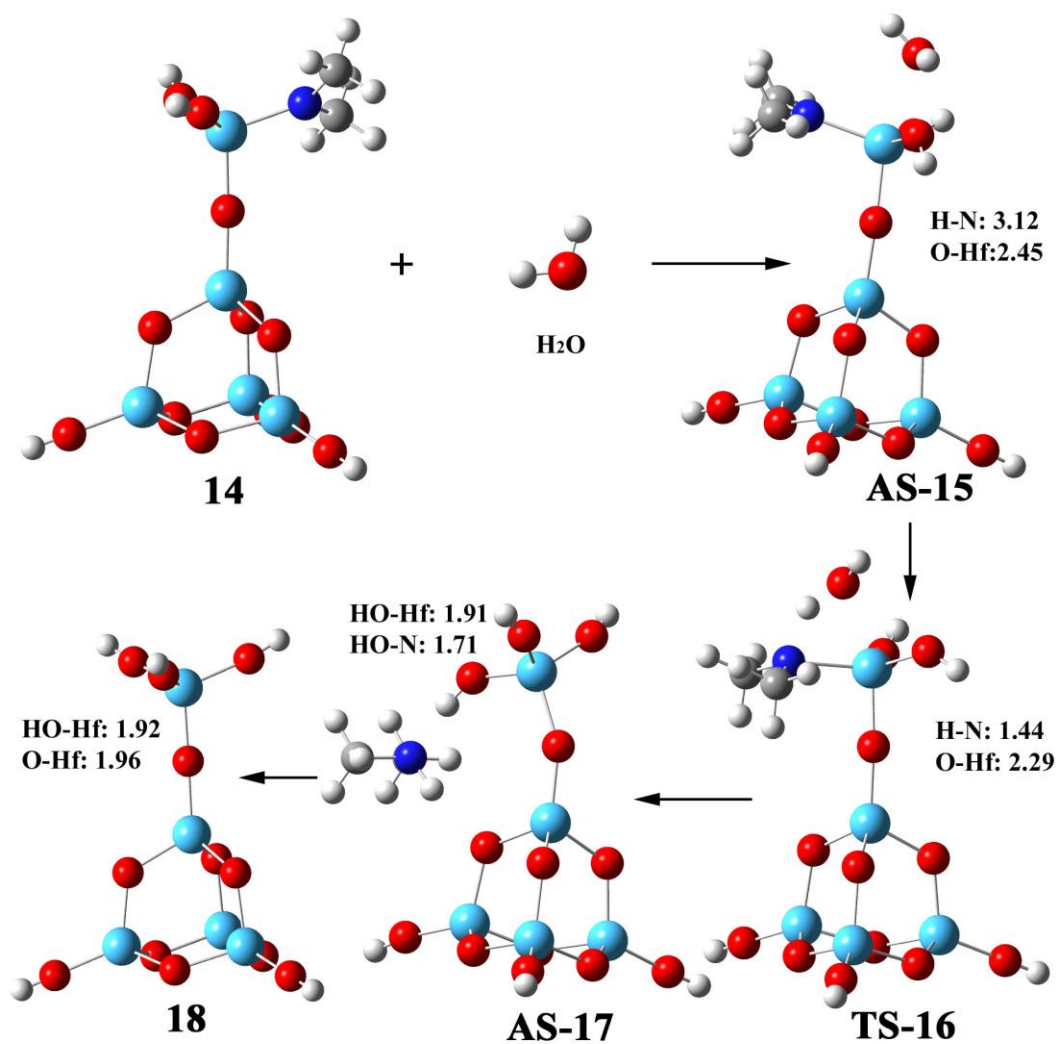
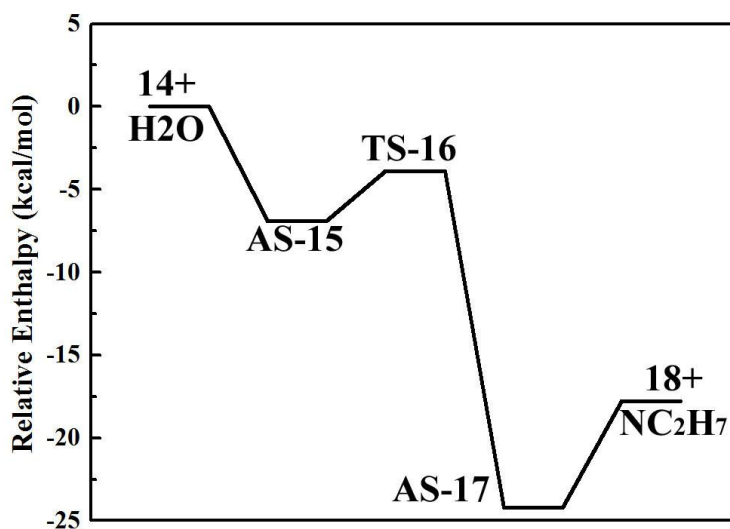


Figure 6.13 Reaction path for fourth partial reaction of HfO<sub>2</sub> ALD, involving H<sub>2</sub>O and –Hf(OH)<sub>2</sub>-N(CH<sub>3</sub>)<sub>2</sub>\* surface reaction sites. The bond lengths are reported in Å and the angles are reported in °.



**Figure 6.14** PES of the fourth partial reaction of the ALD HfO<sub>2</sub>, between H<sub>2</sub>O and –Hf(OH)<sub>2</sub>-N(CH<sub>3</sub>)<sub>2</sub>\* surface reaction sites.

Similar to the ALD of ZrO<sub>2</sub>, it is concluded that all the ALD half-reactions involve formation of intermediate complexes. These complexes form between TDMAHf and Hf-OH\* in the 1st half-reaction, AS-3, and between H<sub>2</sub>O and surface reaction site in 2<sup>nd</sup> to 4<sup>th</sup> half-reactions, AS-7, AS-11, and AS-17. The variations of the Gibbs free energy of formation of these complexes with temperature are shown in Figure 6.15 along with GPC of ALD HfO<sub>2</sub>. The calculated Gibbs free energies of formation of the surface complexes at the ALD chamber pressure, 1.0 torr, are positive at all the deposition temperatures. This justifies to the dependence of GPC on deposition temperature. The decrease of GPC with deposition temperature is consistent with the DFT results. It must be mentioned that here we have not considered the possibility of the reaction of TDMAHf with two –OH\* groups on the surface simultaneously. This mechanism could also affect the growth mechanism and growth rate of the ALD oxide and it should be considered in future work.

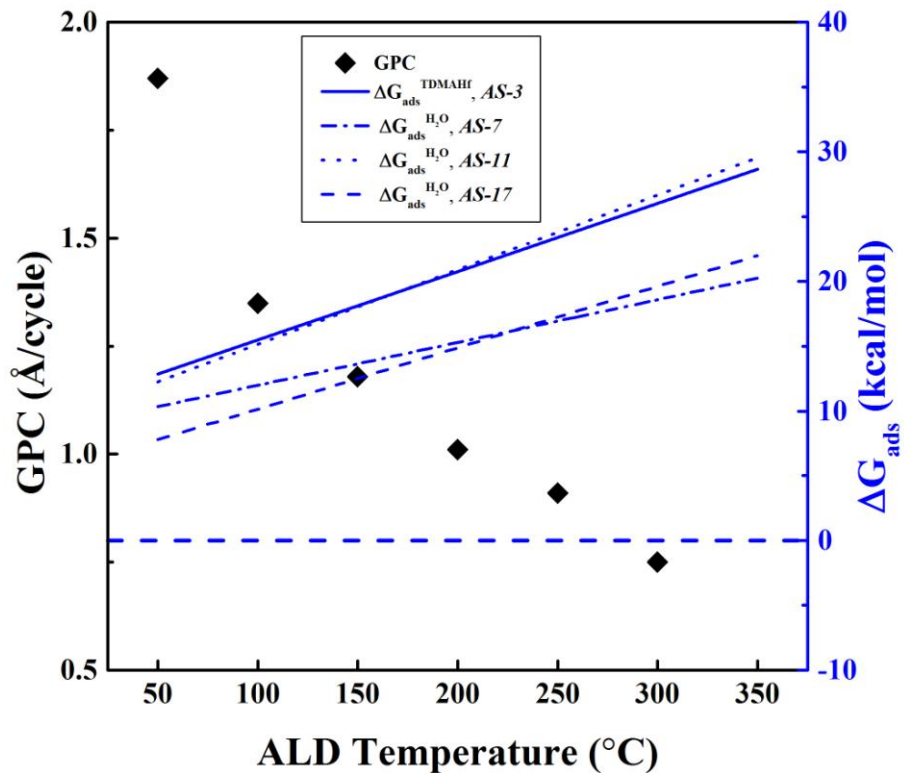


Figure 6.15 Temperature-dependent variation of GPC, and Gibbs free energies of adsorption of TDMAHf and H<sub>2</sub>O during ALD of HfO<sub>2</sub>.

## 6.6 Conclusions

The growth mechanisms of thermal and plasma-enhanced ALD HfO<sub>2</sub> were investigated. The dependence of GPC on deposition temperature showed the condensation of TDMAHf molecules on the surface at low temperatures. CVD-like reaction of TDMAHf and O<sub>2</sub> was observed for PEALD process at high temperatures. The optical constants of the ALD films were calculated by fitting the spectroscopic ellipsometry data to a Tauc-Lorentz model and agreed with the bulk values. AFM and XRD studies indicated the formation of crystallite in amorphous films, which matched the nucleation and growth mechanisms

proposed for ALD of  $\text{ZrO}_2$ . The density of interface trap states was shown to be an order of magnitude higher than that of  $\text{ZrO}_2/\text{GaN}$  interface. This can be attributed to the presence of N impurities in the  $\text{HfO}_2$  thin films. However, the amount of C in the samples was less than 3.0 at.% depending on the deposition temperature. A DFT approach to the growth mechanism of TALD  $\text{HfO}_2$  was represented. It was observed that the enthalpy changes and reaction pathways are very similar to ALD of  $\text{ZrO}_2$  due to the similar chemistry of the precursors.

## Chapter 7

---

### **Conclusions and Future Work**

The purpose of this thesis is an in-depth study of growth mechanisms of the atomic layer deposition (ALD) of three important oxides with promising applications in the wide bandgap semiconductor industry, i.e. ZnO, ZrO<sub>2</sub> and HfO<sub>2</sub>. The oxides were deposited with both thermal and plasma-enhanced ALD approaches in the deposition temperature range from 50 - 300 °C. Characterization techniques used included spectroscopic ellipsometry (SE), X-ray photoelectron spectroscopy (XPS), atomic force microscopy (AFM), and X-ray diffraction (XRD) to methodically study the material properties of the oxides. A model for the nucleation and growth of the crystalline phase was proposed. Finally, a detailed quantum chemistry approach based on density functional theory was utilized to model the growth mechanism of the TALD oxides.

ZnO, with a bandgap of about 3.4 eV, has found many applications in thin-film transistors (TFT) and is a promising low cost replacement for GaN in some electronic and optical applications. ZrO<sub>2</sub> and HfO<sub>2</sub> are two promising high- $\kappa$  oxides for gate oxide on III-V metal-oxide-semiconductor field-effect transistors (MOSFETs). ALD ZrO<sub>2</sub> and HfO<sub>2</sub> are currently used in fabrication of dynamic random-access memories (DRAMs) and central processing units (CPUs). Despite of the vast literature on the deposition, characterization, and application of these three oxides, there is lack of an in-depth study on the growth mechanisms and the materials characterization. The setup of the ALD chamber, carrier gas, chemistry

of precursors, deposition temperature, substrate material, and dose and purge times can affect the properties of the oxides. In this thesis, the effect of deposition temperature and the ALD process on the material properties of the TALD and PEALD oxides was studied by keeping all the other parameters constant.

Diethylzinc (DEZ), tetrakis(dimethylamido)zirconium (TDMAZr), and tetrakis(dimethylamido)hafnium (TDMAHf) were used as the metal precursors for ALD of ZnO, ZrO<sub>2</sub>, and HfO<sub>2</sub>, respectively. H<sub>2</sub>O and remote oxygen plasma were used as the oxidizing reagent for TALD and PEALD processes. The saturation curves were studied to find the optimum dose times for the precursors. It was found that the optimum values for the exposure time of DEZ, TDMAZr, TDMAHf, H<sub>2</sub>O, and O<sub>2</sub>-plasma are 0.02, 0.04, 0.04, 0.10, and 2.00s, respectively. The optical constants and optical bandgaps of the ALD films were found by fitting the SE data to the appropriate optical models and were found to agree with the bulk values at deposition temperatures over 100 °C. The growth-per-cycles (GPCs) of the ALD films were calculated by fitting the *in-Situ* spectroscopic ellipsometry data to the optical models.

GPC of ZnO reached the maximum value at ~150 °C. For the TALD ZrO<sub>2</sub> and HfO<sub>2</sub> oxide the GPCs decrease with deposition temperature. The DFT models showed that the Gibbs free energy of the adsorption of the precursors changed sign at about the same temperature. It was found that the Gibbs free energy of adsorption of TDMAZr and TDMAHf are slightly positive at all the deposition temperatures. Based on these results, it was showed that the thermodynamic

stability of the intermediate structures has the most influence on the GPC of the ALD oxides.

The AFM studies showed that the roughness of the ZnO thin films decrease with the deposition temperature. XRD results showed formation of preferential crystal orientation of the films with increasing deposition temperatures. The chemical composition of the samples from XPS experiment showed a relatively high concentration of Zn(OH) at low deposition temperatures. It is believed that –OH groups deteriorate surface diffusion. Based on these results, a model was proposed for the nucleation and growth of ALD ZnO. It was showed that –OH groups on the surface and the grain boundaries have an important effect on the crystallographic orientation of the ZnO films. XPS results also revealed that the amount of carbon in the films were less than 4 at.% for all the deposition temperatures. The main source of the carbon seemed to be the decomposition of DEZ, especially at high deposition temperatures. The electrical resistivity of the ALD films showed a drop at about 130 °C, possibly because of variation of zinc vacancy and hydrogen concentration in the films. However, more study is needed to find the exact source of this phenomenon.

An increase in GPCs of PEALD ZrO<sub>2</sub> and HfO<sub>2</sub> were observed due to gas phase reaction of metal precursors and O<sub>2</sub> molecules. The optical constants of the ALD films were calculated by fitting the spectroscopy ellipsometric data to a Tauc-Lorentz model and were found very close to the bulk values at all deposition temperatures. The AFM studies showed that the roughness of the ZrO<sub>2</sub> and HfO<sub>2</sub> thin films increase with the deposition temperature due to formation of crystallites.

The crystallite nucleation temperature shifted to lower temperature in PEALD process. The  $\text{ZrO}_2$  showed to have cubic phase at high deposition temperatures. The XRD patterns of  $\text{HfO}_2$  films did not reveal the crystalline nature of the films. Based on these results, a model for the growth of ALD  $\text{ZrO}_2$  and  $\text{HfO}_2$  films was proposed. The chemical compositions of the thin films were studied with XPS. For ALD  $\text{ZrO}_2$ , the amount of C in the samples varied from 2.0 to 9.8 at.% depending on the deposition temperature. The PEALD contained higher amount of carbon due to decomposition of TDMAZr. It was found that ALD  $\text{ZrO}_2$  was free from any N contamination. However, for ALD  $\text{HfO}_2$ , the chemical compositions of the thin films were shown presence of N in the films. The amount of C in the samples was less than 3.0 at.% depending on the deposition temperature. The oxygen/metal ratios of the films were less than 2, probably due to preferential etching of oxygen atoms during cleaning of the samples with  $\text{Ar}^+$  prior to the XPS experiment.

C-V measurements on Cr/ $\text{ZrO}_2$ /GaN metal-oxide-semiconductor capacitors (MOSCAPs) showed that the density of interface trap states was shown to be less than  $10^{11} \text{ eV}^{-1}\text{cm}^{-2}$ . The density of interface trap states was shown to be an order of magnitude higher in Cr/ $\text{HfO}_2$ /GaN MOSCAPs. The TEM images revealed a well-defined interface for  $\text{ZrO}_2$ /GaN interface.

## 7.1 Summary of Contributions to Knowledge

- Nucleation and growth mechanisms were proposed for thermal and plasma enhanced ALD of  $\text{ZnO}$ ,  $\text{ZrO}_2$ , and  $\text{HfO}_2$  based on the AFM, XRD, and

XPS results. The ALD growth of these oxides was studied as a function of deposition variables.

- The optical constants maps of the ZnO, ZrO<sub>2</sub>, and HfO<sub>2</sub> vs. deposition temperature and photon energy were obtained. The graphs can be used to construct optical models of the ALD oxides for *in-situ* and *ex-situ* spectroscopy measurements.
- Atomistic growth mechanisms of thermal ALD ZnO, ZrO<sub>2</sub>, and HfO<sub>2</sub> were studied using density functional theory approach. The important role of formation of intermediate structures between surface and the precursor molecules were highlighted. The results found to be consistent with the variation of GPC of the ALD oxides with deposition temperature.
- We were able to develop a ZrO<sub>2</sub>/GaN interface with a very low density of interface traps, which enables the fabrication of the GaN MOSFETs for high-power and high-frequency applications.

## 7.2 Future Work

In this thesis, the dose and purge times were set to the optimal values from the GPC point of view. However, as discussed in Chapter 4, dose and purge durations can affect chemical composition, microstructure, and electrical properties of the ALD oxides. A systematic approach to the effect of exposure time and purge duration would be of interest. The role of hydrogen concentration on the electrical characteristics of ZnO seemed to be crucial. However, XPS is not able to detect hydrogen atoms. Rutherford backscattering spectroscopy (RBS) can be utilized to detect hydrogen content of the ALD films.

We found DFT results valuable in understanding the behavior of the GPC of the thermal ALD oxides with deposition temperature. The reaction of the precursors with molecular oxygen, atomic oxygen, and oxygen radicals could be used to understand the growth mechanisms of PEALD oxides better. The thermodynamics of the gas phase reaction between the precursors and O<sub>2</sub> can help the understanding of the high GPC of ZrO<sub>2</sub> and HfO<sub>2</sub> at high deposition temperatures. Meanwhile, increasing the accuracy of SE and reducing the sampling time would result in accurately determining the activation energies of the surface reactions and the results could be compared to the theoretical calculations. Utilizing a mass spectrometer to analyze the chemistry of the species in the chamber in real-time, along with the ellipsometer would be an asset.

In this thesis, we only studied the C-V characteristic of the ZrO<sub>2</sub> and HfO<sub>2</sub> thin films deposited at 100 °C using PEALD process. Studying the interface trap density of the MOSCAP using the ALD oxides at other deposition temperatures can be helpful in understanding the relationship between the structure and chemistry of the samples and the electrical characteristics of the oxides. DFT again could be employed to better understand the involving mechanisms of formation of interface traps at GaN/ALD-oxides interface.

## Bibliography

1. Özgür, U., Alivov, Y.I., Liu, C., Teke, A., Reshchikov, M.A., Doğan, S., Avrutin, V., Cho, S.J., and Morkoç, H., "A *Comprehensive Review of ZnO Materials and Devices*". Journal of Applied Physics, **2005**. 98(4): p. 041301.
2. Johnson, W.C., Parsons, J.B., and Crew, M.C., "*Nitrogen Compounds of Gallium III Gallic Nitride*". Journal of Physical Chemistry, **1932**. 36(7): p. 2651-2654.
3. Juza, V.R. and Hahn, H., "*Über Die Kristallstrukturen Von Cu<sub>3</sub>N, GaN Und InN Metallamide Und Metallnitride*". Zeitschrift für anorganische und allgemeine Chemie, **1938**. 239: p. 282 - 287.
4. Grimmeiss, H.G. and Koelmans, H., "*Über Die Kantenemission Und Andere Emissionen Des GaN*". Zeitschrift Für Naturforschung Part a-Astrophysik Physik Und Physikalische Chemie, **1959**. 14(3): p. 264-271.
5. Maruska, H.P. and Tietjen, J.J., "*The Prepration and Properties of Vapor-Deposited Single-Crystalline GaN*". Applied Physics Letters, **1969**. 15: p. 327 - 329.
6. Pankove, J.I., "*Prespective on Gallium Nitride*". Materials Research Society Samposium Proceedings, **1990**. 162: p. 515 - 524.
7. Pearton, S.J., Ren, F., Zhang, A.P., Dang, G., Cao, X.A., Lee, K.P., Cho, H., Gila, B.P., Johnson, J.W., Monier, C., Abernathy, C.R., Han, J., Baca, A.G., Chyi, J.I., Lee, C.M., Nee, T.E., Chuo, C.C., and Chu, S.N.G., "*GaN Electronics for High Power, High Temperature Applications*". Materials Science and Engineering B, **2001**. 82(1-3): p. 227-231.
8. Simin, G., Asif Khan, M., Shur, M.S., and Gaska, R., "*Insulated Gate III-N Heterostructure Field-Effect Transistors*". International Journal of High Speed Electronics and Systems, **2004**. 14: p. 197 - 224.
9. Phillips, J.C., "*Bonds and Bands in Semiconductors*". **1973**, New York: Academic Press.
10. Takahashi, K., Yoshikawa, A., and Sandhu, A., eds. *Wide Bandgap Semiconductors: Fundamental, Properties, and Modern Photonic and Electronic Devices*. **2007**, Springer: Berlin.

11. Morkoc, H., "*Nitride Semiconductors and Devices*. **1999**, Berlin: Springer.
12. Romyantsev, S.L. and Shur, M.S., "*Materials Properties of Nitrides. Summary*". International Journal of High Speed Electronics and Systems, **2004**. 14: p. 1-19.
13. Zhang, A.P., Ren, F., Anderson, T.J., Abernathy, C.R., Singh, R.K., Holloway, P.H., Pearton, S.J., and Palmer, D., "*High-Power GaN Electronic Devices*". Critical Reviews in Solid State and Materials Sciences, **2002**. 27(1): p. 1-71.
14. Buniatyan, V.V. and Aroutiounian, V.M., "*Wide Gap Semiconductor Microwave Devices*". Journal of Physics D-Applied Physics, **2007**. 40(20): p. 6355-6385.
15. Balachander, K., Arulkumaran, S., Ishikawa, H., Baskar, K., and Egawal, T., "*Studies on Electron Beam Evaporated ZrO<sub>2</sub>/AlGa<sub>N</sub>/Ga<sub>N</sub> Metal-Oxide-Semiconductor High-Electron-Mobility Transistors*". Physica Status Solidi a-Applied Research, **2005**. 202(2): p. R16-R18.
16. Gila, B.P., Hlad, M., Anderson, T., Chen, J.-J., Allums, K.K., Gerger, A., Herrero, A., Jang, S., Kang, B., Abernathy, C.R., Ren, F., and Pearton, S.J. "*Oxide Dielectrics for Reliable Passivation of AlGa<sub>N</sub>-Ga<sub>N</sub> HEMTs and Insulated Gates*". in ECS Transactions. **2006**.
17. Liu, C., Chor, E.F., and Tan, L.S., "*Investigations of HfO<sub>2</sub>/AlGa<sub>N</sub>/Ga<sub>N</sub> Metal-Oxide-Semiconductor High Electron Mobility Transistors*". Applied Physics Letters, **2006**. 88(17): p. 173504.
18. Liu, Z.H., Ng, G.I., Arulkumaran, S., Maung, Y.K.T., Teo, K.L., Foo, S.C., and Sahnuganathan, V., "*Improved Two-Dimensional Electron Gas Transport Characteristics in AlGa<sub>N</sub>/Ga<sub>N</sub> Metal-Insulator-Semiconductor High Electron Mobility Transistor with Atomic Layer-Deposited Al<sub>2</sub>O<sub>3</sub> as Gate Insulator*". Applied Physics Letters, **2009**. 95(22): p. 223501.
19. Sugiura, S., Hayashi, Y., Kishimoto, S., Mizutani, T., Kuroda, M., Ueda, T., and Tanaka, T., "*Fabrication of Normally-Off Mode Ga<sub>N</sub> and AlGa<sub>N</sub>/Ga<sub>N</sub> Mosfets with HfO<sub>2</sub> Gate Insulator*". Solid-State Electronics, **2010**. 54(1): p. 79-83.
20. Sun, X., Saadat, O.I., Chang-Liao, K.S., Palacios, T., Cui, S., and Ma, T.P., "*Study of Gate Oxide Traps in HfO<sub>2</sub>/AlGa<sub>N</sub>/Ga<sub>N</sub> Metal-Oxide-Semiconductor High-Electron-Mobility Transistors by Use of AC Transconductance Method*". Applied Physics Letters, **2013**. 102(10): p. 103504.

21. Schroder, D.K., "*Semiconductor Material and Device Characterization*. **1990**, The United States of America: Wiley-Interscience Publication.
22. Wheeler, V.D., *Structure and Properties of Epitaxial Dielectrics on GaN*, in *Material Science and Engineering*, **2009**, North Carolina State University: Raleigh.
23. Chang, Y.C., Chang, W.H., Chiu, H.C., Tung, L.T., Lee, C.H., Shiu, K.H., Hong, M., Kwo, J., Hong, J.M., and Tsai, C.C., "*Inversion-Channel GaN Metal-Oxide-Semiconductor Field-Effect Transistor with Atomic-Layer-Deposited Al<sub>2</sub>O<sub>3</sub> as Gate Dielectric*". *Applied Physics Letters*, **2008**. 93(5): p. 053504.
24. Chen, J.J., Gila, B.P., Hlad, M., Gerger, A., Ren, F., Abernathy, C.R., and Pearton, S.J., "*Band Offsets in the Sc<sub>2</sub>O<sub>3</sub>/GaN Heterojunction System*". *Applied Physics Letters*, **2006**. 88(14): p. 142115.
25. Gregusova, D., Stoklas, R., Cico, K., Lalinsky, T., and Kordos, P., "*AlGaIn/GaN Metal-Oxide-Semiconductor Heterostructure Field-Effect Transistors with 4 nm Thick Al<sub>2</sub>O<sub>3</sub> Gate Oxide*". *Semiconductor Science and Technology*, **2007**. 22(8): p. 947-951.
26. Therrien, R., Lucovsky, G., and Davis, R.F., "*Charge Redistribution at GaN-Ga<sub>2</sub>O<sub>3</sub> Interfaces: A Microscopic Mechanism for Low Defect Density Interfaces in Remote Plasma Processed MOS Devices Prepared on Polar GaN Faces*". *Physica Status Solidi a-Applied Research*, **1999**. 176(1): p. 793-796.
27. Robertson, J. and Falabretti, B., "*Band Offsets of High K Gate Oxides on III-V Semiconductors*". *Journal of Applied Physics*, **2006**. 100(1): p. 014111.
28. Wilk, G.D., Wallace, R.M., and Anthony, J.M., "*High-Kappa Gate Dielectrics: Current Status and Materials Properties Considerations*". *Journal of Applied Physics*, **2001**. 89(10): p. 5243-5275.
29. Razeghi, M., "*Fundamentals of Solid State Engineering* **2009**, New York: Springer.
30. Gila, B.P., Ren, F., and Abernathy, C.R., "*Novel Insulators for Gate Dielectrics and Surface Passivation of GaN-Based Electronic Devices*". *Materials Science and Engineering: R: Reports*, **2004**. 44(6): p. 151-184.

31. Lee, C.T., Chen, H.W., and Lee, H.Y., "Metal-Oxide-Semiconductor Devices Using  $Ga_2O_3$  Dielectrics on N-Type GaN". Applied Physics Letters, **2003**. 82(24): p. 4304-4306.
32. Ren, F., Hong, M., Chu, S.N.G., Marcus, M.A., Schurman, M.J., Baca, A., Pearton, S.J., and Abernathy, C.R., "Effect of Temperature on  $Ga_2O_3(Gd_2O_3)/GaN$  Metal-Oxide-Semiconductor Field-Effect Transistors". Applied Physics Letters, **1998**. 73(26): p. 3893-3895.
33. Cook, T.E., Fulton, C.C., Mecouch, W.J., Tracy, K.M., Davis, R.F., Hurt, E.H., Lucovsky, G., and Nemanich, R.J., "Measurement of the Band Offsets of  $SiO_2$  on Clean N- and P-Type GaN(0001)". Journal of Applied Physics, **2003**. 93(7): p. 3995-4004.
34. Casey, H.C., Fountain, G.G., Alley, R.G., Keller, B.P., and Denbaars, S.P., "Low Interface Trap Density for Remote Plasma Deposited  $SiO_2$  on N-Type GaN". Applied Physics Letters, **1996**. 68(13): p. 1850-1852.
35. Sawada, M., Sawada, T., Yamagata, Y., Imai, K., Kimura, H., Yoshino, M., Iizuka, K., and Tomozawa, H., "Electrical Characterization of N-GaN Schottky and PCVD- $SiO_2/N$ -GaN Interfaces". Journal of Crystal Growth, **1998**. 190: p. 706-710.
36. Nakasaki, R., Hashizume, T., and Hasegawa, H., "Insulator-GaN Interface Structures Formed by Plasma-Assisted Chemical Vapor Deposition". Physica E-Low-Dimensional Systems & Nanostructures, **2000**. 7(3-4): p. 953-957.
37. Ren, F., Abernathy, C.R., Mackenzie, J.D., Gila, B.P., Pearton, S.J., Hong, M., Marcus, M.A., Schurman, M.J., Baca, A.G., and Shul, R.J., "Demonstration of GaN MIS Diodes by Using AlN and  $Ga_2O_3(Gd_2O_3)$  as Dielectrics". Solid-State Electronics, **1998**. 42(12): p. 2177-2181.
38. Gila, B.P., Kim, J., Luo, B., Onstine, A., Johnson, W., Ren, F., Abernathy, C.R., and Pearton, S.J., "Advantages and Limitations of MgO as a Dielectric for GaN". Solid-State Electronics, **2003**. 47(12): p. 2139-2142.
39. Chen, J.J., Hlad, M., Gerger, A.P., Gila, B.P., Ren, F., Abernathy, C.R., and Pearton, S.J., "Band Offsets in the  $Mg_{0.5}Ca_{0.5}O/GaN$  Heterostructure System". Journal of Electronic Materials, **2007**. 36(4): p. 368-372.
40. Johnson, J.W., Gila, B.P., Luo, B., Lee, K.P., Abernathy, C.R., Pearton, S.J., Chyi, J.I., Nee, T.E., Lee, C.M., Chuo, C.C., and Ren, F., " $SiO_2/Gd_2O_3/GaN$  Metal Oxide Semiconductor Field Effect Transistors". Journal of the Electrochemical Society, **2001**. 148(6): p. G303-G306.

41. Jur, J.S., Wheeler, G.D., Veety, M.T., Lichtenwalner, D.J., Barlage, D.W., and Johnson, M.a.L. "*Epitaxial Growth of High-Kappa Dielectrics for GaN MOSFETs*". in *Advances in GaN, GaAs, SiC and Related Alloys on Silicon Substrates*. **2008**. San Francisco, CA.
42. Gila, B.P., Johnson, J.W., Mehandru, R., Luo, B., Onstine, A.H., Allums, K.K., Krishnamoorthy, V., Bates, S., Abernathy, C.R., Ren, F., and Pearton, S.J., "*Gadolinium Oxide and Scandium Oxide: Gate Dielectrics for GaN MOSFETs*". *Physica Status Solidi a-Applied Research*, **2001**. 188(1): p. 239-242.
43. Chiu, H.C., Lin, C.W., Chen, C.H., Yang, C.W., Lin, C.K., Fu, J.S., Chang, L.B., Lin, R.M., and Hsueh, K.P., "*Low Hysteresis Dispersion La<sub>2</sub>O<sub>3</sub> AlGa<sub>N</sub>/Ga<sub>N</sub> MOS-HEMTs*". *Journal of the Electrochemical Society*, **2010**. 157(2): p. H160-H164.
44. Gila, B.P., Thaler, G.T., Onstine, A.H., Hlad, M., Gerger, A., Herrero, A., Allums, K.K., Stodilka, D., Jang, S., Kang, B., Anderson, T., Abernathy, C.R., Ren, F., and Pearton, S.J., "*Novel Dielectrics for Gate Oxides and Surface Passivation on GaN*". *Solid-State Electronics*, **2006**. 50(6): p. 1016-1023.
45. Ye, P.D., Yang, B., Ng, K.K., Bude, J., Wilk, G.D., Halder, S., and Hwang, J.C.M., "*GaN Metal-Oxide-Semiconductor High-Electron-Mobility-Transistor with Atomic Layer Deposited Al<sub>2</sub>O<sub>3</sub> as Gate Dielectric*". *Applied Physics Letters*, **2005**. 86(6): p. 063501.
46. Yun, H.S. and Kim, K.H., "*Fabrication and Properties of GaN MIS Capacitors with a Remote-Plasma Atomic-Layer-Deposited Al<sub>2</sub>O<sub>3</sub> Gate Dielectric*". *Journal of the Korean Physical Society*, **2009**. 54(2): p. 707-711.
47. Hashizume, T., Ootomo, S., and Hasegawa, H., "*Suppression of Current Collapse in Insulated Gate AlGa<sub>N</sub>/Ga<sub>N</sub> Heterostructure Field-Effect Transistors Using Ultrathin Al<sub>2</sub>O<sub>3</sub> Dielectric*". *Applied Physics Letters*, **2003**. 83(14): p. 2952-2954.
48. Gregugova, D., Stoklas, R., Cico, K., Heidelberger, G., Marso, M., Novak, J., and Kordos, P., "*Characterization of AlGa<sub>N</sub>/Ga<sub>N</sub> MOSHFETs with Al<sub>2</sub>O<sub>3</sub> as Gate Oxide*". *Physica Status Solidi C - Current Topics in Solid State Physics, Vol 4 No 7 2007*, **2007**. 4(7): p. 2720-2723
49. Wu, Y.Q., Ye, P.D., Wilk, G.D., and Yang, B., "*GaN Metal-Oxide-Semiconductor Field-Effect-Transistor with Atomic Layer Deposited Al<sub>2</sub>O<sub>3</sub> as Gate Dielectric*". *Materials Science and Engineering B-Solid State Materials for Advanced Technology*, **2006**. 135(3): p. 282-284.

50. *International Technology Roadmap for Semiconductors*. **2009** Edition; Available from: <http://www.itrs.net>.
51. Kim, H., Lee, H.B.R., and Maeng, W.J., "Applications of Atomic Layer Deposition to Nanofabrication and Emerging Nanodevices". *Thin Solid Films*, **2009**. 517(8): p. 2563-2580.
52. Groner, M.D., Fabreguette, F.H., Elam, J.W., and George, S.M., "Low-Temperature  $Al_2O_3$  Atomic Layer Deposition". *Chemistry of Materials*, **2004**. 16(4): p. 639-645.
53. George, S.M., "Atomic Layer Deposition: An Overview". *Chem Rev*, **2010**. 110(1): p. 111-31.
54. Wallace, R.M., McIntyre, P.C., Kim, J., and Nishi, Y., "Atomic Layer Deposition of Dielectrics on Ge and III-V Materials for Ultrahigh Performance Transistors". *Mrs Bulletin*, **2009**. 34(7): p. 493-503.
55. Levine, I.N., "*Quantum Chemistry*." 6th ed. **2009**, Upper Saddle River, N.J.: Pearson Prentice Hall. x, 751 p.
56. Kohn, W., "Nobel Lecture: Electronic Structure of Matter-Wave Functions and Density Functionals". *Reviews of Modern Physics*, **1999**. 71(5): p. 1253-1266.
57. Kohn, W. and Sham, L.J., "Self-Consistent Equations Including Exchange and Correlation Effects". *Physical Review*, **1965**. 140(4A): p. 1133-&.
58. Jones, R.O., "The Density Functional Formalism, Its Applications and Prospects". *Reviews of Modern Physics*, **1989**. 61(3): p. 689-746.
59. Becke, A.D., "Density-Functional Exchange-Energy Approximation with Correct Asymptotic Behavior". *Physical Review A*, **1988**. 38(6): p. 3098-3100.
60. Becke, A.D., "A New Mixing of Hartree-Fock and Local Density-Functional Theories". *The Journal of Chemical Physics*, **1993**. 98(2): p. 1372.
61. Becke, A.D., "Density-Functional Thermochemistry. III. The Role of Exact Exchange". *The Journal of Chemical Physics*, **1993**. 98(7): p. 5648.
62. Lee, C., Yang, W., and Parr, R.G., "Development of the Colle-Salvetti Correlation-Energy Formula into a Functional of the Electron Density". *Physical Review B*, **1988**. 37(2): p. 785-789.

63. Foresman, J.B. and Frisch, A., "*Exploring Chemistry with Electronic Structure Methods: A Guide to Using Gaussian*." 2nd ed. **1996**: Gaussian.
64. Elliott, S.D., "*Atomic-Scale Simulation of Ald Chemistry*". Semiconductor Science and Technology, **2012**. 27(7): p. 074008.
65. Ostrikov, K., Tsakadze, E., Jiang, N., Tsakadze, Z., Long, J., R. Storer, and Shuyan, X., "*Dynamics of Mode Transitions in Inductively-Coupled Plasmas*". IEEE Transactions on Plasma Science, **2002**. 30(1): p. 128-129.
66. Fujiwara, H., "*Spectroscopic Ellipsometry: Principles and Applications*. **2007**: Wiley.
67. Azzam, R.M.A. and Bashara, N.M., "*Ellipsometry and Polarized Light*. **1987**: North-Holland.
68. Langereis, E., Heil, S.B.S., Knoops, H.C.M., Keuning, W., Van De Sanden, M.C.M., and Kessels, W.M.M., "*In Situ Spectroscopic Ellipsometry as a Versatile Tool for Studying Atomic Layer Deposition*". Journal of Physics D: Applied Physics, **2009**. 42(7): p. 073001.
69. Hale, J. and Blaine, J., *Comopleteease*, 1999-2010, J.A. Woollam Co., Inc.
70. Azzam, R.M.A. and Bashara, N.M., "*Ellipsometry and Polarized Light*. **1977**, Amsterdam ; New York: North-Holland Pub. Co. xvii, 529 p.
71. Ferlauto, A.S., Ferreira, G.M., Pearce, J.M., Wronski, C.R., Collins, R.W., Deng, X.M., and Ganguly, G., "*Analytical Model for the Optical Functions of Amorphous Semiconductors from the near-Infrared to Ultraviolet: Applications in Thin Film Photovoltaics*". Journal of Applied Physics, **2002**. 92(5): p. 2424-2436.
72. Sancho-Parramon, J., Modreanu, M., Bosch, S., and Stchakovsky, M., "*Optical Characterization of HfO<sub>2</sub> by Spectroscopic Ellipsometry: Dispersion Models and Direct Data Inversion*". Thin Solid Films, **2008**. 516(22): p. 7990-7995.
73. Garcia, J.C., Scolfaro, L.M.R., Lino, A.T., Freire, V.N., Farias, G.A., Silva, C.C., Alves, H.W.L., Rodrigues, S.C.P., and Da Silva, E.F., "*Structural, Electronic, and Optical Properties of ZrO<sub>2</sub> from Ab Initio Calculations*". Journal of Applied Physics, **2006**. 100(10): p. 104103.

74. Takeuchi, H., Ha, D., and King, T.-J., "*Observation of Bulk HfO<sub>2</sub> Defects by Spectroscopic Ellipsometry*". Journal of Vacuum Science & Technology A: Vacuum, Surfaces, and Films, **2004**. 22(4): p. 1337.
75. Zheng, Y., Mizuta, H., Tsuchiya, Y., Endo, M., Sato, D., and Oda, S., "*In Situ Real-Time Spectroscopic Ellipsometry Study of HfO<sub>2</sub> Thin Films Grown by Using the Pulsed-Source Metal-Organic Chemical-Vapor Deposition*". Journal of Applied Physics, **2005**. 97(2): p. 023527.
76. Geisse, N.A., "*AFM and Combined Optical Techniques*". Materials Today, **2009**. 12: p. 40-45.
77. Serway, R.A., "*Physics for Scientists & Engineers*." 3rd ed. Saunders Golden Sunburst Series. **1990**, Philadelphia: Saunders College Pub.
78. Cullity, B.D., "*Elements of X-Ray Diffraction*." 2d ed. Addison-Wesley Series in Metallurgy and Materials. **1978**, Reading, Mass.: Addison-Wesley Pub. Co. xii, 555 p.
79. Wang, Z.L., "*From Nanogenerators to Piezotronics—a Decade-Long Study of ZnO Nanostructures*". MRS Bulletin, **2012**. 37(09): p. 814-827.
80. Lincot, D., "*Solution Growth of Functional Zinc Oxide Films and Nanostructures*". MRS Bulletin, **2010**. 35: p. 778-789.
81. Kamiya, T. and Kawasaki, M., "*ZnO-Based Semiconductors as Building Blocks for Active Devices*". MRS Bulletin, **2008**. 33: p. 1061-1066.
82. Hoffman, R.L., Norris, B.J., and Wager, J.F., "*ZnO -Based Transparent Thin-Film Transistors*". Applied Physics Letters, **2003**. 82(5): p. 733.
83. Pearton, S.J., Norton, D.P., and Ren, F., "*The Promise and Perils of Wide-Bandgap Semiconductor Nanowires for Sensing, Electronic, and Photonic Applications*". Small, **2007**. 3(7): p. 1144-50.
84. Fortunato, E., Barquinha, P., Pimentel, A., Gonçalves, A., Marques, A., Pereira, L., and Martins, R., "*Recent Advances in ZnO Transparent Thin Film Transistors*". Thin Solid Films, **2005**. 487(1-2): p. 205-211.
85. Guziewicz, E., Kowalik, I.A., Godlewski, M., Kopalko, K., Osinniy, V., Wójcik, A., Yatsunencko, S., Łusakowska, E., Paszkowicz, W., and Guziewicz, M., "*Extremely Low Temperature Growth of ZnO by Atomic Layer Deposition*". Journal of Applied Physics, **2008**. 103(3): p. 033515.

86. Krajewski, T., Guziewicz, E., Godlewski, M., Wachnicki, L., Kowalik, I.A., Wojcik-Glodowska, A., Lukasiewicz, M., Kopalko, K., Osinniy, V., and Guziewicz, M., "The Influence of Growth Temperature and Precursors' Doses on Electrical Parameters of ZnO Thin Films Grown by Atomic Layer Deposition Technique". Microelectronics Journal, **2009**. 40(2): p. 293-295.
87. Guziewicz, E., Godlewski, M., Krajewski, T.A., Wachnicki, Ł., Łuka, G., Paszkowicz, W., Domagała, J.Z., Przeździecka, E., Łusakowska, E., and Witkowski, B.S., "ZnO by ALD — Advantages of the Material Grown at Low Temperature". Acta Physica Polonica A, **2009**. 116: p. 814-817.
88. Janocha, E. and Pettenkofer, C., "ALD of ZnO Using Diethylzinc as Metal-Precursor and Oxygen as Oxidizing Agent". Applied Surface Science, **2011**. 257(23): p. 10031-10035.
89. Kim, D., Kang, H., Kim, J.-M., and Kim, H., "The Properties of Plasma-Enhanced Atomic Layer Deposition (ALD) ZnO Thin Films and Comparison with Thermal ALD". Applied Surface Science, **2011**. 257(8): p. 3776-3779.
90. Hussin, R., Hou, X.H., and Choy, K.L., "Growth of ZnO Thin Films on Silicon Substrates by Atomic Layer Deposition". Defect and Diffusion Forum, **2012**. 329: p. 159-164.
91. Sultan, S.M., Clark, O.D., Masaud, T.B., Fang, Q., Gunn, R., Hakim, M.M.A., Sun, K., Ashburn, P., and Chong, H.M.H., "Remote Plasma Enhanced Atomic Layer Deposition of ZnO for Thin Film Electronic Applications". Microelectronic Engineering, **2012**. 97: p. 162-165.
92. Gieraltowska, S., Wachnicki, L., Witkowski, B.S., Guziewicz, E., and Godlewski, M., "Thin Films of High-K Oxides and ZnO for Transparent Electronic Devices". Chemical Vapor Deposition, **2013**. 19(4-6): p. 213-220.
93. Kawamura, Y., Hattori, N., Miyatake, N., and Uraoka, Y., "Comparison between ZnO Films Grown by Plasma-Assisted Atomic Layer Deposition Using H<sub>2</sub>O Plasma and O<sub>2</sub> Plasma as Oxidant". Journal of Vacuum Science & Technology A: Vacuum, Surfaces, and Films, **2013**. 31(1): p. 01A142.
94. Yamada, A., Sang, B.S., and Konagai, M., "Atomic Layer Deposition of ZnO Transparent Conducting Oxides". Applied Surface Science, **1997**. 112: p. 216-222.
95. Ott, A.W. and Chang, R.P.H., "Atomic Layer-Controlled Growth of Transparent Conducting ZnO on Plastic Substrates". Materials Chemistry and Physics, **1999**. 58(2): p. 132-138.

96. Huby, N., Ferrari, S., Guziewicz, E., Godlewski, M., and Osinniy, V., "Electrical Behavior of Zinc Oxide Layers Grown by Low Temperature Atomic Layer Deposition". Applied Physics Letters, **2008**. 92(2): p. 023502.
97. Lim, S.J., Kwon, S., and Kim, H., " ZnO Thin Films Prepared by Atomic Layer Deposition and RF Sputtering as an Active Layer for Thin Film Transistor". Thin Solid Films, **2008**. 516(7): p. 1523-1528.
98. Keun Kim, S., Seong Hwang, C., Ko Park, S.-H., and Jin Yun, S., "Comparison between ZnO Films Grown by Atomic Layer Deposition Using H<sub>2</sub>O or O<sub>3</sub> as Oxidant". Thin Solid Films, **2005**. 478(1-2): p. 103-108.
99. Thomas, M.A. and Cui, J.B., "Highly Tunable Electrical Properties in Undoped ZnO Grown by Plasma Enhanced Thermal-Atomic Layer Deposition". ACS Appl Mater Interfaces, **2012**.
100. M. J. Frisch, G.W.T., H. B. Schlegel, G. E. Scuseria, M. A. Robb, J. R. Cheeseman, G. Scalmani, V. Barone, B. Mennucci, G. A. Petersson, H. Nakatsuji, M. Caricato, X. Li, H. P. Hratchian, A. F. Izmaylov, J. Bloino, G. Zheng, J. L. Sonnenberg, M. Hada, M. Ehara, K. Toyota, R. Fukuda, J. Hasegawa, M. Ishida, T. Nakajima, Y. Honda, O. Kitao, H. Nakai, T. Vreven, J. J. A. Montgomery, J. E. Peralta, F. Ogliaro, M. Bearpark, J. J. Heyd, E. Brothers, K. N. Kudin, V. N. Staroverov, T. Keith, R. Kobayashi, J. Normand, K. Raghavachari, A. Rendell, J. C. Burant, S. S. Iyengar, J. Tomasi, M. Cossi, N. Rega, J. M. Millam, M. Klene, J. E. Knox, J. B. Cross, V. Bakken, C. Adamo, J. Jaramillo, R. Gomperts, R. E. Stratmann, O. Yazyev, A. J. Austin, R. Cammi, C. Pomelli, J. W. Ochterski, R. L. Martin, K. Morokuma, V. G. Zakrzewski, G. A. Voth, P. Salvador, J. J. Dannenberg, S. Dapprich, A. D. Daniels, O. Farkas, J. B. Foresman, J. V. Ortiz, J. Cioslowski and D. J. Fox, Gaussian, Inc., Wallingford Ct, 2010., *Gaussian 09*, 2010.
101. Krishnan, R., Binkley, J.S., Seeger, R., and Pople, J.A., "Self-Consistent Molecular Orbital Methods. XX. A Basis Set for Correlated Wave Functions". The Journal of Chemical Physics, **1980**. 72(1): p. 650.
102. Mclean, A.D. and Chandler, G.S., "Contracted Gaussian Basis Sets for Molecular Calculations. I. Second Row Atoms, Z=11-18". The Journal of Chemical Physics, **1980**. 72(10): p. 5639.
103. Munk, B.H. and Schlegel, H.B., "Molecular Orbital Studies of Zinc Oxide Chemical Vapor Deposition: Gas-Phase Radical Reactions". Chemistry of Materials, **2006**. 18: p. 1878-1884.

104. Smith, S.M. and Schlegel, H.B., "*Molecular Orbital Studies of Zinc Oxide Chemical Vapor Deposition: Gas-Phase Hydrolysis of Diethyl Zinc, Elimination Reactions, and Formation of Dimers and Tetramers*". Chemistry of Materials, **2003**. 15: p. 162-166.
105. Kim, Y.S. and Won, Y.S., "*Investigation on Reaction Pathways for ZnO Formation from Diethylzinc and Water During Chemical Vapor Deposition*". Bulletin of the Korean Chemical Society, **2009**. 30(7): p. 1573-1578.
106. Yushikawa, H. and Adachi, S., "*Optical Constant of ZnO*". Japanese Journal of Applied Physics, **1997**. 36: p. 6237-6243.
107. Huang, B. and Yang, H.-D., "*Optical Constants of ZnO Films*". ECS Transactions, **2011**. 34: p. 547-550
108. Srikant, V. and Clarke, D.R., "*On the Optical Band Gap of Zinc Oxide*". Journal of Applied Physics, **1998**. 83(10): p. 5447.
109. Caglar, M., Caglar, Y., Aksoy, S., and Ilican, S., "*Temperature Dependence of the Optical Band Gap and Electrical Conductivity of Sol-Gel Derived Undoped and Li-Doped ZnO Films*". Applied Surface Science, **2010**. 256(16): p. 4966-4971.
110. Jensen, G.H.E., "*Temperature Dependence of the Band Gap in ZnO from Reflection Data*". Physica Status Solidi (b), **1974**. 64(K51).
111. Allen, P.B. and Heine, V., "*Theory of the Temperature Dependence of Electronic Band Structures*". Journal of Physics C: Solid State Physics, **1976**. 9(12): p. 2305-2312.
112. Mar, L.G., Timbrell, P.Y., and Lamb, R.N., "*An XPS Study of Zinc Oxide Thin Film Growth on Copper Using Zinc Acetate as a Precursor*". Thin Solid Films, **1993**. 223: p. 341-347.
113. Strohmeier, B.R. and Hercules, D.M., "*Surface Spectroscopic Characterization of the Interaction between Zinc Ions and  $\gamma$ -Alumina*". Journal of Catalysis, **1984**. 86: p. 266-279.
114. Brow, R.K., "*An XPS Study of Oxygen Bonding in Zinc Phosphate and Zinc Borophosphate Glasses*". Journal of Non-Crystalline Solids, **1996**. 194: p. 267-273.

115. Onyiriuka, E.C., "Zinc Phosphate Glass Surfaces Studied by XPS". Journal of Non-Crystalline Solids, **1993**. 163: p. 268-273.
116. Heil, S.B.S., Van Hemmen, J.L., Van De Sanden, M.C.M., and Kessels, W.M.M., "Reaction Mechanisms During Plasma-Assisted Atomic Layer Deposition of Metal Oxides: A Case Study for  $Al_2O_3$ ". Journal of Applied Physics, **2008**. 103(10): p. 103302.
117. Profijt, H.B., Potts, S.E., Van De Sanden, M.C.M., and Kessels, W.M.M., "Plasma-Assisted Atomic Layer Deposition: Basics, Opportunities, and Challenges". Journal of Vacuum Science & Technology A: Vacuum, Surfaces, and Films, **2011**. 29(5): p. 050801.
118. Warner, E.J., Cramer, C.J., and Gladfelter, W.L., "Atomic Layer Deposition of Zinc Oxide: Understanding the Reactions of Ozone with Diethylzinc". Journal of Vacuum Science & Technology A: Vacuum, Surfaces, and Films, **2013**. 31(4): p. 041504.
119. Kovács, I., Iost, N., and Solymosi, F., "Thermal and Photo-Induced Dissociation of  $(C_2H_5)_2Zn$  to Yield  $C_2H_5$  on the Pd(100) Surface". The Journal of Chemical Physics, **1994**. 101(5): p. 4236.
120. Elam, J.W., Sechrist, Z.A., and George, S.M., "ZnO/ $Al_2O_3$  Nanolaminates Fabricated by Atomic Layer Deposition: Growth and Surface Roughness Measurements". Thin Solid Films, **2002**. 414(1): p. 43-55.
121. Kowalik, I.A., Guziewicz, E., Kopalko, K., Yatsunenkov, S., Wójcik-Głodowska, A., Godlewski, M., Dłużewski, P., Łusakowska, E., and Paszkowicz, W., "Structural and Optical Properties of Low-Temperature ZnO Films Grown by Atomic Layer Deposition with Diethylzinc and Water Precursors". Journal of Crystal Growth, **2009**. 311(4): p. 1096-1101.
122. Hausmann, D.M. and Gordon, R.G., "Surface Morphology and Crystallinity Control in the Atomic Layer Deposition (ALD) of Hafnium and Zirconium Oxide Thin Films". Journal of Crystal Growth, **2003**. 249: p. 251-261.
123. Makino, H., Miyake, A., Yamada, T., Yamamoto, N., and Yamamoto, T., "Influence of Substrate Temperature and Zn-Precursors on Atomic Layer Deposition of Polycrystalline ZnO Films on Glass". Thin Solid Films, **2009**. 517(10): p. 3138-3142.

124. Pung, S.Y., Choy, K.L., Hou, X., and Shan, C., "*Preferential Growth of ZnO Thin Films by the Atomic Layer Deposition Technique*". Nanotechnology, **2008**. 19(43): p. 435609.
125. Miikkulainen, V., Leskelä, M., Ritala, M., and Puurunen, R.L., "*Crystallinity of Inorganic Films Grown by Atomic Layer Deposition: Overview and General Trends*". Journal of Applied Physics, **2013**. 113(2): p. 021301.
126. Fujimura, N., Nishihara, T., Goto, S., Xu, J., and Lto, T., "*Control of Preferred Orientation for ZnO<sub>x</sub> Films: Control of Self-Texture*". Journal of Crystal Growth, **1993**. 130: p. 269-279.
127. Malm, J., Sahramo, E., Perälä, J., Sajavaara, T., and Karppinen, M., "*Low-Temperature Atomic Layer Deposition of ZnO Thin Films: Control of Crystallinity and Orientation*". Thin Solid Films, **2011**. 519(16): p. 5319-5322.
128. Park, S.-H.K. and Lee, Y.E., "*Controlling Preferred Orientation of ZnO Thin Films by Atomic Layer Deposition*". Journal of Materials Science, **2004**. 39: p. 2195–2197.
129. Kohan, A.F., Ceder, G., Morgan, D., and Walle, C.G.V.D., "*First-Principles Study of Native Point Defects in ZnO*". Physical Review B, **2000**. 61(22): p. 15019 - 15027.
130. Janotti, A. and Van De Walle, C.G., "*Native Point Defects in ZnO*". Physical Review B, **2007**. 76(16).
131. Puurunen, R.L., "*Surface Chemistry of Atomic Layer Deposition: A Case Study for the Trimethylaluminum/Water Process*". Journal of Applied Physics, **2005**. 97(12): p. 121301.
132. Widjaja, Y. and Musgrave, C.B., "*Quantum Chemical Study of the Mechanism of Aluminum Oxide Atomic Layer Deposition*". Applied Physics Letters, **2002**. 80(18): p. 3304.
133. Widjaja, Y. and Musgrave, C.B., "*Quantum Chemical Study of the Elementary Reactions in Zirconium Oxide Atomic Layer Deposition*". Applied Physics Letters, **2002**. 81(2): p. 304.
134. Widjaja, Y. and Musgrave, C.B., "*Atomic Layer Deposition of Hafnium Oxide: A Detailed Reaction Mechanism from First Principles*". The Journal of Chemical Physics, **2002**. 117(5): p. 1931.

135. Karzel, H., Potzel, W., Fferlein, M.K., Schiessl, W., Steiner, M., Hiller, U., Kalvius, G.M., Mitchell, D.W., Das, T.P., Blaha, P., Schwarz, K., and Pasternak, M.P., "*Lattice Dynamics and Hyperfine Interactions in ZnO and ZnSe at High External Pressures*". Physical Review B **1996**. 53(17): p. 11425-11438.
136. Haaland, A., Green, J.C., Mcgrady, G.S., Downs, A.J., Gullo, E., Lyall, M.J., Timberlake, J., Tutukin, A.V., Volden, H.V., and Ostby, K.-A., "*The Length, Strength and Polarity of Metal–Carbon Bonds: Dialkylzinc Compounds Studied by Density Functional Theory Calculations, Gas Electron Diffraction and Photoelectron Spectroscopy*". Dalton Transactions, **2003**(22): p. 4356.
137. Ferguson, J.D., Weimer, A.W., and George, S.M., "*Surface Chemistry and Infrared Absorbance Changes During ZnO Atomic Layer Deposition on ZrO<sub>2</sub> and BaTiO<sub>3</sub> Particles*". Journal of Vacuum Science & Technology A: Vacuum, Surfaces, and Films, **2005**. 23(1): p. 118.
138. Thompson, D.P., Dickins, A.M., and Thorp, J.S., "*The Dielectric Properties of Zirconia*". Journal of Materials Science: Materials in Electronics, **1992**. 27(8): p. 2267-2271.
139. Robertson, J., "*High Dielectric Constant Gate Oxides for Metal Oxide Si Transistors*". Reports on Progress in Physics, **2006**. 69(2): p. 327-396.
140. Robertson, J., "*High Dielectric Constant Oxides*". The European Physical Journal Applied Physics, **2004**. 28(3): p. 265-291.
141. Cho, H.J., Kim, Y.D., Park, D.S., Lee, E., Park, C.H., Jang, J.S., Lee, K.B., Kim, H.W., Chae, S.J., Ki, Y.J., Il Keun Han, and Song, Y.W., "*New Tit Capacitor with ZrO<sub>2</sub>/Al<sub>2</sub>O<sub>3</sub>/ZrO<sub>2</sub> Dielectrics for 60nm and Below Drams*", in *Solid-State Device Research Conference 2006*: Montreux. p. 146-149.
142. Niinistö, J., Kukli, K., Heikkilä, M., Ritala, M., and Leskelä, M., "*Atomic Layer Deposition of High-Koxides of the Group 4 Metals for Memory Applications*". Advanced Engineering Materials, **2009**. 11(4): p. 223-234.
143. Shim, J.H., Chao, C.-C., Huang, H., and Prinz, F.B., "*Atomic Layer Deposition of Ytria-Stabilized Zirconia for Solid Oxide Fuel Cells*". Chem. Mater., **2007**. 19: p. 3850-3854.
144. Ritala, M. and Leskela, M., "*Zirconium Dioxide Thin Films Deposited by ALE Using Zirconium Tetrachloride as Precursor*". Applied Surface Science, **1994**. 75: p. 333-340.

145. Cassir, M., Goubin, F., Bernay, C.C., Vernoux, P., and Lincot, D., "Synthesis of  $ZrO_2$  Thin Films by Atomic Layer Deposition: Growth Kinetics, Structural and Electrical Properties". Applied Surface Science, **2000**. 193: p. 120-128.
146. Copel, M., Gribelyuk, M., and Gusev, E., "Structure and Stability of Ultrathin Zirconium Oxide Layers on Si(001)". Applied Physics Letters, **2000**. 76(4): p. 436.
147. Kukli, K., Ritala, M., and Leskelä, M., "Low-Temperature Deposition of Zirconium Oxide Based Nanocrystalline Films by Alternate Supply of  $Zr[OC(CH_3)_3]_4$  and  $H_2O$ ". Chemical Vapor Deposition, **2000**. 6: p. 297-302.
148. Ritala, M., "Atomic Layer Deposition of Oxide Thin Films with Metal Alkoxides as Oxygen Sources". Science, **2000**. 288(5464): p. 319-321.
149. Smith, R.C., Hoilien, N., Taylor, C.J., Ma, T., Campbell, S.A., Roberts, J.T., Copel, M., Buchanan, D.A., Gribelyuk, M., and Gladfelter, W.L., "Low Temperature Chemical Vapor Deposition of  $ZrO_2$  on Si(100) Using Anhydrous Zirconium(IV) Nitrate". Journal of The Electrochemical Society, **2000**. 147(9): p. 3472-3476.
150. Jones, A.C., Williams, P.A., Roberts, J.L., Leedham, T.J., Davies, H.O., Matero, R., Ritala, M., and Leskelä, M., "Atomic-Layer Deposition of  $ZrO_2$  Thin Films Using New Alkoxide Precursors". MRS Symposium Proceedings, **2002**. 716: p. B3.5.1-B3.5.6.
151. Niinistö, J., Kukli, K., Tamm, A., Putkonen, M., Dezelah, C.L., Niinistö, L., Lu, J., Song, F., Williams, P., Heys, P.N., Ritala, M., and Leskelä, M., "Advanced Cyclopentadienyl Precursors for Atomic Layer Deposition of  $ZrO_2$  Thin Films". Journal of Materials Chemistry, **2008**. 18(28): p. 3385.
152. Kukli, K., Niinistö, J., Tamm, A., Ritala, M., and Leskelä, M., "Behavior of Zirconium Oxide Films Processed from Novel Monocyclopentadienyl Precursors by Atomic Layer Deposition". Journal of Vacuum Science & Technology B: Microelectronics and Nanometer Structures, **2009**. 27(1): p. 226.
153. Chen, T., Cameron, T.M., Nguyen, S.D., Stauf, G.T., Peters, D.W., Maylott, L., Li, W., Xu, C., Roeder, J.F., Hendrix, B.C., Hilgarth, M., Niinistö, J., Kukli, K., Ritala, M., and Leskelä, M., "Novel Zirconium Precursors for Atomic Layer Deposition of  $ZrO_2$  Films". ECS Transactions, **2008**. 16(4): p. 87-101.

154. Dezelah, C.L., Niinistö, J., Kukli, K., Munnik, F., Lu, J., Ritala, M., Leskelä, M., and Niinistö, L., "*The Atomic Layer Deposition of HfO<sub>2</sub> and ZrO<sub>2</sub> using Advanced Metallocene Precursors and H<sub>2</sub>O as the Oxygen Source*". Chemical Vapor Deposition, **2008**. 14(11-12): p. 358-365.
155. Hausmann, D.M., Kim, E., Becker, J., and Gordon, R.G., "*Atomic Layer Deposition of Hafnium and Zirconium Oxides Using Metal Amide Precursors*". Chemistry of Materials, **2002**. 14: p. 4350-4358.
156. Chao, C.-C., Kim, Y.B., and Prinz, F.B., "*Surface Modification of Yttria-Stabilized Zirconia Electrolyte by Atomic Layer Deposition*". Nano Letters, **2009**. 9(10): p. 3626-3628.
157. Shim, J.H., Park, J.S., An, J., Gür, T.M., Kang, S., and Prinz, F.B., "*Intermediate-Temperature Ceramic Fuel Cells with Thin Film Yttrium-Doped Barium Zirconate Electrolytes*". Chemistry of Materials, **2009**. 21(14): p. 3290-3296.
158. Wu, F., Wu, J.N., Banerjee, S., Blank, O., and Banerjee, P., "*Frontiers in Applied Atomic Layer Deposition (ALD) Research*". Materials Science Forum, **2012**. 736: p. 147-182.
159. Bothe, K.M., Hauff, P.a.V., Afshar, A., Ali Foroughi-Abari, Cadien, K.C., and Barlage, D.W., "*Capacitance Modeling and Characterization of Planar MOSCAP Devices for Wideband-Gap Semiconductors with High-K Dielectrics*". IEEE Transactions on Electron Devices, **2012**. 59(10).
160. Von Hauff, P., Afshar, A., Foroughi-Abari, A., Bothe, K., Cadien, K., and Barlage, D., "*ZrO<sub>2</sub> on Gan Metal Oxide Semiconductor Capacitors Via Plasma Assisted Atomic Layer Deposition*". Applied Physics Letters, **2013**. 102(25): p. 251601.
161. Binning, R.C. and Curtiss, L.A., "*Compact Contracted Basis Sets for Third-Row Atoms: Ga-Kr*". Journal of Computational Chemistry, **1990**. 11(10): p. 1206-1216.
162. Rassolov, V.A., Pople, J.A., Ratner, M.A., and Windus, T.L., "*6-31g Basis Set for Atoms K through Zn*". The Journal of Chemical Physics, **1998**. 109(4): p. 1223.
163. Petersson, G.A., Bennett, A., Tensfeldt, T.G., Al-Laham, M.A., Shirley, W.A., and Mantzaris, J., "*A Complete Basis Set Model Chemistry. I. The Total Energies of Closed-Shell Atoms and Hydrides of the First-Row Elements*". The Journal of Chemical Physics, **1988**. 89(4): p. 2193.

164. Rassolov, V.A., Ratner, M.A., John A. Pople, Redfren, P.C., and Curtiss, L.A., "6-31g $\square$  Basis Set for Third-Row Atoms". Journal of Computational Chemistry, **2001**. 22(9): p. 976-984.
165. Francl, M.M., "Self-Consistent Molecular Orbital Methods. XXIII. A Polarization-Type Basis Set for Second-Row Elements". The Journal of Chemical Physics, **1982**. 77(7): p. 3654.
166. Hehre, W.J., "Self—Consistent Molecular Orbital Methods. XII. Further Extensions of Gaussian—Type Basis Sets for Use in Molecular Orbital Studies of Organic Molecules". The Journal of Chemical Physics, **1972**. 56(5): p. 2257.
167. Hariharan, P.C. and Pople, J.A., "The Influence of Polarization Functions on Molecular Orbital Hydrogenation Energies". Theoretical Chimistry Acta (Berl.), **1973**. 28: p. 213-222.
168. Ditchfield, R., "Self-Consistent Molecular-Orbital Methods. IX. An Extended Gaussian-Type Basis for Molecular-Orbital Studies of Organic Molecules". The Journal of Chemical Physics, **1971**. 54(2): p. 724.
169. Wadt, W.R. and Hay, P.J., "Ab Initio Effective Core Potentials for Molecular Calculations. Potentials for Main Group Elements Na to Bi". The Journal of Chemical Physics, **1985**. 82(1): p. 284.
170. Hay, P.J. and Wadt, W.R., "Ab Initio Effective Core Potentials for Molecular Calculations. Potentials for the Transition Metal Atoms Sc to Hg". The Journal of Chemical Physics, **1985**. 82(1): p. 270.
171. Hay, P.J. and Wadt, W.R., "Ab Initio Effective Core Potentials for Molecular Calculations. Potentials for K to Au Including the Outermost Core Orbitals". The Journal of Chemical Physics, **1985**. 82(1): p. 299.
172. Chen, W., Zhang, D.W., Ren, J., Lu, H.-L., Zhang, J.-Y., Xu, M., Wang, J.-T., and Wang, L.-K., "Density Functional Theory Study of Initial Stage of ZrO<sub>2</sub> Atomic Layer Deposition on Ge/Si(100)-(2 $\times$ 1) Surface". Thin Solid Films, **2005**. 479(1-2): p. 73-76.
173. Han, J.H., Gao, G., Widjaja, Y., Garfunkel, E., and Musgrave, C.B., "A Quantum Chemical Study of ZrO<sub>2</sub> Atomic Layer Deposition Growth Reactions on the SiO<sub>2</sub> Surface". Surface Science, **2004**. 550(1-3): p. 199-212.

174. Zhu, L.Q., Fang, Q., He, G., Liu, M., and Zhang, L.D., "*Interfacial and Optical Properties of ZrO<sub>2</sub>/Si by Reactive Magnetron Sputtering*". Materials Letters, **2006**. 60(7): p. 888-891.
175. Jerman, M., Qiao, Z., and Mergel, D., "*Refractive Index of Thin Films of SiO<sub>2</sub>, ZrO<sub>2</sub>, and HfO<sub>2</sub> as a Function of the Films' Mass Density*". APPLIED OPTICS, **2005**. 44(15): p. 3006-3012.
176. Zhao, S. and Xu, K., "*The Characterization of ZrO<sub>2</sub> Films with Different Substrate Bias Voltages*". Journal of the Korean Physical Society, **2005**. 46: p. S70-S74.
177. George, S.M., "*Atomic Layer Deposition: An Overview*". Chemical Reviews, **2010**. 110(1): p. 111-31.
178. Majumdar, D. and Chatterjee, D., "*X-Ray Photoelectron Spectroscopic Studies on Yttria, Zirconia, and Yttria Stabilized Zirconia*". Journal of Applied Physics, **1991**. 70: p. 988-992.
179. Korduban, A.M., Konstantinova, T.E., Danilenko, I.A., Volkova, G.K., and Glazunova, V.A., "*Xray Photoelectron Spectroscopy of Nanopowders of ZrO<sub>2</sub>-Y<sub>2</sub>O<sub>3</sub>-Cr<sub>2</sub>O<sub>3</sub> Compounds*". Functional Materials, **2007**. 14(4): p. 454-459.
180. Ardizzone, S., Cattania, M.G., and Lugo, P., "*Interfacial Electrostatics Behavior of Oxides: Correlations with Structural and Surface Parameters of the Phase*". Electrochimica Acta, **1994**. 39(11): p. 1509-1517.
181. Sarma, D.D. and Rao, C.N.R., "*Xpes Studies of Oxides of Second- and Third-Row Transition Metals Including Rare Earths*". Journal of Electron Spectroscopy and Related Phenomena, **1980**. 20: p. 25-45.
182. Anderson, J.A. and Fierro, J.L.G., "*Bulk and Surface Properties of Copper Containing Oxides of General Formula LaZr<sub>1-x</sub>Cu<sub>x</sub>O<sub>3</sub>*". Journal of Solid State Chemistry, **1994**. 108: p. 305-313.
183. Severin, K.G. and Ledford, J.S., "*Characterization of Titanium and Zirconium Valerate Sol-Gel Films*". Chem. Mater., **1994**. 6: p. 890-898.
184. Kaichev, V.V., Dubinin, Y.V., Smirnova, T.P., and Lebedev, M.S., "*A Study of the Structure of (HfO<sub>2</sub>)<sub>x</sub>(Al<sub>2</sub>O<sub>3</sub>)<sub>1-x</sub>/Si Films by X-Ray Photoelectron Spectroscopy*". Journal of Structural Chemistry, **2011**. 52(3): p. 480-487.

185. Jeong, D., Lee, J., and Kim, J., "Effects of Various Oxidizers on the  $ZrO_2$  thin Films Deposited by Atomic Layer Deposition". Integrated Ferroelectrics, **2004**. 67(1): p. 41-48.
186. Leger, J., Tomaszewski, P., Atouf, A., and Pereira, A., "Pressure-Induced Structural Phase Transitions in Zirconia under High Pressure". Physical Review B, **1993**. 47(21): p. 14075-14083.
187. Garvie, R.C., "Stabilization of the Tetragonal Structure in Zirconia Microcrystals ". The Journal of Physical Chemistry, **1978**. 82(2): p. 218-224.
188. Garvie, R.C., "The Occurrence of Metastable Tetragonal Zirconia as a Crystallite Size Effect". Journal of Physical Chemistry, **1965**. 69(4): p. 1238-1245.
189. Garvie, R.C. and Goss, M.F., "Intrinsic Size Dependence of the Phase Transformation Temperature in Zirconia microcrystals". Journal of Materials Science, **1986**. 21: p. 1253-1257.
190. Christensen, A. and Carter, E.A., "First-Principles Study of the Surfaces of Zirconia". Physical Review B, **1998**. 58(12): p. 8050-8064.
191. Witczak, S.C., Suehle, J.S., and Gaitan, M., "An Experimental Comparison of Measurement Techniques to Extract Si-SiO<sub>2</sub> Interface Trap Density". Solid State Electronics, **1992**. 35(3): p. 345-355.
192. Soo, Y.L., Chen, P.J., Huang, S.H., Shiu, T.J., Tsai, T.Y., Chow, Y.H., Lin, Y.C., Weng, S.C., Chang, S.L., Wang, G., Cheung, C.L., Sabirianov, R.F., Mei, W.N., Namavar, F., Haider, H., Garvin, K.L., Lee, J.F., Lee, H.Y., and Chu, P.P., "Local Structures Surrounding Zr in Nanostructurally Stabilized Cubic Zirconia: Structural Origin of Phase Stability". Journal of Applied Physics, **2008**. 104.
193. Hagen, K., Holwill, C.J., Rice, D.A., and Runnaclesl, J.D., "Gas-Phase Electron Diffraction Study of Tetrakis(Dimethylamido)Zirconium(Iv),  $Zr(NMe_2)_4$ ". Inorganic Chemistry, **1988**. 27: p. 2032-2035.
194. Kim, I.-W., Kim, S.-J., Kim, D.-H., Woo, H., Park, M.-Y., and Rhee, S.-W., "Fourier Transform Infrared Spectroscopy Studies on Thermal Decomposition of Tetrakis-Dimethyl-Amido Zirconium for Chemical Vapor Deposition of  $ZrN$ ". Korean Journal of Chemical Engineering, **2004**. 21(6): p. 1256-1259.

195. Emsley, J., "Very Strong Hydrogen Bonding". Chemical Society Reviews, **1980**. 9: p. 91-124.
196. Choi, J.H., Mao, Y., and Chang, J.P., "Development of Hafnium Based High-K Materials—a Review". Materials Science and Engineering: R: Reports, **2011**. 72(6): p. 97-136.
197. Wilk, G.D., Wallace, R.M., and Anthony, J.M., "Hafnium and Zirconium Silicates for Advanced Gate Dielectrics". Journal of Applied Physics, **2000**. 87(1): p. 484-492.
198. Hubbard, K.J. and Schlom, D.G., "Thermodynamic Stability of Binary Oxides in Contact with Silicon". Journal of Materials Research, **1996**. 11(11): p. 2757-2776.
199. Bohr, M. and Mistry, K., *Intel's Revolutionary 22 nm Transistor Technology*, **2011**.
200. S. Banerjee, E. Tutuc, S. Kim, T. Aykol, J. Mustafa, D. Shahredji, and J. Donnell "High-K Dielectrics for Ge, III-V and Graphene MOSFETs" **2009** in *216th ECS Meeting*, Vienna, Austria, p. 2130
201. Hong, M., Kwo, J.R., Tsai, P.-C., Chang, Y., Huang, M.-L., Chen, C.-P., and Lin, T.-D., "III-V Metal-Oxide-Semiconductor Field-Effect Transistors with High K Dielectrics". Japanese Journal of Applied Physics, **2007**. 46(5B): p. 3167-3180.
202. Kukli, K., Ritala, M., Sundqvist, J., Aarik, J., Lu, J., Sajavaara, T., Leskela, M., and Harsta, A., "Properties of Hafnium Oxide Films Grown by Atomic Layer Deposition from Hafnium Tetraiodide and Oxygen". Journal of Applied Physics, **2002**. 92(10): p. 5698-5703.
203. Renault, O., Samour, D., Rouchon, D., Holliger, P., Papon, A.M., Blin, D., and Marthon, S., "Interface Properties of Ultra-Thin HfO<sub>2</sub> Films Grown by Atomic Layer Deposition on SiO<sub>2</sub>/Si". Thin Solid Films, **2003**. 428(1-2): p. 190-194.
204. Ritala, M., Leskela, M., Niinisto, L., Prohaska, T., Friedbacher, G., and Grasserbauer, M., "Development of Crystallinity and Morphology in Hafnium Dioxide Thin-Films Grown by Atomic Layer Epitaxy". Thin Solid Films, **1994**. 250(1-2): p. 72-80.

205. Aarik, J., Aidla, A., Mandar, H., Sammelselg, V., and Uustare, T., "Texture Development in Nanocrystalline Hafnium Dioxide Thin Films Grown by Atomic Layer Deposition". Journal of Crystal Growth, **2000**. 220(1-2): p. 105-113.
206. Copel, M., Gribelyuk, M., and Gusev, E., "Structure and Stability of Ultrathin Zirconium Oxide Layers on Si(001)". Applied Physics Letters, **2000**. 76(4): p. 436-438.
207. Aarik, J., Aidla, A., Kiisler, A.A., Uustare, T., and Sammelselg, V., "Influence of Substrate Temperature on Atomic Layer Growth and Properties of  $\text{HfO}_2$  Thin Films". Thin Solid Films, **1999**. 340(1-2): p. 110-116.
208. Conley, J.F., Ono, Y., Tweet, D.J., Zhuang, W., and Solanki, R., "Atomic Layer Deposition of Thin Hafnium Oxide Films Using a Carbon Free Precursor". Journal of Applied Physics, **2003**. 93(1): p. 712-718.
209. Kukli, K., Ritala, M., Leskelä, M., Sajavaara, T., Keinonen, J., Jones, A.C., and Tobin, N.L., "Atomic Layer Deposition of Hafnium Dioxide Films from Hafnium Hydroxylamide and Water". Chemical Vapor Deposition, **2004**. 10(2).
210. Niinistö, J., Mäntymäki, M., Kukli, K., Costelle, L., Puukilainen, E., Ritala, M., and Leskelä, M., "Growth and Phase Stabilization of  $\text{HfO}_2$  Thin Films by ALD Using Novel Precursors". Journal of Crystal Growth, **2010**. 312(2): p. 245-249.
211. Bradley, D.C. and Thomas, I.M., "Metallo-Organic Compounds Containing Metal-Nitrogen Bonds .I. Some Dialkylamino-Derivatives of Titanium and Zirconium". Journal of the Chemical Society, **1960**(Oct): p. 3857-3861.
212. Van Mol, A.M.B., Driessen, J.P.a.M., Linden, J.L., De Croon, M.H.J.M., Spee, C.I.M.A., and Schouten, J.C., "Vapor Pressures of Precursors for the CVD of Titanium Nitride and Tin Oxide". Chemical Vapor Deposition, **2001**. 7(3): p. 101-104.
213. Kukli, K., Pilvi, T., Ritala, M., Sajavaara, T., Lu, J., and Leskelä, M., "Atomic Layer Deposition of Hafnium Dioxide Thin Films from Hafnium Tetrakis(Dimethylamide) and Water". Thin Solid Films, **2005**. 491(1-2): p. 328-338.

214. Kukli, K., Ritala, M., Lu, J., Hårsta, A., and Leskelä, M., "*Properties of HfO<sub>2</sub> Thin Films Grown by ALD from Hafnium Tetrakis(Ethylmethanamide) and Water*". Journal of The Electrochemical Society, **2004**. 151(8): p. F189.
215. Deshpande, A., Inman, R., Jursich, G., and Takoudis, C., "*Atomic Layer Deposition and Characterization of Hafnium Oxide Grown on Silicon from Tetrakis(Diethylamino)Hafnium and Water Vapor*". Journal of Vacuum Science & Technology A: Vacuum, Surfaces, and Films, **2004**. 22(5): p. 2035.
216. Katamreddy, R., Inman, R., Jursich, G., Soulet, A., and Takoudis, C., "*Atomic Layer Deposition of HfO<sub>2</sub>, Al<sub>2</sub>O<sub>3</sub>, and HfAlO<sub>x</sub> Using O<sub>3</sub> and Metal(Diethylamino) Precursors*". Journal of Materials Research, **2007**. 22(12): p. 3455-3464.
217. Park, P.K., Roh, J.-S., Choi, B.H., and Kang, S.-W., "*Interfacial Layer Properties of HfO<sub>2</sub> Films Formed by Plasma-Enhanced Atomic Layer Deposition on Silicon*". Electrochemical and Solid-State Letters, **2006**. 9(5): p. F34.
218. Rodriguez-Reyes, J.C.F. and Teplyakov, A.V., "*Mechanisms of Adsorption and Decomposition of Metal Alkylamide Precursors for Ultrathin Film Growth*". Journal of Applied Physics, **2008**. 104(8).
219. Li, K.J., Li, S.G., Li, N., Klein, T.M., and Dixon, D.A., "*Tetrakis(Ethylmethanamido) Hafnium Adsorption and Reaction on Hydrogen-Terminated Si(100) Surfaces*". Journal of Physical Chemistry C, **2011**. 115(38): p. 18560-18571.
220. Li, K., Li, S., Li, N., Dixon, D.A., and Klein, T.M., "*Tetrakis(Dimethylamido)Hafnium Adsorption and Reaction on Hydrogen Terminated Si(100) Surfaces*". J. Phys. Chem. C, **2010**. 114: p. 14061–14075
221. Zukic, M., Torr, D.G., Spann, J.F., and Torr, M.R., "*Vacuum Ultraviolet Thin Films. 1: Optical Constants of BaF<sub>2</sub>, CaF<sub>2</sub>, LaF<sub>3</sub>, MgF<sub>2</sub>, Al<sub>2</sub>O<sub>3</sub>, HfO<sub>2</sub>, and SiO<sub>2</sub> Thin Films*". Applied Optics, **1990**. 29(28): p. 4284-4292.
222. Thielsch, R., Gatto, A., Heber, J., and Kaiser, N., "*A Comparative Study of the UV Optical and Structural Properties of SiO<sub>2</sub>, Al<sub>2</sub>O<sub>3</sub>, and HfO<sub>2</sub> Single Layers Deposited by Reactive Evaporation, Ion-Assisted Deposition and Plasma Ion-Assisted Deposition*". Thin Solid Films, **2002**. 410: p. 86-93.
223. Foroughi Abari, A., *Atomic Layer Deposition of Metal Oxide Thin Films on Metallic Substrates*, in *Chemical and Materials Engineering* **2012**, University of Alberta.

224. Ting-Ting, T., Zheng-Tang, L., and Yan-Yan, L., "*Electrical, Structural and Interfacial Characterization of HfO<sub>2</sub> Films on Si Substrates*". Chinese Physical Letters, **2011**. 28(8).
225. Xu, D., Cheng, X., Zhang, Y., Wang, Z., Xia, C., Cao, D., Yu, Y., and Shen, D., "*Plasma Enhanced Atomic Layer Deposition of HfO<sub>2</sub> with in Situ Plasma Treatment*". Microelectronic Engineering, **2012**. 93: p. 15-18.
226. Weier, D., Chtera, C.F., Siervo, A.D., Rmann, M.S., Dreiner, S., Berges, U., Carazzolle, M.F., Pancotti, A., Landers, R., Kleiman, G.G., and Westphal, C., "*Photoelectron Spectroscopy (XPS) and Photoelectron Diffraction (XPD) Studies on the System Hafnium Silicide and Hafnium Oxide on Si(100)*". Materials Science in Semiconductor Processing **2006**. 9: p. 1055–1060.
227. Cho, M.-H., Chung, K.B., Whang, C.N., Ko, D.-H., Lee, J.H., and Lee, N.I., "*Nitridation for HfO<sub>2</sub> High-K Films on Si by an NH<sub>3</sub> Annealing Treatment*". Applied Physics Letters, **2006**. 88: p. 202902.
228. Suzer, S., Sayan, S., Banaszak Holl, M.M., Garfunkel, E., Hussain, Z., and Hamdan, N.M., "*Soft X-Ray Photoemission Studies of Hf Oxidation*". Journal of Vacuum Science & Technology A: Vacuum, Surfaces, and Films, **2003**. 21(1): p. 106.
229. Ramqvist, L., Hamrin, K., Johansson, G., Fahlman, A., and Nordling, C., "*Charge Transfer in Transition Metal Carbides and Related Compounds Studied by ESCA*". J. Phys. Chem. Solids, **1969**. 30: p. 1835-1847.
230. Von Hauff, P., *Metal Oxide Processing on Gallium Nitride and Silicon*, in *Electrical and Computer Engineering Department* **2012**, University of Alberta: Fall 2012.
231. Rozen, J., Dhar, S., Dixit, S.K., Afanasev, V.V., Roberts, F.O., Dang, H.L., Wang, S., Pantelides, S.T., Williams, J.R., and Feldman, L.C., "*Increase in Oxide Hole Trap Density Associated with Nitrogen Incorporation at the SiO<sub>2</sub>/SiC Interface*". Journal of Applied Physics, **2008**. 103(12): p. 124513.